A Techno-Economic Assessment of Underground Hydrogen Storage with Investigation of H2-Brine Multiphase Flow in Porous Rock at Micro-Scale

Master Thesis

Tim Rademaker

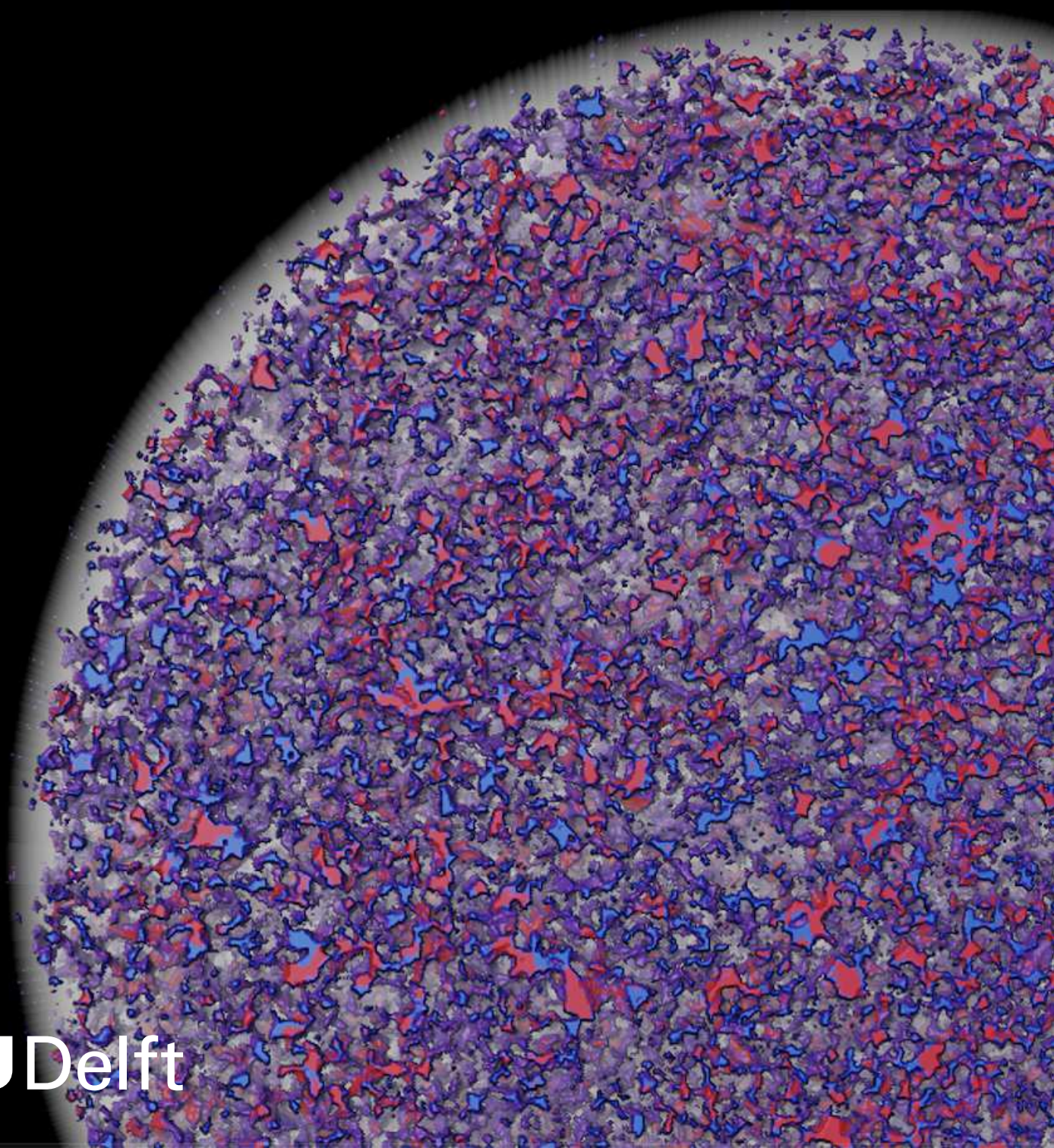

Delft University of Technology

TU Delft

A Techno-Economic Assessment of Underground Hydrogen Storage with Investigation of H2-Brine Multiphase Flow in Porous Rock at Micro-Scale

by

Tim Rademaker

to obtain the degree of Master of Science
at the Delft University of Technology,
to be defended publicly on Tuesday July 9, 2024 at 10:00 AM.

Student number:	4596242	
Project duration:	November 10, 2023 – July 9, 2024	
Thesis committee:	Prof. dr. ir. H. Hajibeygi,	TU Delft, main supervisor
	Dr. M. Boon,	TU Delft
	Prof. dr. Ir. T.J.H. Vlugt	TU Delft
	Ir. M. Looijer	Shell

An electronic version of this thesis is available at http://repository.tudelft.nl/.

TU Delft

Preface

In October 2023, I was searching for a graduation project for my master's degree in Sustainable Energy Technology. Alongside my studies, my enthusiasm for hydrogen technology was further strengthened during my full-time year with Forze Hydrogen Racing. Combined with my bachelor's degree in Applied Earth Sciences, this led to an interest in underground hydrogen storage. Consequently, I contacted Hadi Hajibeygi, who offered me this amazing project, for which I am very grateful. Furthermore, I want to thank Maartje Boon, from whom I received invaluable support during the preparation, execution, and processing of my experiment. I also want to thank Michiel Slob for all of his practical support and Sian Jones for always being available to discuss the challenges I faced in the lab. I am grateful to my supervisors at Shell, Mark Looijer and Karin de Borst, for giving me the opportunity to do an internship and for their guidance throughout. Last but definitely not least, I want to thank Tom Bultreys and especially Chandra Winardhi for inviting me to the University of Ghent, helping me get familiar with CT image processing, and always being available for questions.

Tim Rademaker
Delft, July 2024

Abstract

Underground hydrogen storage (UHS) in porous reservoirs offers a promising solution for addressing the temporal and spatial variability of renewable energy sources. To safely and efficiently utilize these reservoirs for UHS at an affordable cost, it is essential to understand the diverse disciplines involved at various scales. This study combines large-scale techno-economic evaluations with micro-scale laboratory research to assess the commercial and technical viability of UHS in porous media. A techno-economic case study of commercial-scale UHS in a depleted gas field in the Dutch nearshore is investigated, defining the integrated scope of infrastructure and facilities and estimating associated costs. Additionally, the multiphase flow behavior and redistribution of hydrogen in sandstone rock are analyzed through experimental assessment of relative permeability, capillary trapping, dissolution, and Ostwald ripening using CT imagery. The case study compares various surface facility design concepts, revealing that the Levelized Cost of Hydrogen Storage (LCOHS) ranges from Cannot be disclosed for confidentiality reasons , depending on the required purification scope of the production stream. Cushion gas cost significantly impacts the LCOHS. The multiphase flow behavior was examined on a micro-scale by co-injecting hydrogen and brine at varying fractional flows into a vertically placed 17 cm Berea sandstone rock sample at 25°C and 50 bar, while observing under CT imaging during both drainage and imbibition. High-resolution CT imaging visualized Ostwald ripening at the pore scale after several periods without flow. The experimental results indicate a hydrogen end-point relative permeability of 0.043 and a linear trapping coefficient of 0.725. No preferential flow paths were observed, however, dissolution was shown to have an impact the saturation profiles. Pore-scale image analysis demonstrated that Ostwald ripening leads to the fragmentation of mid-sized hydrogen ganglia and the growth of larger ganglia over time. These findings provide valuable insights into optimizing UHS and provide input for large-scale reservoir simulations, emphasizing the importance of integrating techno-economic assessments with detailed laboratory research for the commercial success of UHS.

Contents

List of Figures

Nomenclature

Abbreviations

Abbreviation	Definition
BCM	Billion Cubic Metres
CAPEX	Capital Expenditure
CCET	Capital Cost Estimating Tool
CCO	Capital Cost Outlook
CCS	Carbon capture and storage
CS	Carbon Steel
CT	Computed tomography
EOC	End of Cycle
EPC	Engineering Procurement Construction
FID	Final Investment Decision
GIIP	Gas Initially in Place
HU	Hounsfield unit
ID	Inner diameter
KI	Potassium iodide
LCOHS	Levelized Cost of Hydrogen Storage
LHV	Lower Heating Value
MMV	Measurement, Monitoring, and Verification
OPEX	Operational Expenditures
PEEK	Polyether ether ketone
PoR	Port of Rotterdam
PSA	Pressure Swing Adsorption
PV	Pore volume
SOC	Start of Cycle
TEG	Tri-Ethylene Glycol
TSA	Temperature Swings Adsorption
TVDSS	True Vertical Depth Sub-Sea Underground
UGS	Gas Storage
UHS	Underground Hydrogen Storage

Symbols

Symbol	Definition	Unit
A (relative permeability)	Cross-sectional area	[m^2]
A (trapping)	Linear trapping coefficient	[-]
Ca	Capillary number	[-]
CT	CT number	[HU]
D	Diffusion coefficient	[m^2/s]
f	Fractional flow	[-]
g	Gravitational acceleration	[m/s^2]
H	Henry's constant	[mol/m^3·Pa]
I	CT number (single phase)	[HU]
k	Absolute permeability	[m^2]
k_r	Relative permeability	[-]
L	Length	[m]
l	Equilibrium length scale	[m]
m_g	Molecular mass	[kg/mol]
P	Pressure	[Pa]
P_c	Capillary pressure	[Pa]
P_g	Gas pressure	[Pa]
q	Flow rate	[m^3/s]
R	Radius of curvature	[m]
r	Typical throat radius	[m]
S	Saturation	[-]
S_{gi}	Initial gas saturation	[-]
S_{gr}	Residual gas saturation	[-]
S_{H2}	Hydrogen saturation	[-]
S_w	Water/brine saturation	[-]
S_{wi}	Irreducible water/brine saturation	[-]
t	Pore-scale equilibrium timescale	[s]
v	Darcy velocity	[m/s]
μ	Viscosity	[Pa·s]
ρ	Density	[kg/m^3]
σ	Interfacial tension	[N/m]
ϕ	Porosity	[-]

1 Introduction

As the global push for net-zero emissions accelerates, the reliance on energy storage technologies intensifies. Hydrogen storage emerges as a key solution to addressing the intermittency and geographical constraints of renewable energy sources, thereby enhancing their integration into the overall energy portfolio. By enabling the effective use of diverse local clean energy sources, hydrogen storage reduces reliance on fossil fuel imports. Particularly in the context of current global political instability (e.g., wars), hydrogen storage significantly boosts energy security, underscoring its vital socio-technical relevance. Furthermore, hydrogen will play a large role in reducing carbon emissions in sectors that are traditionally challenging to decarbonize, such as long-haul transportation, heating, and it may serve as a low-carbon option for industrial raw materials. These applications will increase demand for hydrogen from 95 Mt in 2022, to 430 Mt in 2050 [40]. Due to the low density of hydrogen at standard conditions, immense volumes are needed to accommodate this quantity of gas. Geological formations in the subsurface offer the volumes required to store hydrogen at realistic cost. This concept is called underground hydrogen storage (UHS) and can be divided into two main categories: salt caverns and porous media.

Salt caverns are made by intentionally dissolving salt deposits naturally occurring in the subsurface [44] and they have already been used to store hydrogen in the UK and US [65]. In Zuidwending, the Netherlands, an ongoing pilot project aims at converting several salt caverns, presently utilized for natural gas storage, into hydrogen storage facilities [38]. Salt caverns are considered to have several advantages compared to hydrogen storage in porous media: Smaller need for cushion gas, robust sealing capabilities of rock salt, and the non-reactive nature of salt structures, which safeguards the hydrogen against contamination [7]. Furthermore, salt caverns offer relatively large injection and withdrawal rates [7] [65]. The primary limitation of utilizing salt caverns for hydrogen storage lies in their geographical confinement and their limited storage capacities, up to several 100 GWh [29].

Whereas salt caverns are a massive hollow structure, porous reservoirs contain many small pores in which the stored gas resides. These storage sites typically include a reservoir for containment, a caprock that acts as a seal, and are encompassed by a structure that ensures geometric trapping [64]. These reservoirs, which predominantly consist of sandstone or carbonate rock [23], are widely available and the reliance on these large reservoirs (TWh range) as storage option increases as demand for hydrogen grows. UHS in porous media can be subdivided into aquifer storage, storage in depleted gas fields and storage in depleted oil fields [44]. In all three, an in-situ liquid (brine) is commonly present, albeit in varying quantities. This introduces hydrogen to multiphase fluid dynamics when injected or back-produced. Methane (CH_4), air, and carbon dioxide (CO_2) have been effectively and securely stored in depleted hydrocarbon reservoirs and saline aquifers [10]. While there is a growing interest in research on UHS in porous geological formations, comprehensive understanding in this area remains limited. Historically, practical applications have primarily focused on the storage of town gas, which comprises mixtures with approximately 25–60% hydrogen [30]. In recent years, however, several pioneering projects have started exploring this field more extensively, as evidenced by initiatives such as HyUsPRe [36], HyChico [74], and Underground Sun Storage [62].

The operation of UHS is anticipated to differ significantly from underground storage of other gases. This difference arises mainly because of the cyclicity of UHS. In strong contrast to storage of CO_2

(CCS), hydrogen storage entails repeated cycles of injection and withdrawal. This will be influenced by the irregular nature of green energy production. Additionally, the unique physical properties of hydrogen, like its low density and viscosity, may lead to a complex interaction of gravitational, capillary, and viscous forces when stored in porous reservoirs [10]. As a basis for reservoir simulation, important input parameters like wettability, capillary pressure and relative permeability can be experimentally obtained in the laboratory [31] [10]. Microbial activity [70] and gas mixing [9] are processes that further determine recoverability of injected hydrogen and the purity of the withdrawn hydrogen, both important parameters to determine the feasibility of commercial scale UHS [50].

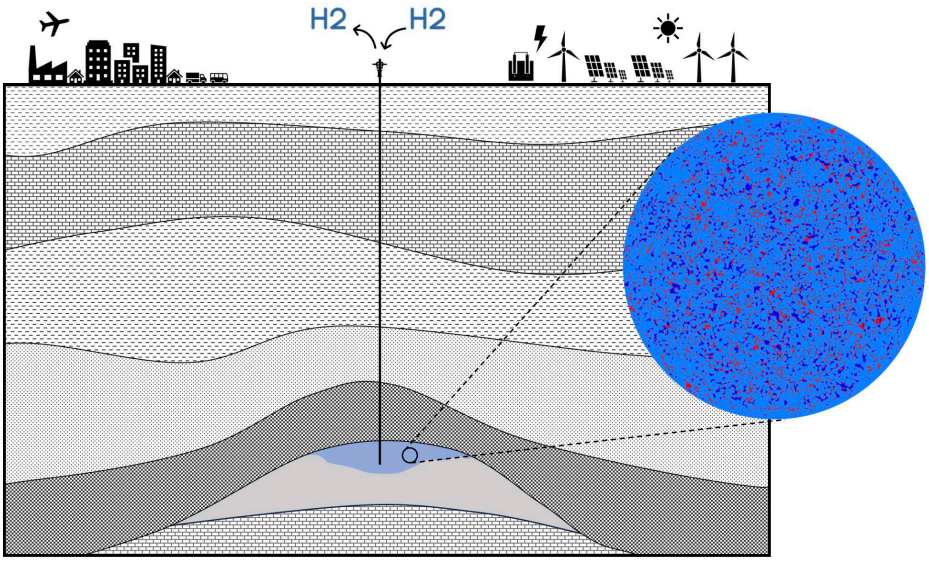

Figure 1.1: A schematic illustration of the UHS concept in a porous reservoir. The close-up view depicts the saturation of a sandstone with brine (dark blue) and hydrogen (red) at the pore scale, as observed in this study.

Integrating micro-scale and core-scale laboratory research, alongside comprehensive techno-economic evaluations at a larger scale, is crucial for achieving commercial success of UHS. Laboratory work provides crucial insights into the physical and chemical interactions in underground environments, while techno-economic assessments ensure the viability and efficiency of such storage systems at a broader, more practical level. Reducing uncertainties in subsurface processes through laboratory experiments will provide better insights into factors such as impurities and flow rates of backproduced hydrogen, and facilitate estimation of potential unrecoverable hydrogen. A large range of these uncertainties can lead to diverse requirements for infrastructure and facilities. Laboratory findings can therefore inform the design parameters for infrastructure and surface facilities, thereby reducing risks associated with the commercial deployment of UHS. This study specifically focuses on investigating both these key aspects through a techno-economic case study of commercial-scale UHS and experimental investigations at the micro-scale.

Part I: Underground Hydrogen Storage in a Depleted Gas Field in the Dutch Nearshore
The first part, which is a study conducted at Shell, will assess the techno-economic feasibility of commercial scale UHS in a depleted gas field in the Dutch nearshore. The approach involves injection of green hydrogen during a period of surplus renewable energy production and withdrawal when renewable energy sources fail to meed demand. It includes both a seasonal use case and a 'Dunkelflaute' use case. A nearshore field was selected as reference in this case study. The main objectives of this study are to define injection and production profiles for both use cases, establish the integrated scope of surface facilities and pipelines, estimate CAPEX, OPEX, and LCOHS, and compare different concepts for tail gas separation and destinations.

Part II: H2/Brine Multiphase Flow and Ostwald Ripening in Sandstone Rock: An Experimental

CT Imagery Approach
The main objectives of the second part are to characterize flow behavior including dissolution and capillary trapping, determine relative permeability, and investigate the effect of Ostwald ripening. This is achieved by co-injecting hydrogen and brine from the top into a vertically placed 17 cm sandstone rock sample while observing under CT imaging. Relative permeability is established by measuring steady-state pressure differences across the rock sample at varying fluid saturations. These saturations and the flow behavior are assessed using CT scans. High-resolution CT imaging enables the visual assessment of hydrogen redistribution over time without flow, attributed to Ostwald ripening.

Part III: Interrelated Implications
At the end of this thesis, a brief part will discuss the implications of the results from both studies in relation to each other.

Appendix A includes a detailed guideline for pore-scale image processing, followed by supplementary figures in Appendix B

I

Underground Hydrogen Storage in a Depleted Gas Field in the Dutch Nearshore

2

Previous studies

Previous techno-economic studies on UHS have investigated various geological formations, including depleted oil and gas reservoirs, saline aquifers, and salt caverns, with a focus on assessing their feasibility, performance, and economic viability. In 2014, Lord et al. [51] recognized the necessity of UHS to buffer the intermittency of renewable energy sources. They conducted an economic analysis addressing the costs involved in developing and operating a UHS facility, focussing on salt caverns due to their proven technology and greater geotechnical certainty. Gianni et al. [24] conducted a comparative techno-economic study on UHS in various geological formations. Their findings indicate that UHS in porous media is the most economically attractive option in terms of the levelized cost of hydrogen storage (LCOHS), which measures cost per kilogram of hydrogen stored. However, they acknowledge that the optimal storage technology is highly site-specific. The HyUSPRe consortium project explores the feasibility and potential for large-scale renewable hydrogen storage in porous reservoirs across Europe. Their deliverables include estimating the hydrogen storage potential of existing European gas storage sites in depleted fields and aquifers [13], conducting studies on complex subsurface processes, and determining equipment requirements and cost estimates [42]. Zooming in further, case studies have been conducted on the Dutch subsurface, which features abundant geologic salt structures and depleted gas fields both onshore and offshore. EBN & TNO collaborated on a techno-economic feasibility study of UHS in the Dutch offshore region, comparing offshore and onshore technologies [19]. The study concluded that for short-cycle storage, onshore salt caverns are the most economically attractive, with other technologies costing at least twice as much for this purpose. They also suggest that onshore salt caverns are optimal for seasonal storage, although a reduction in cushion gas costs could quickly make storage in depleted gas fields more appealing. Moreover, the study indicates that offshore infrastructure investment costs for both salt caverns and depleted gas fields would be 1.5 to 2.5 times higher than their onshore counterparts. Yousefi et al. [83] highlighted a gap in the attention given to surface facility design requirements, particularly concerning the expected flow rates of hydrogen. They conducted a case study focusing on a field located in the northern part of the Dutch onshore subsurface. Their work involved subsurface modeling to assess storage capacity, and to determine injection and withdrawal rates for both seasonal and short-term storage scenarios using hydrogen or nitrogen as a cushion gas. Additionally, they designed surface facilities tailored for injection and withdrawal operations, and estimated the Levelized Cost of Hydrogen Storage (LCOHS). Given the overlapping objectives, the study by Yousefi et al. [83] serves as a valuable source for comparison for this study, as it similarly presents a techno-economic case study for UHS using a depleted reservoir in the Dutch subsurface. However, this study places particular emphasis on the integration of surface facilities, a significant challenge specific to this case.

3

Study basis

This study will assess the feasibility of commercial scale UHS in a depleted gas field in the Dutch nearshore. The nearshore field, refered to as 'NSH' is used as reference in this case study. The field location cannot be disclosed for confidentiality reasons. This field is proposed as a potential field for UHS due to its seemingly suitable subsurface properties. However, there are currently no commercial plans to develop this field for UHS. This report serves solely as a case study.

The development of the NSH field for a commercial scale UHS system in this case study is based on a seasonal storage concept with steady yearly injection-production cycles, as well as short high production intervals during a 'Dunkelflaute' event. Abandonment pressure before conversion to UHS is assumed to be 9 bara. The chosen working pressure range for hydrogen storage and back-production is 150–250 bara. To achieve this pressure range, cushion gas injection is required to raise the pressure of the gas field to 150 bara. In this case study, hydrogen (H_2) is selected as the cushion gas, and an estimated volume of 2.30 billion cubic meters (BCM) of H_2 at normal conditions will be needed. The total storage volume (working gas volume of H_2) is estimated to be 1.54 BCM.

In this study, it is assumed that a share of the working volume is reserved for each use case: 0.78 BCM for the seasonal use case, and 0.76 BCM for the Dunkelflaute use case. For the seasonal use case, 8.67 M Nm³/d of H_2 will be produced during a period of 90 days each year. 54.24 M Nm³/d will be produced intermittently over 14 days total for the Dunkelflaute use case. The Dunkelflaute working volume and production rate are chosen such that 4 GWe can be generated in gas-fired power plants using the produced H_2 as fuel. An injection rate of 9.28 M Nm³/d H_2 will be required over a period of 166 days to fill the total 1.54 BCM.

Despite the high level of depletion of the NSH field, production of contaminants during UHS operation is inevitable. Similar to case study SRN-04205 [3], it is assumed that a constant free flow rate into the H_2 backbone is required during seasonal production, which is 8.67 M Nm³/d in this study. Therefore, considering separation of contaminants in processing facilities, larger production rates are required as the fraction of impurities increase. For the seasonal production stream, a Pressure Swing Adsorption (PSA) unit separates the produced H_2 stream into two components: a clean H_2 stream meeting H_2 backbone specifications [37] and a by-product stream known as 'tail gas'. This tail gas is re-injected into a nearby empty gas field in the reference case. Furthermore, given that the H_2 recovery from the PSA is approximately 92%, the reservoir production rates must also be increased to offset the H_2 loss in the tail gas.

As a production of 8.67 M Nm³/d for 90 days will exactly deplete the reserved store working volume, overproduction results in a reduction in H_2 cushion gas within the reservoir, requiring replenishment. As a result, the injection rates will also exceed 9.28 M Nm³/d. For the Dunkelflaute use case, purities below backbone-spec are acceptable and overproduction is not necessary. Distribution of this export stream is beyond the scope of this study.

In the favourable case that the high level of depletion of the NSH field will result in backbone-spec purities (98 – 99.5%) in the production stream, overproduction/injection, a PSA, and a destination for the tail gas stream will not be necessary, thereby substantially simplifying the concept.

To estimate the purity of the production stream, existing reservoir simulations performed in SRN-04205 are scaled to the level of depletion of NSH (9 bara). This scaling estimates a minimum purity of 98.5% in the 6th cycle. This would meet the lower end of the possible backbone purity spec and

in this case, a PSA and overproduction/injection would not be needed. In case backbone-spec purity requires 99.5% and a PSA will be needed, the total seasonal production rate would increase to 9.46 M Nm³/d at the start of the production cycle to 9.57 M Nm³/d at the end of the production cycle in order to maintain a steady H_2 backbone export rate of 8.67 M Nm³/d. To compensate for the overproduction, a replenishment of 0.45 M Nm³/d would be required, and the injection rate would increase to 9.73 M Nm³/d.

To address uncertainties related to production stream purity and to compare tail gas destinations, this study examines various concepts with identical H_2 export rates. Note that Concept [A[] is also referred to as the reference case.

Concept	Purification	Tail Gas Destination
[A]	PSA	Reinjection into nearby field
[B]	PSA	Reinjection into NSH
[C]	PSA+cryogenic	Reinjection of non-H_2 gas into nearby field
[D]	PSA+cryogenic	Reinjection of non-H_2 gas into NSH
[E]	None	No tail gas

Table 3.1: Summary of concepts examined in this report.

No well-performance analysis is conducted in this study. Instead, performance estimates are provided by Shell's Production Technologists.

3.1. Reservoir (NSH)

Cannot be disclosed for confidentiality reasons

Table 3.2: Reservoir properties of the NSH field (Shell internal source). Note that actual abandonment pressure depends on potential further development plans.

Due to the seemingly suitable subsurface properties for UHS, this field is might be suitable for UHS. However, the field is also attractive from a commercial perspective due to its proximity near Rotterdam, which is anticipated to become a significant hydrogen hub. The Maasvlakte, adjacent to Rotterdam, hosts several H_2 production initiatives in various stages of planning or execution (including Shell's 200 MW electrolyser project, Holland Hydrogen I). Additionally, the harbour is being outfitted with facilities to support H_2 import and distribution.

The most recent available reservoir gas composition is as follows:

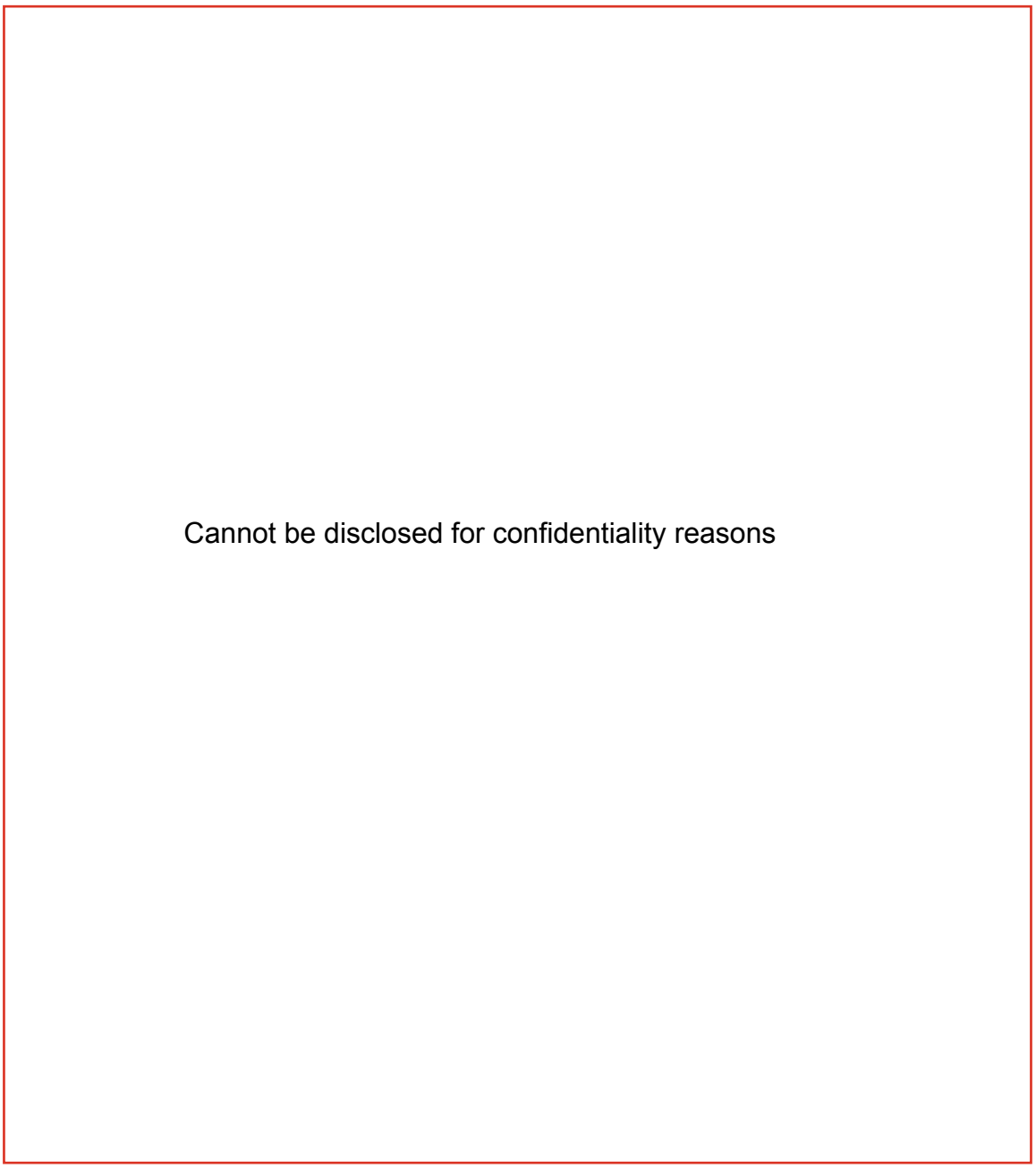

Table 3.3: Reservoir gas composition for NSH (Shell internal source).

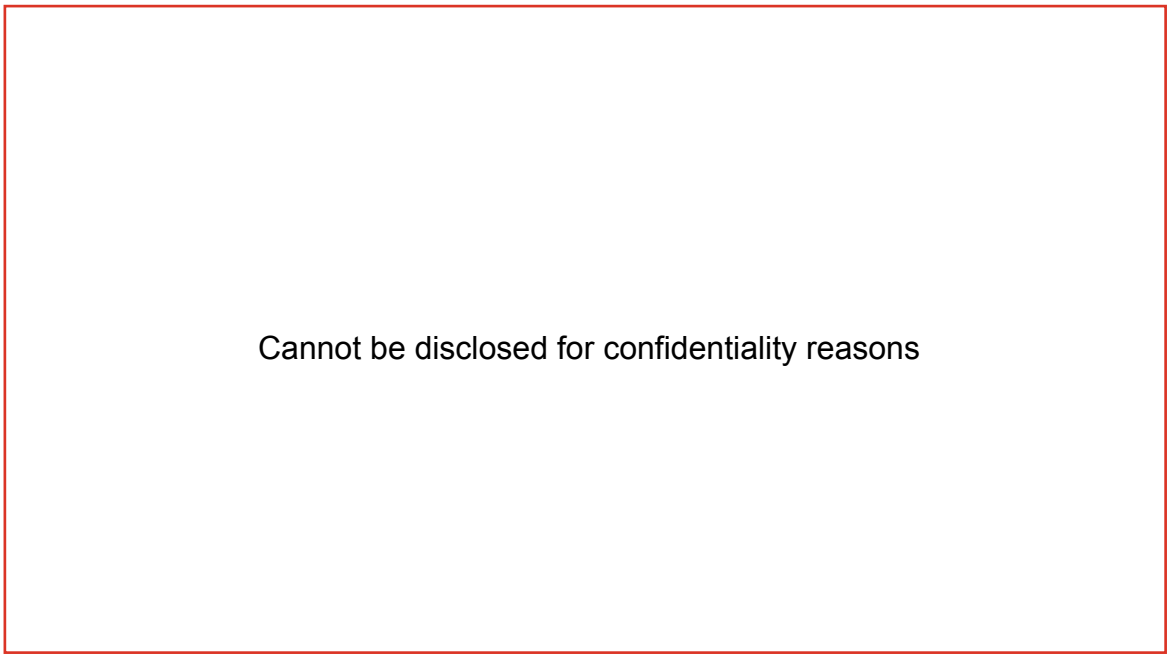

Figure 3.1: Dutch gas field map showing NSH and its proximity to the port of Rotterdam [58].

3.1.1. Working volume

To increase the reservoir pressure from 9 bara to the lower end of the working pressure range (150 bara), an estimated 2.30 BCM of H_2 cushion gas (at normal conditions) should be injected. The compressibility factor of H_2 is 1.0731 at 150 bara and 20 °C, and 1.1226 at 250 bara and 20 °C (Shell internal source). To calculate the volume of working gas, or storage capacity, an average value of 1.09785 is used for the calculation. This leads to a working volume of 1.54 BCM.

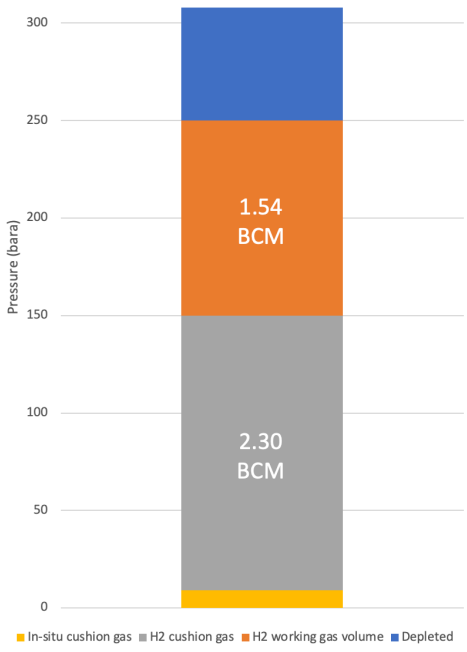

Figure 3.2: Store pressure breakdown, indicating the pressure ranges including the corresponding H_2 volumes for the cushion gas and the working volume.

3.1.2. Working pressure range

For this case study, a free flow production philosophy is adopted to select the working pressure range. This entails that no recompression of the produced stream would be required before export. The operating pressure regime of the future H_2 network in the Netherlands (H_2 backbone) will be between 30 and 50 bar [37]. It is assumed that H_2 will be imported from the H_2 backbone at 30 bar and exported at 50 bar. Therefore, the lower end of the working pressure range should be sufficient to export the processed H_2 at 50 bar without recompression. Choosing an optimal working pressure range in the store would require an extensive sensitivity analysis in which several trade-offs need to be considered, for example:

- Increasing the high end of the working pressure would mean that the injection compression system would become more expensive from both a CAPEX and OPEX perspective.
- Decreasing the lower end of the working pressure range would reduce well productivity, resulting in a larger number of required wells to reach the same production rates.
- Decreasing the lower end of the working pressure range potentially requires additional recompression as the pressure in the production stream may drop below the export pressure during processing.

These factors have been considered in similar UHS studies. To align with their findings, a working pressure range of 150-250 bara is assumed. This pressure range aims to strike a balance between storage capacity, cost-effectiveness, and production efficiency.

3.2. Use cases

To effectively deploy UHS on a commercial scale, it must be utilized in contexts where it outperforms other energy storage technologies in terms of cost-effectiveness. UHS in porous media has the potential to efficiently store energy on a large (TWh) scale over extended periods, making it a viable option for addressing seasonal imbalance in renewable energy supply and demand [53].

It is important to recognize that there exists significant uncertainty regarding the widespread adoption of H_2 as a storage solution. Consequently, this results in uncertainty in the projected levels of H_2 demand and supply beyond 2030. The primary driver of this uncertainty is the production cost of green H_2 (electrolysis). For the Netherlands, two potential scenarios can be anticipated:

1. Green H_2 production in the Netherlands is expected to accelerate rapidly, with substantial price reductions anticipated from 2030 onwards. These cost reductions will make it economically viable to store locally produced green H_2 generated from solar and wind sources on a large scale. In this scenario, a seasonal storage pattern can be anticipated.
2. Green H_2 production in the Netherlands is expected to evolve slowly, with demand primarily met through the import of liquid ammonia via shipping or gaseous H_2 through pipelines. In this scenario, there will be no significant seasonal storage pattern.

For this case study, it is assumed that scenario 1 will prevail. Furthermore, the commercial store is proposed to serve two purposes simultaneously. These use cases are defined in the sections below.

3.2.1. Seasonal store

It is assumed that the supply and demand into and out of the Dutch H_2 backbone will exhibit a seasonal pattern. The H_2 supply trend in the Netherlands is expected to align with the yearly wind speed profile. This assumption is based on the relatively large capacity factor of (offshore) wind energy [41], which provides a steady power supply for electrolysis. The large H_2 supply into the backbone is buffered by storage in depleted gas fields. This seasonal storage use case entails steady injection and production into/from the store. Based on average monthly wind speeds in The Hague, injection will occur from October to March, while production will take place from June to August.

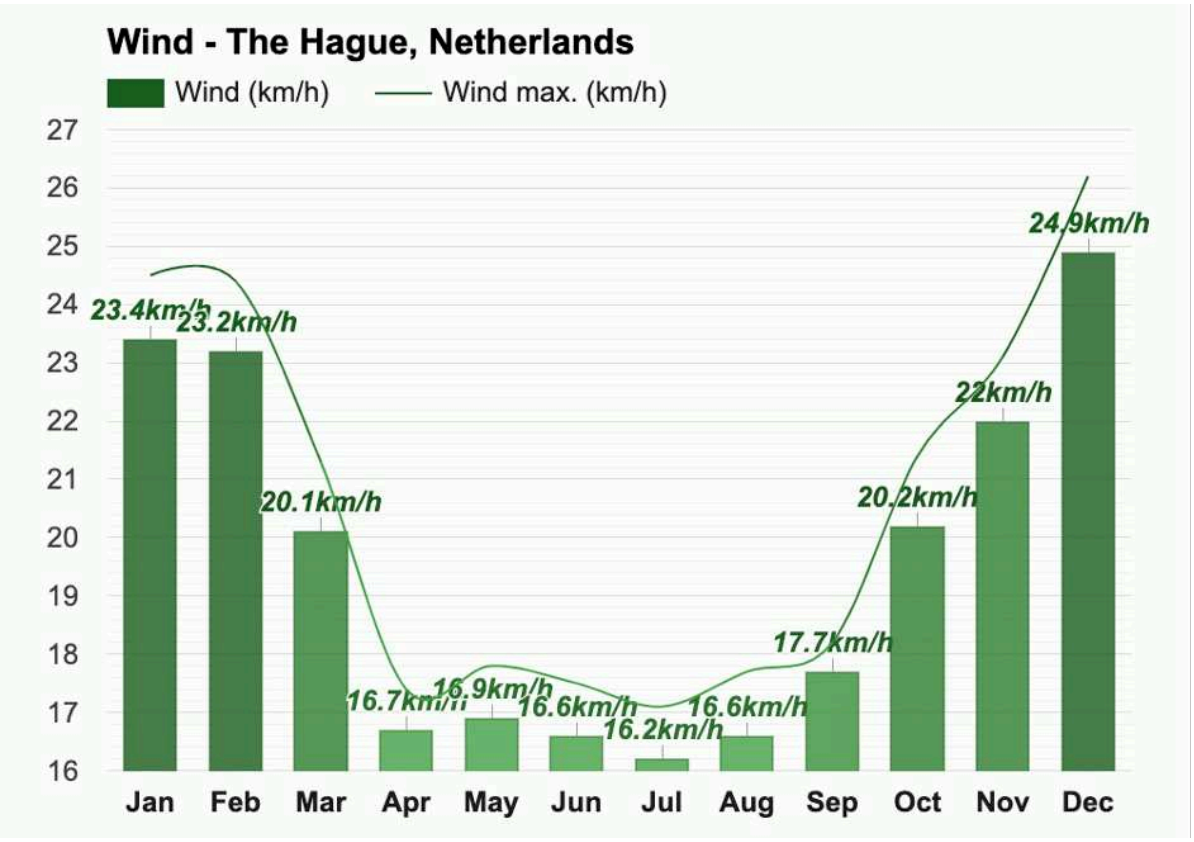

Figure 3.3: Monthly average wind speeds in The Hague [78].

3.2.2. Dunkelflaute

In North Sea and Baltic Sea countries, 2 to 10 so-called “Dunkelflaute” events lasting longer than 24 hours occur annually [49]. These events are characterized by very low levels of renewable energy production due to simultaneous occurrences of low wind speeds and overcast conditions. For this case study, it is assumed that the Dutch reliance on import of energy will be minimized in the future to ensure energy security. Therefore, Dunkelflaute events in the Netherlands ask for controllable energy supply within national borders. This implies the relevance of the second use case, in which stored H_2 will be used to fire gas turbine power plants during Dunkelflaute. Providing H_2 distribution to these power plants will involve collaboration with Gasunie, the operator of the Dutch gas transmission grid, and is beyond the scope of this study.

In this case study, it is assumed that Dunkelflaute events in the Netherlands will occur for 75 hours in January, 120 hours in November, and 135 hours in December, based on Figure 3.4. For simplicity, the number of hours is rounded to the number of hours in the nearest number of full days: 3 consecutive days in January, 5 consecutive days in November, and 6 consecutive days in December. Additionally, it is assumed that the Dunkelflaute events will consistently occur during the same period every year of operation.

3.2.3. Working volume per use case

Both use cases will reserve a ‘share’ of the total working volume of the store, where the required H_2 production rate during Dunkelflaute will be the starting point. In the greater Rotterdam area, where the commercial store is situated, there is currently approximately 4 GW of installed electric capacity from natural gas-fired power plants as of 2024 (Figure 3.5). Eneco, the operator of the Enecogen power plant in the Port of Rotterdam, is researching the possibility of converting its facility into a H_2 fired power plant [20]. Based on its capacity of 870 MW, and 59% LHV efficiency (assuming the same efficiency for H_2 as for natural gas), it would require 1.5 GW of H_2 fuel at maximum capacity. Extrapolating these values to the 4 GW as described above, the Dunkelflaute use case would require 6.8 GW of H_2 production from

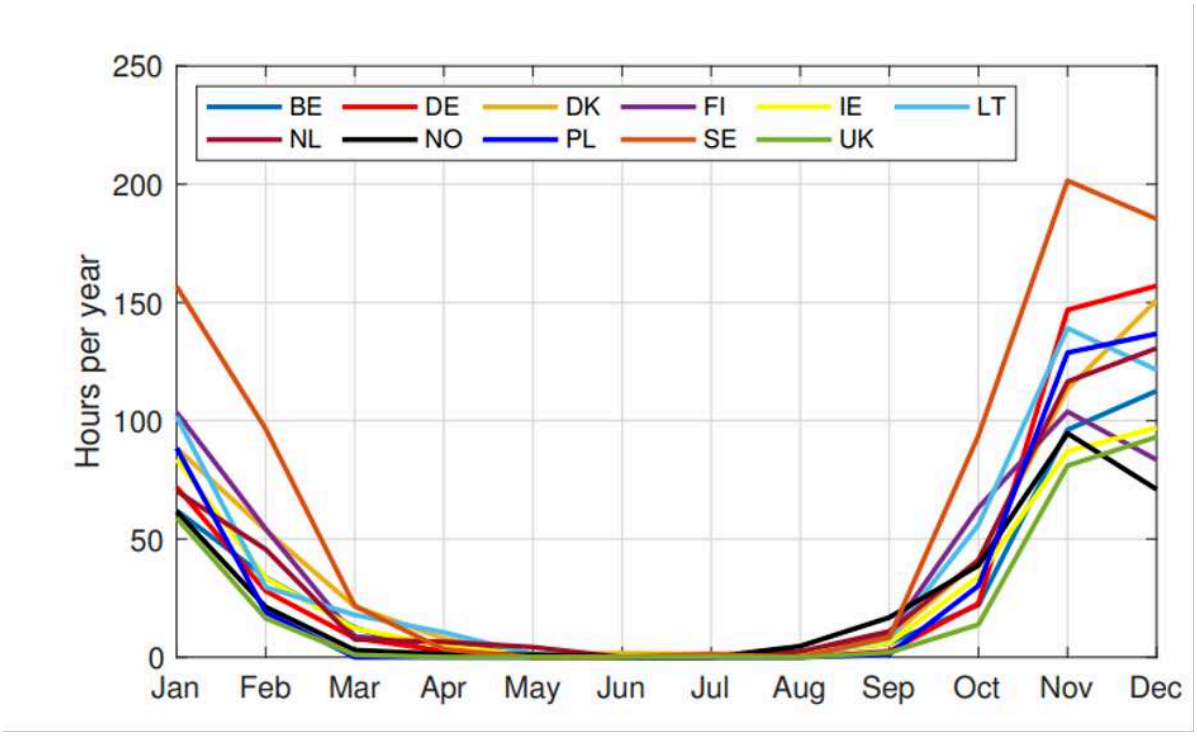

Figure 3.4: Monthly variation of Dunkelflaute hours per year for several countries near the North Sea and Baltic Sea [49].

Producent	Centrale	Plaats	Naam	Type eenheid	Hoofd-brandstof	Nominaal Elektrisch Vermogen [MW]	Nominaal Thermisch Vermogen [MW]	In bedrijf vanaf
EPH	Rijnmond Energie	Rotterdam (Vondelingenplaat)	Rijnmond Centrale	STEG	Aardgas	810	–	2004[17]
Eneco / EPH	Enecogen	Rotterdam (Europoort)	EGEN10	STEG	Aardgas	465	–	2012
Eneco / EPH	Enecogen	Rotterdam (Europoort)	EGEN20	STEG	Aardgas	435	–	2012
EPH	Maasstroom Energie	Rotterdam (Vondelingenplaat)	MSEC	STEG	Aardgas	427	–	2010
RWE	Centrale Moerdijk	Moerdijk	Moerdijk-2	STEG	Aardgas	426	–	2012
RWE	Centrale Moerdijk	Moerdijk	Moerdijk-1	Gasturbine/WKC	Aardgas	339	–	2008
Air Liquide	PerGen	Rotterdam (Botlek)		Gasturbine/WKC	Aardgas	300	– [19]	2007
Uniper	Centrale RoCa	Rotterdam	Roca-3	STEG/WKC	Aardgas	220	200[10]	1997
Air Liquide/Eneco	EuroGen	Rotterdam (Botlek)		Gasturbine/WKC	Aardgas	130	–	1994
Uniper	Energiecentrale Den Haag	Den Haag		STEG/WKC	Aardgas	97	– [7]	1901
Uniper	Maasvlakte UCML	Rotterdam (Maasvlakte)		Gasturbine/WKC	Aardgas	80	– [8]	2003
Uniper	Centrale RoCa	Rotterdam	Roca-1	Gasturbine/WKC	Aardgas	25	70[10]	1983
Uniper	Centrale RoCa	Rotterdam	Roca-2	Gasturbine/WKC	Aardgas	25	70[10]	1983
Europoort Utility Partners	Europoort Utility Partners	Rotterdam (Europoort)		Gasturbine	Aardgas	24	–	1997

Figure 3.5: Gas fired power plants in the greater Rotterdam region [79].

the store. Or, considering 14 days of Dunkelflaute per year, 2.3 TWh. This equals 0.76 BCM (normal conditions) of stored H_2 (LHV). For the NSH case, the expected H_2 purity in the produced stream will be relatively high due to the high level of depletion of the field. Still, some mixing with the in-situ gas is inevitable. It is important to note that produced H_2 with some co-produced natural gas can still serve the Dunkelflaute purpose without necessitating a Pressure Swing Adsorption (PSA) process. This insight was verified by an Eneco employee via email correspondence.

The remaining working volume of 0.78 BCM will be allocated for the seasonal use case. Considering the injection- and production periods for each use case and the associated working volumes, the injection- and production rates can be calculated. It is assumed that the produced working volume for both use cases will be replenished simultaneously from October to March.

In this study, the allocated working volume and injection/production period will lead to injection/production rates of **backbone spec** H_2, as summarized in Table 3.4. As the seasonal use case requires production stream purification to meet backbone spec, the total seasonal production rate will exceed the production rate of **backbone spec** H_2 alone. This will be addressed in Section 3.3. Contrarily, as the Dunkelflaute use case allows impurities, this distinction will not be made for the Dunkelflaute production stream. Therefore, for this use case, the total volume (normal conditions) of **backbone-spec** H_2 injected will equal the volume of **sub-backbone-spec** H_2 produced. Moreover, it is assumed that the 0.76 BCM working volume allocated for the Dunkelflaute use case will be available before the first year of production. This provision ensures that the reservoir pressure will not fall below 150 bara, even if

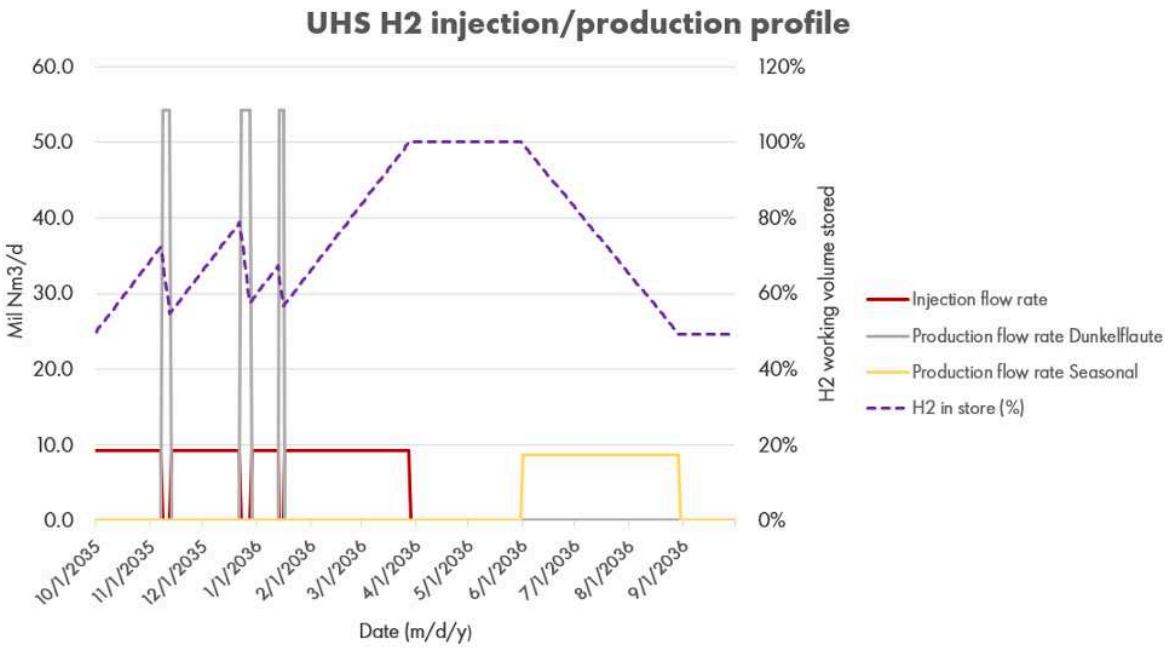

Figure 3.6: Conceptual injection/production profile for commercial scale UHS in this case study.

Dunkelflaute occurs early during the injection period. At the end of the seasonal production period, the remaining H_2 in the store represents the allocated working volume for the Dunkelflaute use case in the upcoming cycle. Figures 3.6 - 3.8 depict a potential production and injection scheme for commercial operations, including the rare scenario of early-season Dunkelflaute events.

System failures resulting in shutdowns are excluded in this study. Additionally, start-up and shut-down times are neglected.

Parameter	Total	Seasonal	Dunkelflaute
Working volume [BCM]	1.54	0.78	0.76
Max. reservoir pressure [bara]	250	-	-
Min. reservoir pressure [bara]	150	-	-
Yearly injection period [days]	166*	-	-
Yearly production period [days]	-	90	14
Injection rate [M Nm³/d]	9.28[b]	-	-
Production rate [M Nm³/d]	-	8.67[b]	54.24[s]

* = 180 days – 14 days of Dunkelflaute production
[b] Backbone-spec purity
[s] Sub-backbone-spec purity

Table 3.4: Key conceptual operating parameters.

3.3. Tail gas production

In a depleted gas field, residual gases are always present. Consequently, when H_2 is injected into the storage reservoir, it will mix with the in-situ gases, leading to impurities in the production stream. Reservoir simulations for SRN-04205 [3] indicate that these impurities will be most significant after 6 years, at the end of the annual production cycle. To estimate impurities in the production streams of this study, the same reservoir simulation of SRN-04205 case are used. However, this study assumes that the non-H_2 gas fractions in the produced gas are scaled down based on the difference in abandonment pressure. It is assumed that a difference in production flow rate will not result in different non-H_2 gas fractions. As a result, the minimum H_2 fraction in the production stream is 98.5% at the end of the

Figure 3.7: Store fill level broken down into use cases.

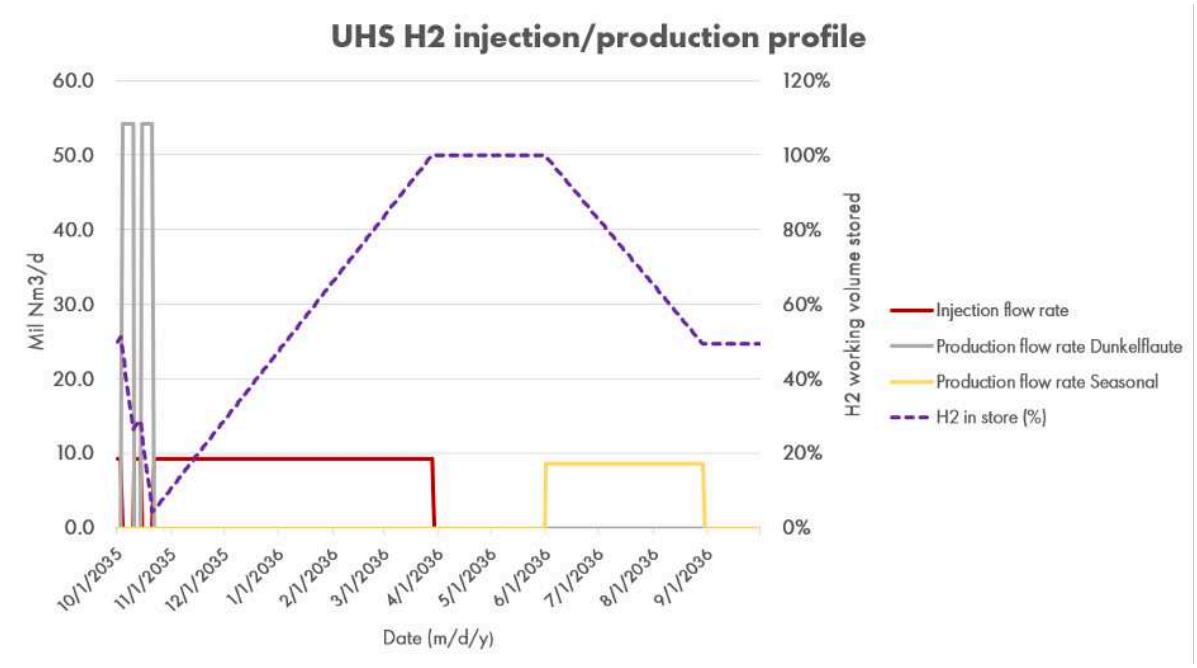

Figure 3.8: Conceptual injection/production profile for early-season occurrence of Dunkelflaute events.

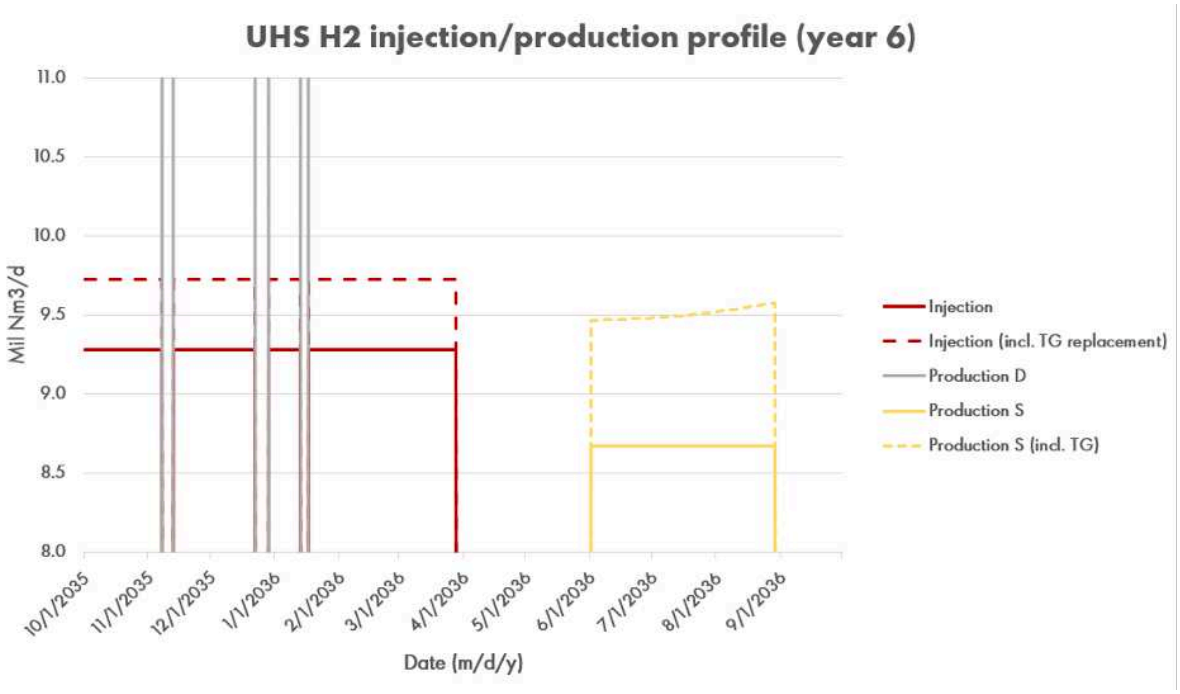

Figure 3.9: Conceptual injection/production profile for commercial scale UHS in this case study. including tail gas (replacement).

6th yearly cycle. If a PSA system is used for purification, a maximum total production rate of 9.57 M Nm³/d (at the end of the production period) is required to supply a steady production of H_2 (8.67 M Nm³/d) to the H_2 backbone throughout the production cycle. The calculations consider a H_2 recovery efficiency of 92% in the PSA as indicated by a vendor, with 8% of the produced H_2 being separated along with non-H_2 gases (primarily CH_4, N_2, C_2H_6, and CO_2). To account for the unrecovered H_2 and the increasing fraction of non-H_2 gases, the reservoir's production rate is thus adjusted from 9.46 M Nm³/d to 9.57 M Nm³/d over the production period. Note that the large purity of the production stream (minimum 98.5%) corresponding to the low abandonment pressure of the reservoir might imply that a PSA and the overproduction are redundant in case the backbone quality specification will be kept at 98% H_2 [37]. This scenario is considered in Chapter 8. In cases where a PSA and overproduction are necessary, the expected tail gas production coming out of the PSA will be 0.79 M Nm³/d at the start of the 6th production cycle, and 0.90 M Nm³/d at the end of the 6th cycle. A tail gas replacement of 0.45 M Nm³/d must be injected over the 166-day injection period to compensate for the tail gas 'lost' during the 90-day seasonal production period. In the reference case, where tail gas is reinjected in a nearby field, this tail gas replacement comes from the H_2 backbone. Consequently, the resulting total injection rate would be 9.73 M Nm³/d. As mentioned earlier, the production flow rate for the Dunkelflaute use case remains unchanged due to acceptable small impurities, allowing the bypassing of a PSA.

	Flow rate [M Nm³/d]	H_2 [mole fraction]	N_2 [mole fraction]	CO_2 [mole fraction]	CH_4 [mole fraction]	C_2H_6 [mole fraction]
Start of cycle	9.46	0.996212	0.001876	0.000001	0.001902	0.000009
End of cycle	9.57	0.985085	0.001832	0.000138	0.011830	0.001115

Table 3.5: Production stream composition used in this case study (6th production cycle).

3.3.1. Reservoir simulation uncertainty

The production stream composition in Table 3.5 is based on a fine grid generic 2D model reservoir simulation from SRN-04205 [3] where the following input parameters were used:

- Average Permeability = 100 mD
- Heterogeneity (Dykstra-Parson coefficient) = 0.9

- Ratio of vertical permeability and horizontal permeability (Kv/Kh) = 0.1
- Homogeneous porosity
- Dip = 0°
- A component slate of H_2, N_2, CO_2, CH_4 and C_2H_6 is used for reservoir modelling. No other components are included in reservoir modelling
- Abandonment pressure of natural gas field = 44 bar
- Injection from May – November (180 days) (to 250 bar) followed by 2-month idle period
- Production from January – April (90 days) (to 150 bar) followed by 1-month idle period
- The composition of the injection stream is of backbone-spec
- Production rate of 2.58 M Sm^3/d in the 6th year

In SRN-04384 [34], the impact of reservoir uncertainties and design choices on production stream gas compositions within this model were analyses. The sensitivity analyses led to the following results:

Parameter	Description	Impact on Recovery[1]	Impact on Hydrogen Minimum Mol Concentration in Back Produced Gas[1]
Vertical Heterogeneity	Heterogeneuous reservoir with VDP = 0.6	Low 93.8% vs 94.4%	High 89.1% vs 92.6%
Dip Angle	10° dip angle	Low 93.9% vs 93.8%	Moderate 90.8% vs 89.1%

Figure 3.10: Summary of reservoir parameter sensitivity analyses conducted in SRN-04384 [34] with reference to a base case used in the study: 100 mD, Kv/Kh = 0.1, 15% porosity, 50 bar abandonment pressure, no dip, no vertical heterogeneity (layering), constant 0.5 M Sm^3/d injection rate (90 days), constant 1 M Sm^3/d production rate.

Design Choice	Description	Impact on Recovery[2]	Impact on Hydrogen Minimum Mol Concentration in Back Produced Gas[2]
Well Perforations	Only upper half layers perforated	High 94.4% vs 93.8%	High 91.5% vs 89.1%
Rate	Double rate	Low 94.2% vs 94.4%	Low 89.0% vs 89.1%
Abandonement Pressure	50 bar to 100 bar	Low 94.0% vs 93.8%	Very High 93.3% vs 76.4%
Partial Cycling[3]	Multiple cycles per year and variable length ranging from 2 weeks to 2 months	Moderate 93.7% vs 93.4%	Low 94.8% vs 94.7%
Ramp Up[3]	1/3 rate for 5 years, 2/3 rate for 5 years and full rate for remaining years	High 91.8% vs 93.4%	Moderate 94.9% vs 94.7%

Figure 3.11: Summary of design choice sensitivity analyses conducted in SRN-04384 [34] with reference to a base case used in the study.

For this study, only the difference in abandonment pressure was considered to scale the production stream composition, as it significantly outweighs the other categories in its impact. The non-H_2 fractions of the end of the 6th production cycle of a simulation for SRN-04205 [3] were multiplied by a factor 0.205 (which is 9/44) to account for this difference. However, it is important to recognize that this linear correlation is not supported by empirical evidence and should be interpreted with caution.

Figures 3.10 and 3.11 also indicate the level of uncertainty due to possible potential variations in reservoir parameters and design choices that were not considered in this study. SRN-04384 [34] considered only one well that serves both purposes of injection and production in the sensitivity analyses. However, in this case study, several wells at separate locations are considered. Therefore, the impact of this well configuration on the uncertainty of production stream composition cannot be estimated based on SRN-04384 [34].

Finally, it is important to note that the reservoir simulations only consider mixing with in-situ gas and do not account for loss of H_2 or contamination due to microbial or geochemical reactions. This study focuses on H_2 purity and H_2 recovery is not considered.

4

Scope

The current NSH well pad covers approximately 9500 m^2. However, this area alone cannot accommodate a significant portion of the injection and production scope. Consequently, considerable attention has been devoted to designing a system integration concept that involves multiple locations for various aspects of the scope. In the following section, a detailed analysis of the operational processing of the injection and production stream in a commercial case is provided. Pipeline material is assumed to be CS XS65 clad 825 for wet streams, and CS X65 for dry streams, as advised by Shell's H_2 Pipelines Research Team. Pressure drops over pipelines are calculated with Shell's Hydrogen Pipeline Pressure Drop Calculator,' using hydrogen's dynamic viscosity of $8.74*10^{-6}$ Pa s at 15°C and 50 bar [57]. A wall roughness of $3.00*10^{-5}$ m is used. Process equipment parameters are estimated using Shell's CCET (Capital Cost Estimating Tool).

4.1. Injection Process

During the injection process, H_2 from the backbone is conveyed through a 16-inch carbon steel (CS X65, wall thickness 8 mm) pipeline to a metering station which is installed to measure the H_2 flow taken from the backbone. This same metering station is also utilized during the production process to measure the H_2 flow from the production processing site back to the backbone. The incoming H_2 stream arrives at the metering facility at a pressure of 29.5 bara from the backbone. To meet the required working pressure, the H_2 must be compressed to a pressure range of roughly 170 bara to 270 bara (depending on the store fill level) to account for a pressure drop over well tubing and in the near-wellbore area. No further treatment of this H_2 stream is necessary. The compression system is specifically designed to achieve the desired pressure of 270 bara while maintaining a flow rate of 9.73 M Nm³/d. It employs a 3-stage reciprocating compressor equipped with interstage air coolers and knockout (KO) drums. Centrifugal compression will likely not be suitable due to the resulting large number of required impellers and a much smaller compression ratio because of hydrogen's low molecular weight [54]. Nine parallel compressors will be required for the desired flow rate.

Please note that the first compression stage will occur at a different hypothetical location. This location will be further detailed in Section 4.2. The decision to separate the compression stages stems from the limited available space at the NSH well pad. In this arrangement, the first stage will elevate the pressure from 29.5 bara to 65 bara. To connect the first stage with the second and third stages at the NSH well pad, a bidirectional 24-inch CS XS65 clad 825 pipeline spanning 10.5 kilometres will be employed. A wall thickness of 13 mm is selected as advised by the H_2 Pipelines Research Team. The large diameter is chosen as this pipeline also transports the production streams.

This separation in compression stages strikes a balance between saving plot space at NSH and avoiding excessive pressure levels in the connecting pipeline that would necessitate the use of costly materials. The notably large diameter is necessary to accommodate the high flow rates during Dunkelflaute production.

Compression/ cooling stage	Inlet pressure [bara]	Inlet temperature [°C]	Discharge pressure [bara]	Discharge temperature [°C]
Compression stage 1	29.5	15.0	65.0	105.6
After cooler 1	65.0	105.6	64.7	40.0
Compression stage 2	64.7	40.0	132.2	128.0
Inter-stage cooler 2-3	132.2	128.0	131.8	40.0
Compression stage 3	131.8	40.0	270.0	128.4
After cooler 2	270.0	128.4	269.9	100.0*

* Equal to the reservoir temperature of NSH.

Table 4.1: Summary of injection compression system up to 270 bar. Designed in CCET.

4.1.1. Injection wells

Since no well-performance analysis was conducted in this study, an estimate provided by Shell's Production Technologists was used to determine the number of wells required for this case. Given that the flow rate for injection (9.73 M Nm³/d) closely aligns with the flow rate for seasonal production (9.57 M Nm³/d), the wells will serve a dual purpose. This dual purpose also leads to large purities for seasonal production. For further details, please refer to the subsection dedicated to the production wells (Subsection 4.2.1).

4.1.2. Well pad layout

The small size of the NSH well pad, combined with its location in a densely populated area with many greenhouses, presents one of the main challenges for implementing a commercial-scale UHS at NSH. To estimate the areas occupied by the different facilities, plot size of existing UGS sites (Norg and Grijpskerk) are scaled down to the required flow rate and pressure. Compressor noise production and multi-MW electricity supply could pose a challenge for commercial scale UHS operation at this site. Also, due to the immaturity of UHS, safety distances could be larger for compared to conventional natural gas production/storage.

Figure 4.1: Indicative potential well pad layout at NSH [26].

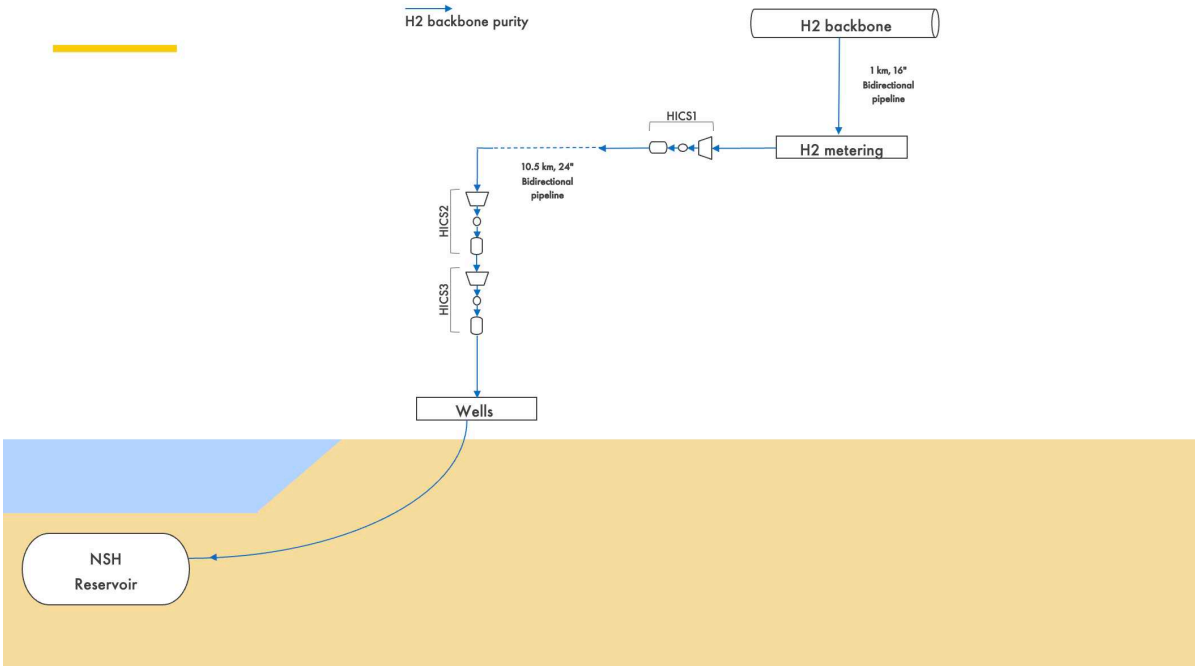

Figure 4.2: Injection process flowchart. HICS denotes a hydrogen injection compressor stage.

4.2. Production process

Due to the limited available space at NSH, an alternative location for production stream processing needs to be identified. However, connecting NSH to a new site poses challenges due to the protected Natura 2000 area surrounding NSH (Figure 4.3). Environmental experts from NAM have determined that installing new pipelines in this area is unfeasible. Fortunately, there is an existing NAM pipeline connected to the NSH site, which provides a potential corridor for reuse. Reusing an existing pipeline corridor could streamline the permitting process and could potentially save cost.

Figure 4.4 illustrates the active natural gas pipeline linking NSH to NAM's well pad at a nearby field (NRB). Additionally, this pipeline connects to two parallel, decommissioned NAM natural gas pipelines that terminate in the Port of Rotterdam. At the end of these pipelines lies a 120,000 m² location currently labeled as "temporarily closed" on Google Earth. This location will be referred to as "PoR" moving forward. Notably, PoR is situated near the H_2 backbone in the Port of Rotterdam, a significant future H_2 hub. Furthermore, several large gas-fired power plants are in close proximity to PoR.

The pipeline corridor connecting these three locations will be a promising opportunity to form an integrated processing system where:

1. The injection stream is metered and compressed (1st stage) at PoR and transported through a 10.5 km bidirectional pipeline to NSH.
2. The injection stream is further compressed (2nd and 3rd stage) and injected into the reservoir at NSH.
3. The production stream arrives to the surface at NSH and is transported through the bidirectional pipeline to PoR.
4. The produced stream is processed at PoR.
5. The processed seasonal stream is injected into the H_2 backbone and the Dunkelflaute stream is distributed to power plants.
6. The tail gas is recompressed and transported through a separate 8 km pipeline to NRB.
7. The tail gas is reinjected into NRB.

Note that a bidirectional pipeline connecting PoR and NSH is conceptually possible as injection and production will never occur simultaneously.

Figure 4.3: The NSH well pad (green square) and its location near the Natura 2000 zone (light green) [55]. NAM's existing natural gas pipeline is indicated by the purple line.

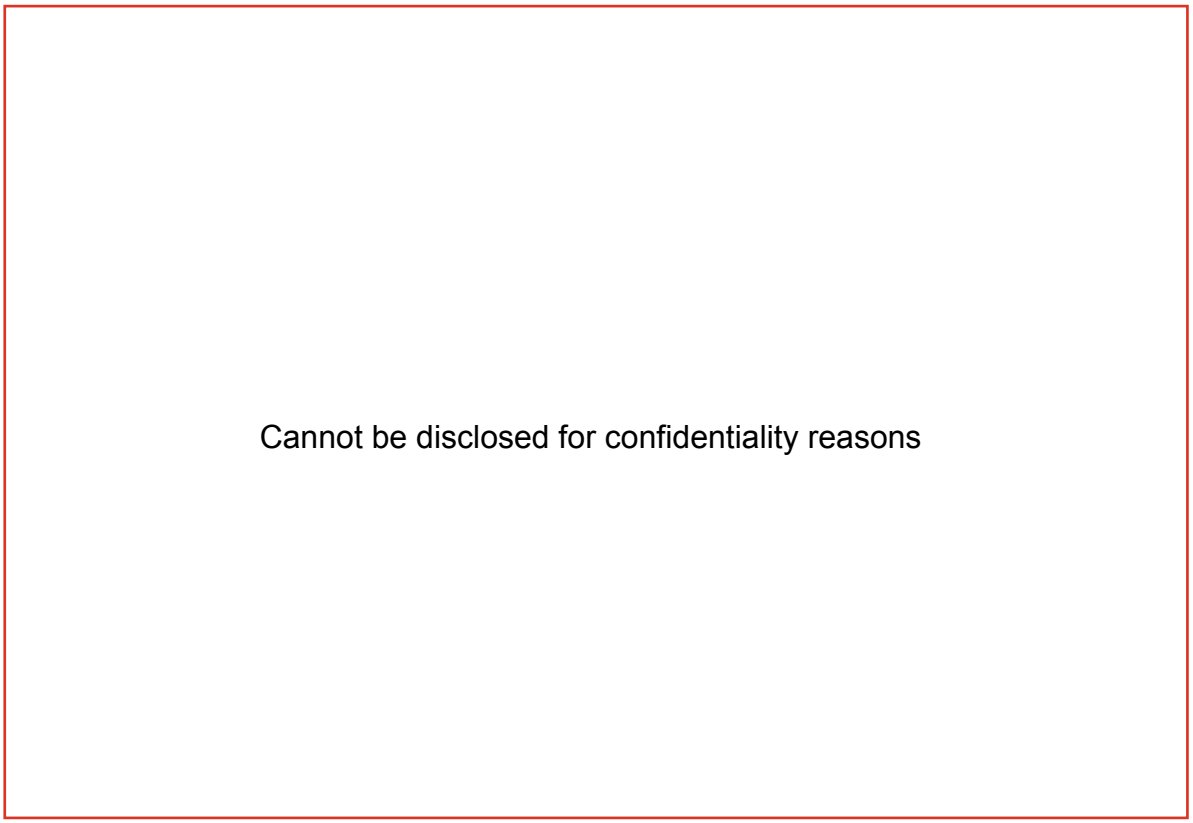

Figure 4.4: NSH, PoR and NRB and their connection through existing natural gas pipelines (indicated by the green lines) [5].

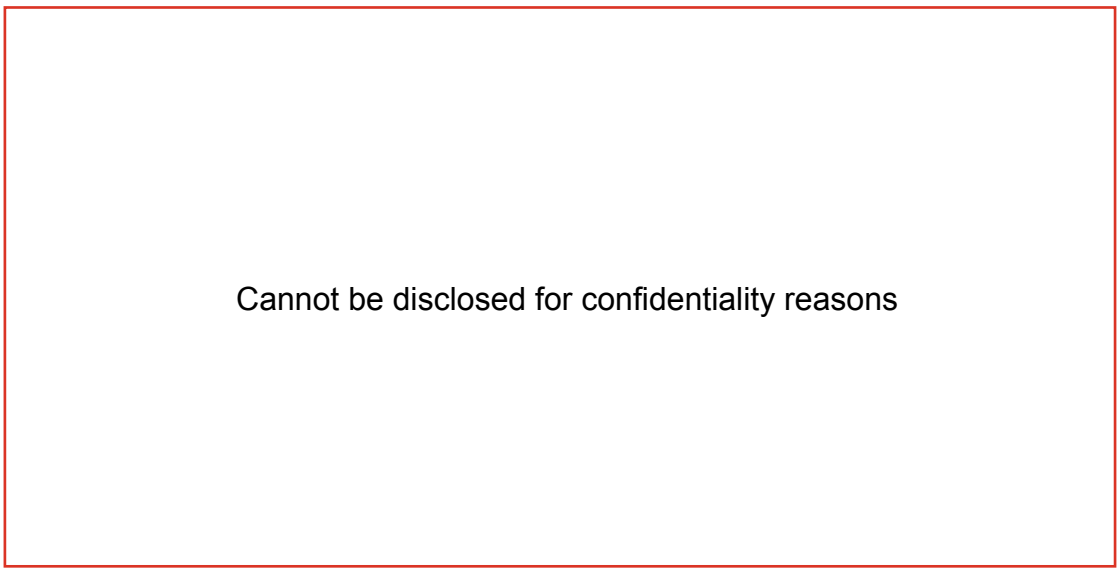

Figure 4.5: The hypothetical processing location in the Port of Rotterdam [26].

4.2.1. Production wells

According to estimates provided by Shell's Production Technologists, each well in NSH would be capable of producing 6.8 M Nm³/d at the lower end of the working pressure range (150 bara). Consequently, using 2 wells would suffice to achieve the seasonal production rate of 9.57 M Nm³/d. These same wells will serve the purpose of injection (9.73 M Nm³/d). Similarly, 8 wells would be required to achieve the Dunkelflaute production rate of 54.24 M Nm³/d. For the reinjection of the small tail gas stream (max. 0.90 M Nm³/d) into NRB, one well is included in the scope. Given that the Dunkelflaute use case allows for larger impurities compared to the seasonal use case, there is an opportunity to optimize the placement of production wells within the reservoir. Specifically:

- 2 wells serve a dual purpose of injection and seasonal production allowing for the highest purities.
- 8 Dunkelflaute wells could be strategically drilled further away from the injection wells, where there is more mixing with cushion gas and in-situ gases.

The following schematic illustrates this concept:

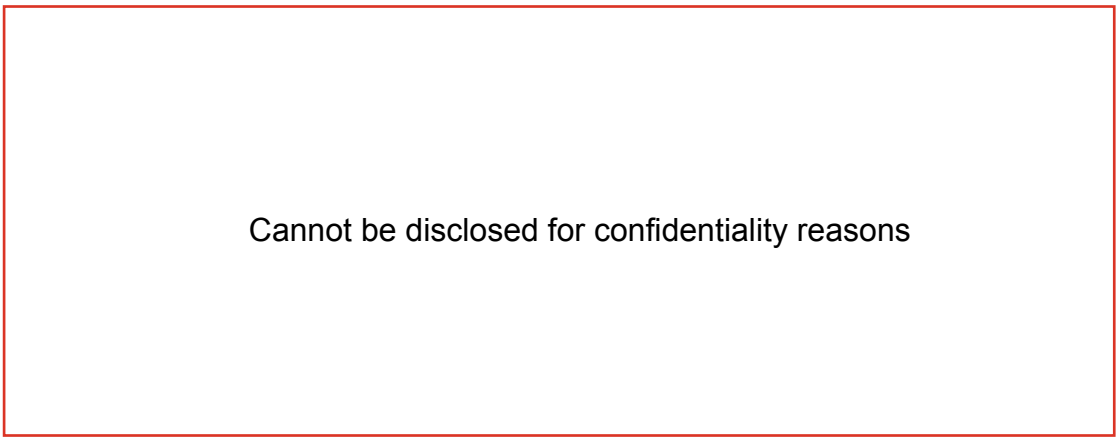

Figure 4.6: Conceptual placement of wells in the reservoir.

4.2.2. Gas processing

The production streams reach the surface at NSH at a pressure of 60 bar. From here, both streams (seasonal and Dunkelflaute) are transported through the 10.5 km 24-inch bidirectional pipeline to PoR. The large Dunkelflaute stream will experience larger pressure drops during transport and processing than the seasonal stream. CCET is used to estimates process equipment parameters based on the Sour Gas processing archetype, with adjustments made to input parameters for UHS operation instead of conventional natural gas processing. The larger flow rates of the Dunkelflaute stream and the larger feed pressures of seasonal stream (due to smaller pressure drops) are used to ensure that the facilities can serve both purposes.

Gas/liquid separator

Upon arrival at the inlet section, the streams pass through a gas/liquid separation unit where free liquids are removed. The separated water is treated, metered, and pumped overboard. A water production of 3 m^3/h is assumed (Shell internal source).

Cooling

Subsequently, the liquid free gas is air cooled from 75 °C to 40 °C to protect facilities downstream.

Mercury bed

Following the cooling step, the streams are sent to a mercury bed to remove trace amounts of mercury, which can lead to corrosion and/or embrittlement to aluminium components downstream [60].

H_2S removal

Next, H_2S is removed from the sour gas. There is a large uncertainty in the H_2S concentration which may be formed during subsurface reactions. With current knowledge, a concentration between 10 ppm and 1000 ppm is expected in the production streams (Shell internal source). Normalising production rates to reflect a continuous (365 day) process leads to an average production rate of 4.4 M Nm³/d. According to Figure 4.7, a Redox and Biological processes would be selected. Based on this figure and SRN-04744 [11], the Thiopaq unit emerges as the optimal choice in terms of both CAPEX and OPEX. Thiopaq units have a proven track record in non-continuous processing within the biogas industry [11]. However, it is essential to consider the potential risk posed by the sudden Dunkelflaute production stream when implementing this technology.

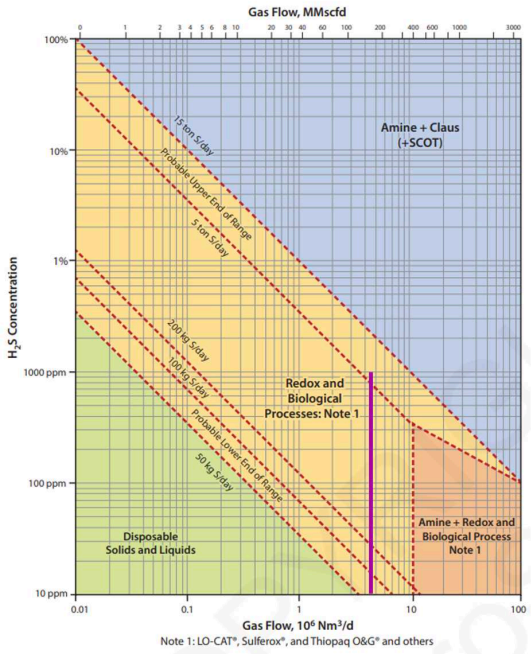

Figure 4.7: H_2S removal selection options [61]. This purple line indicates the normalised production rate and the uncertainty in H_2S concentration.

PSA

When the H_2S is removed, the residual non-H_2 gases are separated in a Pressure Swing Adsorption (PSA) unit [3]. However, the selection of a separation technology can be further refined during the subsequent study phases. Pressure swing adsorption is a gas separation technique commonly used for H_2 purification in which specific components of a gas mixture selectively adhere to the surface of adsorbent materials. The absorbent can be regenerated by adjusting the system pressure [27]. As the Dunkelflaute use case does not require H_2 backbone spec purities, this stream will bypass the PSA. Therefore, only seasonal use case parameters are used for the sizing of the PSA.

Dunkelflaute dehydration

The Dunkelflaute production stream will share the same equipment as the seasonal stream until it exits the Thiopaq unit. Since the Dunkelflaute stream allows for impurities, a PSA can be bypassed. However, the gas will still need to be dehydrated to remove gaseous water. This dehydration process is performed using a Temperature Swing Adsorption (TSA) unit. While a Triethylene glycol (TEG) unit is commonly used for gaseous water removal, a TSA performs better under intermittent conditions, making it the suitable technology for UHS. A TSA unit is not available in CCET, and therefore, sizing estimates are not provided in this study. However, to estimate CAPEX for a TSA, a TEG unit is included in CCET. With the current state of technology, there is not a noticeable difference in type 0 cost between TEG and TSA. Before distribution, the Dunkelflaute stream is metered on the processing site.

Produced tail gas treatment and reinjection

The tail gas separated in the PSA unit exits the facility at near-atmospheric pressure (1.3 bara). Not only does the amount of tail gas produced vary over the years of operation, but it also increases during a production cycle. Furthermore, the tail gas composition inconsistent and predominantly contains H_2 due to the PSA's H_2 recovery efficiency of 92%, as suggested by a vendor. This inconsistency poses a significant challenge in identifying a suitable destination, and this topic has already received considerable attention without a without a well-defined solution. For the reference case, the entire tail gas stream will be reinjected into NRB. It is assumed that the tail gas is reinjected into NRB at 50 bara. Therefore, after exiting the PSA, the tail gas is recompressed and metered before being transported through an 8 km, 8-inch pipeline through the existing corridor from PoR to NRB, where it is injected. According to NAM, the current reservoir pressure in NRB is roughly 25 bara. By 2028, it will have been depleted to 20 bara. NRB is a large reservoir with 9.9 BCM GIIP.

Compression/ cooling stage	**Inlet pressure** [bara]	**Inlet temperature** [°C]	**Discharge pressure** [bara]	**Discharge temperature** [°C]
Compression stage 1	1.3	40.0	3.3	154.0
Inter-stage cooler 1-2	3.3	154.0	2.9	40.0
Compression stage 2	2.9	40.0	7.3	154.0
Inter-stage cooler 2-3	7.3	154.0	6.9	40.0
Compression stage 3	6.9	40.0	18.2	154.0
Inter-stage cooler 3-4	18.2	154.0	17.8	40.0
Compression stage 4	17.8	40.0	51.0	170.4
Aftercooler	51.0	170.4	50.8	107.0*

* The reservoir temperature of NRB is roughly 107°C.

Table 4.2: Summary of the tail gas compression system at EOC (the end of the 6th production cycle). Designed in CCET. One compressors will be required for the tail gas flow rate.

It is important to note that the scope definition and cost estimate assume the use of reciprocating compressors for tail gas compression, as also assumed for the injection compressors. However, due to the large inconsistency in tail gas production as compared to the injection stream, the required duty for the compressors varies significantly. Reciprocating compressors hold an advantage over centrifugal compressors in terms of volumetric flow control. Typically, reciprocating compressors can achieve a turndown ratio of up to 80% [67]. Nevertheless, current technology may not be well-suited for the

intermittency and variability of tail gas composition and therefore mass flow rate, raising questions about its applicability for UHS tail gas recompression. Further study is necessary in this regard and the cost estimate should not be taken strictly.

This reference case requires limited recompression of the tail gas and by reinjecting in a different field, it 'cleans' the store at NSH over time. However, this case also comes with downsides. Four other concepts are compared in Chapter 8. This comparison follows from a study by UK-based engineering company Costain [16] to explore potential destinations for this tail gas. The favoured options based on the study are as follows:

1. Recovery of the residual H_2 in the tail gas using cryogenic separation with reinjection of the non-H_2 gases.

2. Recovery of the residual H_2 in the tail gas using cryogenic separation with blue H_2 as destination for the non-H_2 gases.

In Chapter 8, the first option is explored. This option is compared with the reference case, where no recovery of residual H_2 is considered and the entire tail gas stream is reinjected into the NRB. The second option is not addressed in this report due to its commercial complexity arising from the inconsistent nature of the stream.
Figure 4.8 illustrates the production process flowchart for the reference case.

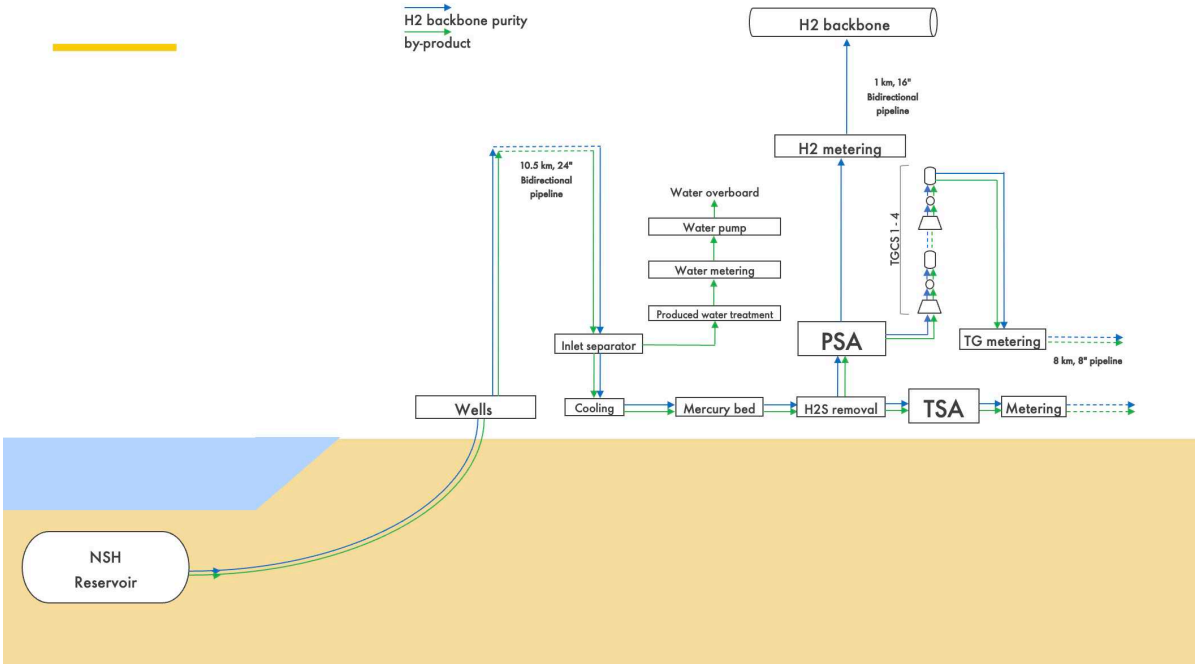

Figure 4.8: Production process flowchart for the reference case. TGCS denotes a tail gas compressor stage.

4.3. Integrated system

Figure 4.9 depicts the process flowchart of the integrated system in the reference case [A], illustrating the division of the scope across three locations: NSH, PoR, and NRB. Table 4.3 provides a detailed breakdown of the integrated system scope which is used for CAPEX estimates in Chapter 5. It categorizes the scope into three components: those included in the injection side using CCET, those included in the production side using CCET, and separate estimations using alternative methods.

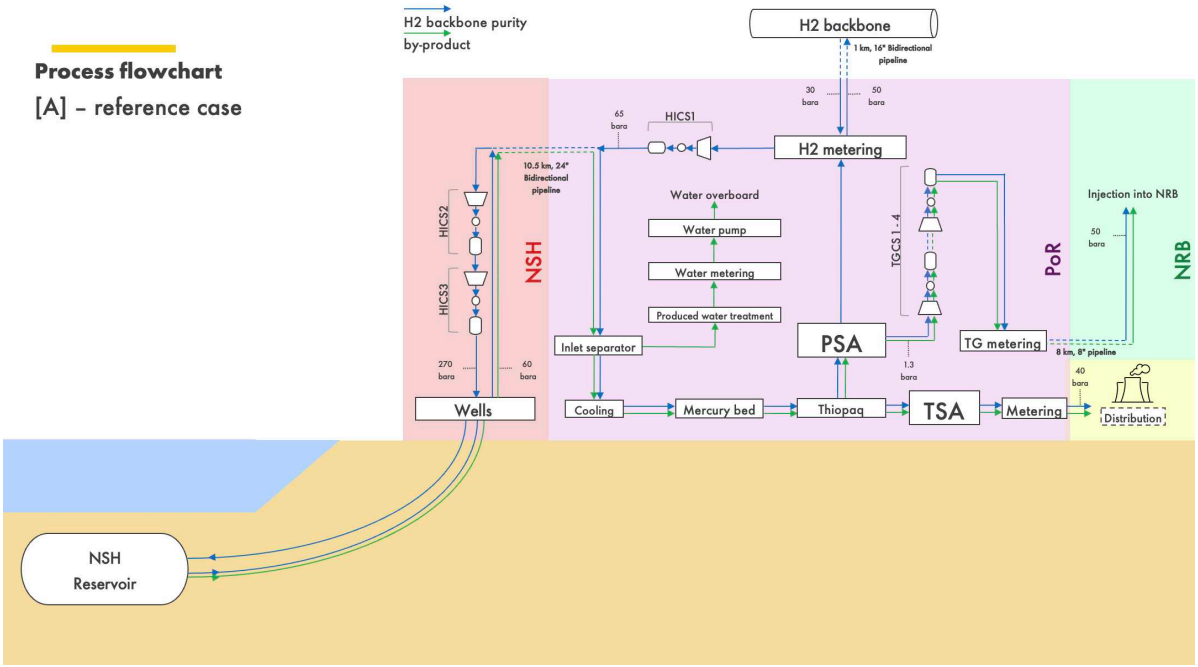

Figure 4.9: Process flowchart for integrated system of reference case [A].

Scope item	Injection process (CCET)	Production process (CCET)	Separate CAPEX estimates
Bi-directional pipeline H_2 backbone – PoR	X		
H_2 metering	X		
HICS1	X		
Bi-directional pipeline PoR - NSH	X		
HICS2 – HICS3	X		
Injection wells			X
Production wells			X
Well pad facility NSH		X	
Inlet (gas/liquid) separator		X	
Produced water treatment		X	
Water metering		X	
Water pump		X	
Gas cooling		X	
Mercury bed		X	
Thiopaq H_2S removal			X
PSA			X
Tail gas compression		X	
Tail gas metering		X	
Pipeline PoR - NRB		X	
Well pad facility NRB		X	
Tail gas injection well			X
TSA (TEG)		X	
Dunkelflaute metering		X	
Cushion gas			X

Table 4.3: Breakdown of scope into CAPEX estimation categories.

5

CAPEX estimation

This chapter provides an overview of the capital expenditures (CAPEX) estimated for the development of the commercial scale UHS facility using the NSH reservoir. The CAPEX estimation uses CCET type 0 cost estimates for most of the components within the project scope. However, PSA, Thiopaq H_2S removal, wells, and cushion gas are estimated alternatively as these components are not covered within the CCET software. Note that this chapter refers to the reference case [A]. CAPEX estimates for the different concepts are included in Chapter 8. All CAPEX is estimated in U.S. dollar (USD).

5.1. Injection process

Type 0 cost estimates have been developed for the injection process from the Capital Cost Outlook (CCO) as of Q1 – 2024. The final investment decision (FID) time considered is January 2035. Below, a summarized overview of the injection process CAPEX is presented.

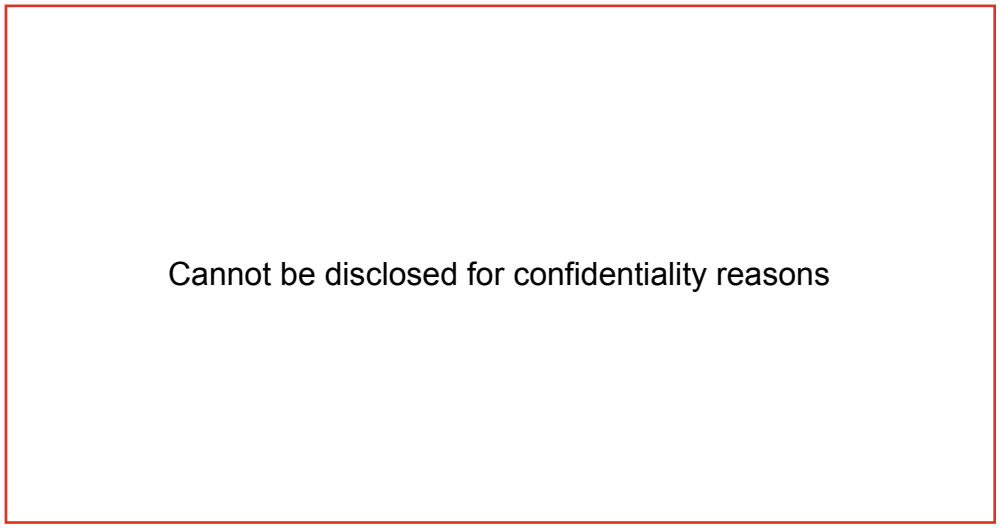

Figure 5.1: Summary of CAPEX for the injection process of reference case [A].

The Engineering, Procurement and Construction (EPC) Base Estimate is categorized in Figure 5.2.

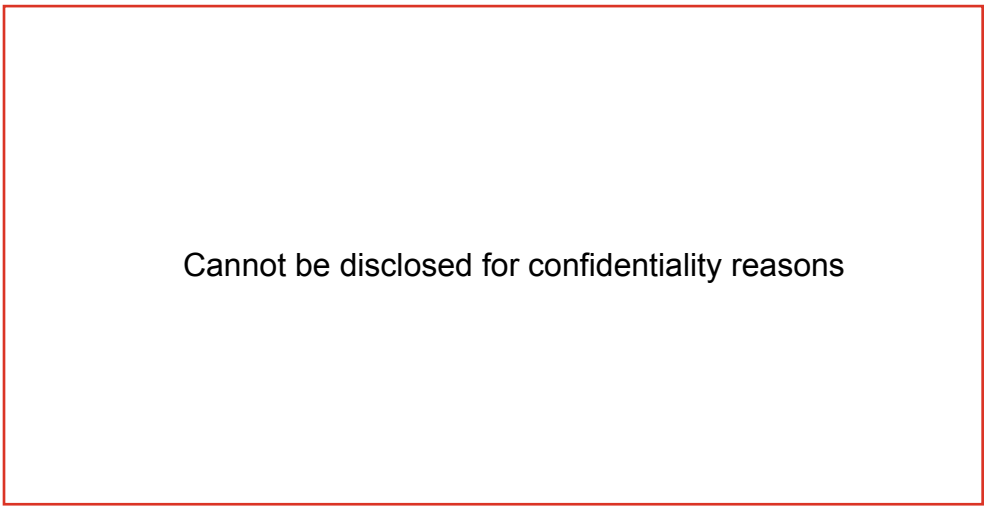

Figure 5.2: Breakdown of EPC estimate for the injection process of reference case [A].

5.2. Production process

Type 0 cost estimates have been developed for the production process from the Capital Cost Outlook (CCO) as of Q1 – 2024. The final investment decision (FID) time considered is January 2035. Below, a summarized overview of the production process CAPEX is presented.

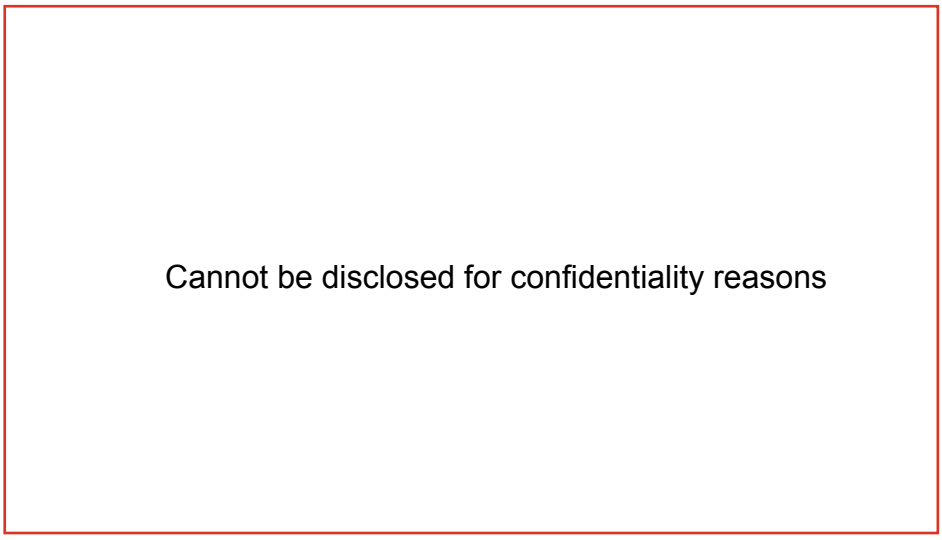

Figure 5.3: Summary of CAPEX for the production process of reference case [A].

The Engineering, Procurement and Construction (EPC) Base Estimate is categorized in Figure 5.4.

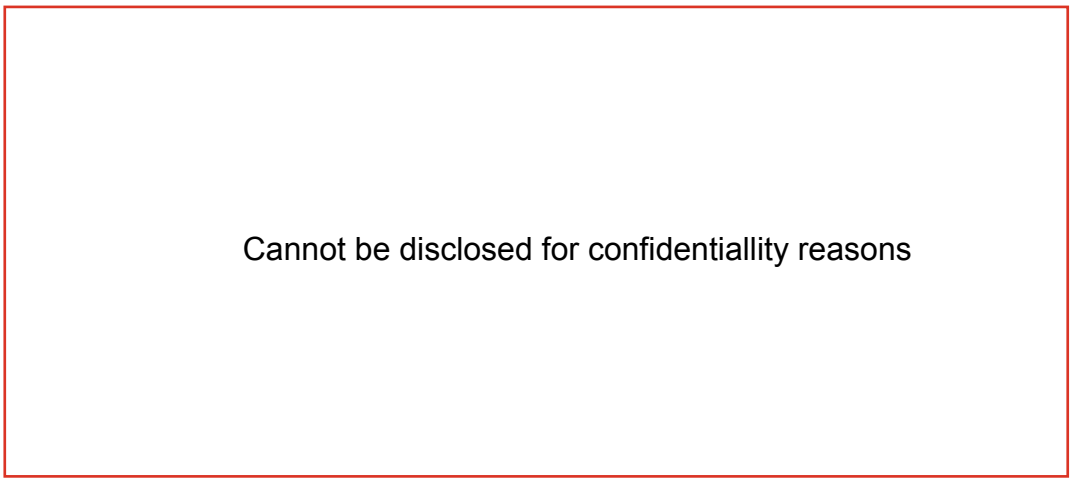

Figure 5.4: Breakdown of EPC estimate for the production process of reference case [A].

5.2.1. PSA

To estimate PSA CAPEX. The CAPEX estimated by a vendor is scaled down by proration using the difference in flow rates. The quote estimated a cost of Cannot be disclosed for confidentiality reasons for a feed flow rate of 70 M Nm³/d with an inlet pressure of 55 bara. The similar inlet pressure allows for proration based on flow rate only using a Shell standard exponential factor of 0.8. To stay consistent with CCET, so to include all cost apart from the major technical components, a lang factor of 4 is applied based on SRN-04205 [3]:

(5.1)

5.2.2. Thiopaq H_2S removal

In SRN-04744 [11], a CAPEX of Cannot be disclosed for confidentiality reasons is determined for a case in which 100 ppm of H_2S is assumed for a working volume of 1.6 BCM. Assuming the same concentration of H_2S, the yearly H_2S production is approximately the same, considering a similar working volume (1.54 BCM in this case). Consequently, in this study the same CAPEX is used and multiplied by a lang factor of 4:

(5.2)

5.3. Wells

In this study, well-performance analysis and cost modeling were not conducted. However, to incorporate the wells into the CAPEX estimation, an assumption of Cannot be disclosed for confidentiality reasons per well was made based on input from NAM. The installation of 2 injection wells (which also serve as seasonal production wells), 8 Dunkelflaute wells and 1 tail gas well would lead to a total Cannot be disclosed for confidentiality reasons. It is important to note that further work is required to obtain a more accurate, case-specific estimate. For instance, using a smaller tubing size to accommodate low flow rates in the tail gas well may result in reduced CAPEX, however, addressing hydrogen-related mechanisms that can cause leaks may require larger investments than conventional natural gas wells. Additionally, the potential for reuse is limited due to differing design requirements. [73].

5.4. Cushion gas

To achieve the desired pressure range, it is necessary to inject cushion gas into the gas field, raising the pressure from 9 to 150 bara. In this case study, H_2 has been chosen as the cushion gas, and an estimated volume of approximately 2.30 BCM (normal conditions) of H_2 will be required.

Cushion gas volume	2.30 BCM
Cushion gas mass	207.7 M kg
H_2 price	4.4 USD/kg [3]
Cushion gas cost	**909 M USD**

Table 5.1: Cushion gas cost estimate.

5.5. Total CAPEX estimate

Considering the CAPEX estimates provided in the preceding sections, it is possible to estimate the total CAPEX for a commercial-scale UHS at NSH under the reference case concept. Please note that market escalation and inflation numbers provided in the CCET CAPEX summaries are not factored into the total CAPEX summary in Table 5.2. To enhance the transferability of these estimates to different timeframes and locations, 'Project P50 Estimate' CAPEX is considered instead. Likewise, market escalation and inflation are not considered for CAPEX estimation of the PSA, Thiopaq, wells, and cushion gas.

Cannot be disclosed for confidentiality reasons

Table 5.2: Summary of total CAPEX, broken down based on the section in this chapter.

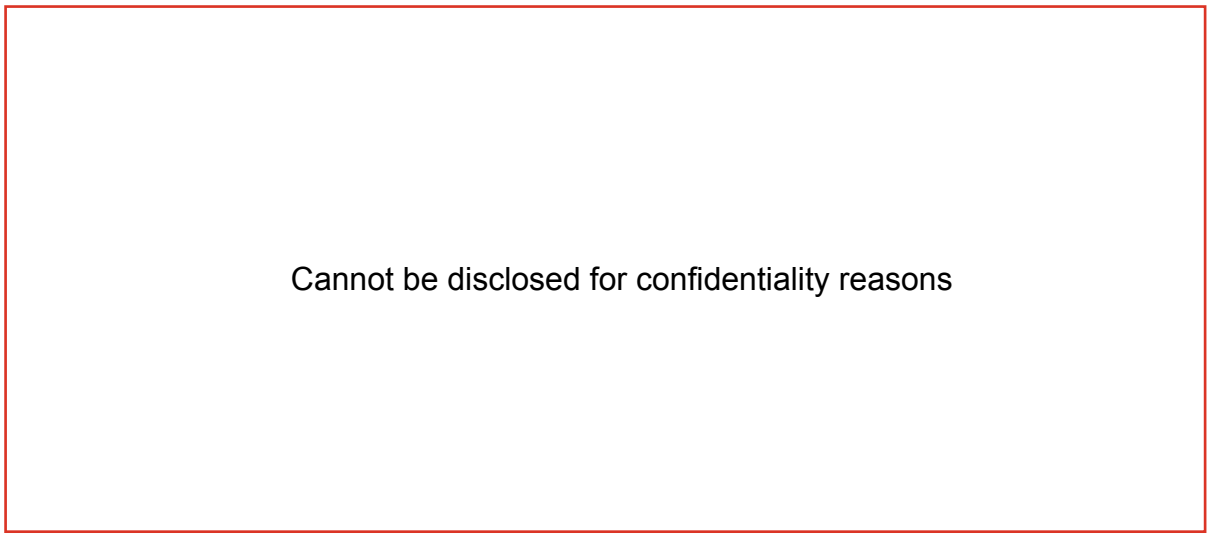

Figure 5.5: Summary of total CAPEX, broken down into scope categories.

6

Electrical energy consumption

The compression system responsible for injecting H_2 into the storage reservoir is a significant energy consumer within the NSH UHS case study. During the injection cycle in year 6, the electrical energy consumption for this compression system is calculated. The energy consumption by the tail gas compressors is also included. A 10% margin is factored into account for electrical energy consumption in other units of the UHS facility. For the tail gas, the flow rate is assumed to be constant over the production cycle. In reality, the flow rate will slightly increase (approximately 13%) as indicated in Figure 3.9. The flow rate at the end of the cycle is used for calculation. The small tail gas stream is assumed to not raise the pressure in NRB (9.9 BCM GIIP) significantly, therefore a constant injection pressure for the tail gas of 50 bara is assumed. As previously discussed, the UHS operation assumes a working pressure range of 150–250 bara. However, to supply the Dunkelflaute use case, which occurs predominantly during autumn and winter, the store will not be fully depleted after summer. Consequently, when the injection cycle begins, it is likely that injection will commence when the store is still approximately 50% full (as shown in Figure 3.6). This results in a store pressure of roughly 200 bar at the start of the injection cycle. To account for the pressure drop in the well tubing and near-well bore area, H_2 will be injected at a pressure of 220 bar. Similarly, when injecting against an almost filled storage, compression up to 270 bara is necessary. As Dunkelflaute production decreases the store pressure during injection, taking the arithmetic mean of the power consumption at 220 bar and 270 bar would overestimate the energy consumption. Therefore, the total electrical energy consumption in year 6 is estimated as follows:

$$E = \left(P_{220} * \frac{2}{3} + P_{270} * \frac{1}{3} \right) * \text{ hours }_{inj} \tag{6.1}$$

SOC: 29.5 – 220 bara	
Flow rate	9.73 M Nm³/d
Power	31.0 MW
EOC: 29.5 – 270 bara	
Flow rate	9.73 M Nm³/d
Power	34.6 MW
Yearly injection hours	3984
Electrical energy consumption year 6	**128.2 GWh**

Table 6.1: Electrical energy consumption of injection compressors in year 6.

SOC: 1.3 – 50 bara	
Flow rate	0.90 M Nm³/d
Power	5.6 MW
EOC: 1.3 – 50 bara	
Flow rate	0.90 M Nm³/d
Power	5.6 MW
Yearly injection hours	2160
Electrical energy consumption year 6	**12.1 GWh**

Table 6.2: Electrical energy consumption of tail gas compressors in year 6.

Electrical energy consumption compressors	140.3 GWh
10% margin for remaining energy consumption	14.0 GWh
Total electrical energy consumption year 6	**154.3 GWh**
„ as % of energy content in stored H_2 working volume	**3.3%**

Table 6.3: Total yearly electrical energy consumption, based on year 6.

7

OPEX

Using the estimated CAPEX and Shell standard percentage factors, the OPEX for a NSH UHS development are determined. Power import from the electricity grid constitutes a significant OPEX component. Power import expenditure is estimated separately based on electrical energy consumption calculations outlined in Chapter 6. For this estimation, a tariff of 100 USD/MWh is assumed. Additionally, the costs related to replenishing the cushion gas due to the disposal of tail gas at NRB are factored into the analysis. The calculation assumes the replenishment flow rate specific to year 6 (0.45 M Nm3/d) and a H_2 cost of 4.4 USD/kg. However, it is important to note that since the tail gas stream is largest in year 6, this cost will be lower in other years. Therefore, extrapolating it to the entire lifetime of the storage facility should be interpreted as an overestimate. The OPEX calculation is based on a pre-tax, undiscounted cost basis. The estimate for the Levelized Cost of Hydrogen Storage (LCOHS) is based on a 20-year operational lifetime of the store. A H_2 density of 0.08988 kg/Nm^3 is used (Shell internal standard).

Cannot be disclosed for confidentiality reasons

Table 7.1: Summary of annual OPEX estimation for the reference case [A].

Cannot be disclosed for confidentiality reasons

Table 7.2: Summary of OPEX per unit H_2 stored for the reference case [A].

Cannot be disclosed for confidentiality reasons

Table 7.3: Summary of the LCOHS for the reference case [A].

8

Concept comparison

In this chapter, a concept is considered where the tail gas stream is reinjected into NSH (instead of NRB). Additionally, Costain's [16] recommendation to recover residual H_2 from the tail gas is considered. To facilitate this comparison, identical export flow rates into the H_2 backbone for the seasonal use case are set (8.67 M Nm3/d). The analysis will reveal variations in required CAPEX and OPEX. Furthermore, opportunities and challenges associated with each concept are identified, which serve as recommendation for further study.

8.1. [B]

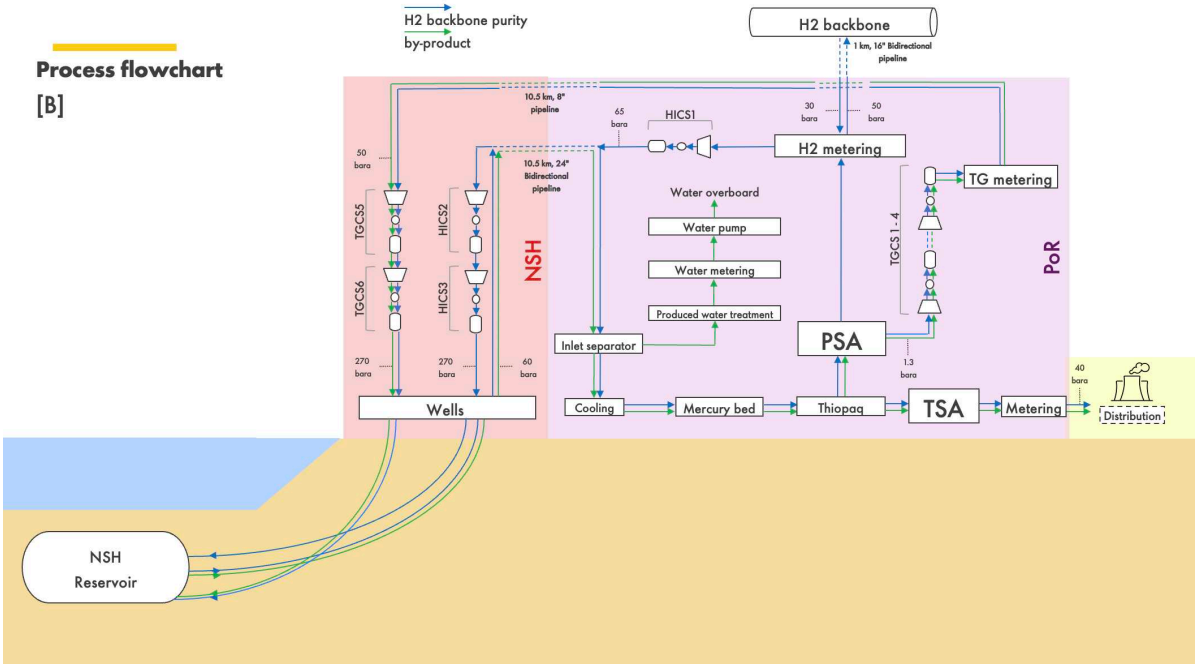

Figure 8.1: Process flowchart for concept [B].

In this concept, the tail gas is reinjected into NSH. Compared to the reference case, this approach necessitates a lower injection rate since the tail gas is recycled, forming a closed-loop system. Consequently, the tail gas is not merely discarded, and replenishment with costly H_2 from the H_2 backbone is not required to maintain the store within its operational pressure range. By limiting the operation to only two sites instead of three, the overall complexity of the system also decreases. Additionally, utilizing the same pipeline corridor for the connection between PoR and NSH could potentially reduce

pipeline CAPEX. It is worth noting that corridor reuse was not considered in CCET, but estimating this cost reduction requires further study. However, injecting into the same reservoir introduces challenges. The tail gas must be compressed to a much higher pressure (up to 270 bar at the start of the production cycle, as opposed to 50 bar at NRB) due to the substantial backpressure in the UHS store. This requirement necessitates additional compression stages. Furthermore, the small well pad at NSH may not be able accommodate these compressors. Lastly, this concept does not inherently 'clean' the store over time, potentially preventing purification cost savings after several years of operation. A potential opportunity could involve utilizing the injection compressors to compress the tail gas at NSH. However, due to the significant required turndown ratio of at least 90% (0.90 vs. 9.73 M Nm³/d), this approach may not be technically viable.

8.2. [C]

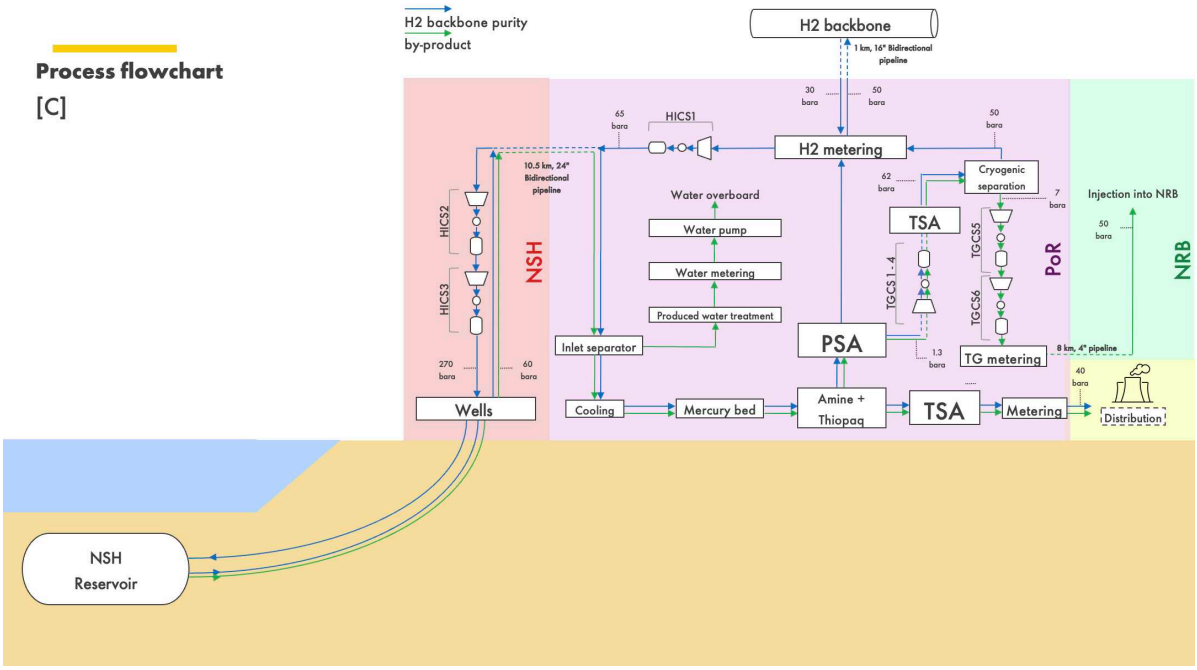

Figure 8.2: Process flowchart for concept [C].

In this concept, cryogenic separation is employed on the tail gas stream to separate non-H_2 gases. Cryogenic separation capitalizes on the extremely low boiling point of H_2, causing non-H_2 gases to liquefy by decreasing temperature, which enables separation. The PSA process achieves an efficiency of 92%, leaving 8% of the H_2 input in the tail gas stream. However, according to Costain's study [16] and literature [1], cryogenic separation can achieve recovery rates as high as 96 to 97%. The resulting H_2 product stream purity can reach 99%, making it suitable for direct integration into the H_2 backbone alongside the PSA H_2 product. This combined approach yields a total recovery rate of 99.76%, significantly higher than the 92% achieved with PSA alone. Consequently, there is an opportunity to recoup the additional CAPEX within a short timeframe.

The CH_4-rich stream exiting the cryogenic separation facility is relatively small (maximum of 0.15 M Nm³/d) and is reinjected into NRB due to commercial complexities associated with this inconsistent stream. One potential destination for this CH_4-rich stream could be blue H_2 production sites, although further investigation is necessary.

The primary challenge in this concept lies in justifying the additional cost of implementing a cryogenic separation facility. Since cryogenic separation is not included in CCET, an estimated CAPEX of 200 USD per tonne per annum (Tpa) is used based on Thunder Said Energy's average for cryogenic separation of oxygen [72]. This estimation uses the yearly tonnage of separated non-H_2 gases (assuming EOC production rate and 365 days): 0.15 M Nm³/d = 54.75 M Nm3/a = 40895 tonnes (0.747 kg/Nm3 is the combined density of the non-H_2 gases) = 8.18 M USD. Applying a lang factor of 4 leads

to a CAPEX of 33 M USD.

Moreover, since this process occurs at cryogenic temperatures to separate non-H_2 gases (approximately -140°C), it is essential to remove H_2O and CO_2 upstream to prevent freezing and potential equipment damage. According to Shell's Gas Treating Guideline (SR.19.01479 [46]), an Amine unit could be used in combination with the Thiopaq unit. The Amine unit removes both H_2S and CO_2 through a chemical adsorption reaction using an amine solvent [61]. The Thiopaq unit will still be needed to treat the acid gas resulting from the adsorption in the amine unit. An amine unit (without regeneration package) is included in CCET to include additional CAPEX. In the cryogenic separation process, maintaining CO_2 concentrations below 50 ppmv is crucial to prevent freezing. However, H_2O must be reduced to concentrations less than 0.1 ppmv [16]. Achieving these low values necessitates a TSA unit with regenerable molecular sieves as the adsorption material. Again, for CAPEX estimation, a TEG unit is incorporated into CCET. The H_2 product exits the cryogenic separator at a pressure close to the feed pressure. However, the CH_4-rich stream exits the cryogenic separator at approximately 7 bara. The expansion of this stream provides cooling for the separation process. Subsequently, recompression is necessary to reinject this stream into NRB.

Considering that the export pressure for the H_2 product into the H_2 backbone is only 50 bara, it is possible to utilize the excess pressure for cooling in the cryogenic separator. This approach would help limit the pressure drop for the CH_4-rich stream. However, detailed modeling is required, and this aspect was not considered in the current study. The pressure in the CH_4-rich product is roughly 7 bara [16].

8.3. [D]

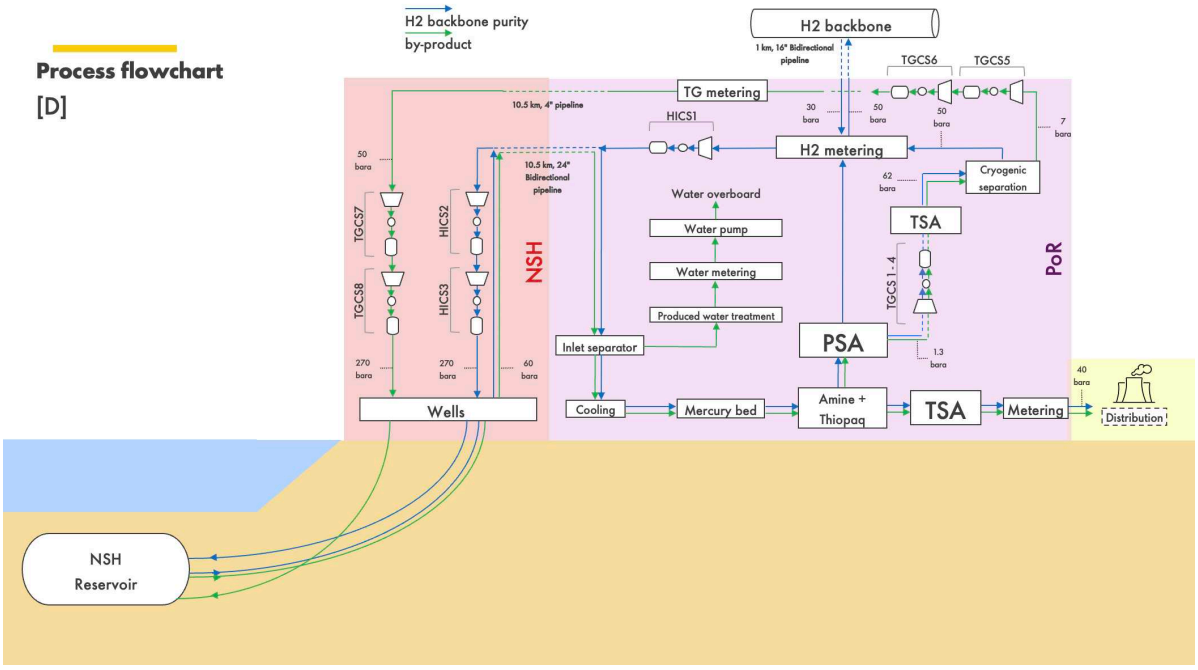

Figure 8.3: Process flowchart for concept [D].

This concept combines the previous two concepts, where cryogenic separation is applied on the tail gas stream and the residual non-H_2 gas is reinjected into NSH. Similar to the previous concepts, this concept has the same benefits of having much larger H_2 recovery rates, a small CH_4-rich stream, no need for replenishment with costly H_2 from the H_2 backbone and decreased complexity by limiting operation to two sites. On the other hand, extra compression and limited space might make this concept unfeasible. Additionally, cryogenic separation, Amine H_2S/CO_2 removal, and tail gas dehydration all involve substantial investments.

8.4. [E]

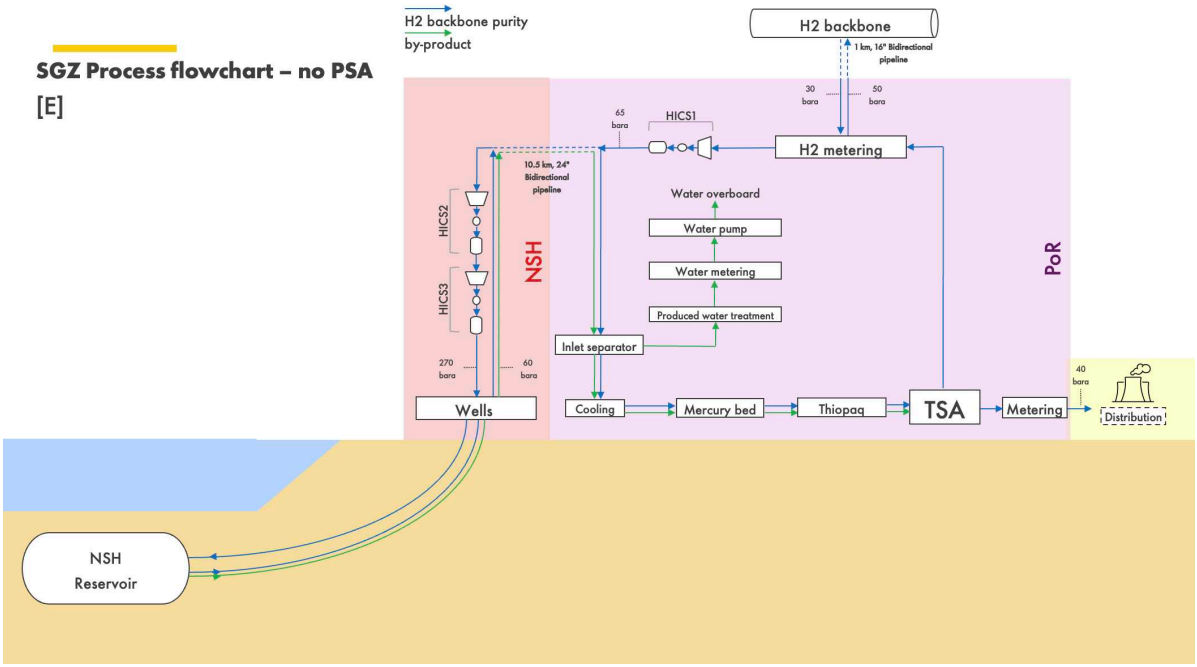

Figure 8.4: Process flowchart for concept [E].

It is evident that achieving a production stream with sufficient purity to eliminate the need for a PSA or cryogenic separation process, while still meeting backbone spec, would be an ideal scenario. However, due to significant uncertainties related to subsurface processes, it remains uncertain whether this concept is realistic. Nevertheless, the low abandonment pressure of the NSH could potentially result in high back-produced purities as gas mixing with in-situ gas will be limited. This concept serves to highlight how enhanced modelling capabilities for subsurface processes, may significantly reduce the project scope and associated CAPEX and OPEX. These cost savings result from eliminating the need for a PSA, tail gas compression, a tail gas pipeline and a tail gas well.

8.5. Comparison table

Concept	H_2 backbone injection flow rate [M Nm^3/d]	-of which replenishment [M Nm^3/d]	seasonal flow rate (max) [M Nm^3/d]	-of which reinjected tail gas (max) [M Nm^3/d]	Dunkelflaute flow rate [M Nm^3/d]	CAPEX [M USD]	OPEX [M USD]	-of which replenishment [M USD]
[A]	9.73	0.45	9.57	0.90	54.24			
[B]	9.28	-	9.57	0.90	54.24			
[C]	9.33	0.05	8.83	0.15	54.24	Cannot be disclosed for confidentiality reasons		
[D]	9.28	-	8.83	0.15	54.24			
[E]	9.28	-	8.67	-	54.24			

Table 8.1: Technical and economic comparison of concepts considered. Note that all concepts assume identical injection period (166 days), production period (14 days Dunkelflaute, 90 days seasonal), and H_2 backbone export rate (8.67 M Nm^3/d).

In Table 8.1, a summary of the concepts is provided, along with estimated values for CAPEX, OPEX including the costs resulting from replenishment of the cushion gas lost from reinjection into NRB. Please note that the flow rates and costs are based on year 6, assuming a H_2 cost of 4.4 USD/kg. In the years before, less mixing will have taken place, and the purity will be higher. Also, after year 6, the purification and replenishment cost are expected to decrease, potentially reaching zero. This reduction is due to the 'cleaned' store potentially achieving purities above the backbone specification. Eventually, there may come a point where a PSA and a cryogenic separator are no longer necessary, removing the need for the entire tail gas scope which leads to significant cost (OPEX) reduction. However, for concept [B] and [D], the store will not self-clean from seasonal production, and a PSA and cryogenic

separator might be required for the entire operational lifetime, unless the Dunkelflaute production results in substantial cleaning. Also, keep in mind that all concepts assume the same production stream composition as given in Table 3.5. In reality, the different tail gas reinjection destinations will result in different purities in the production streams, depending on the well placement in the reservoir.

9

Recommendations

This study serves to identify possible challenges and opportunities related to commercial scale UHS operation using NSH as reservoir. Therefore, comprehensiveness was the objective of the study, rather than precision. To be able to create a comprehensive study within the available time, several assumptions were made. These assumptions, along with the challenges encountered during the study, provide a basis for future research:

- Several facilities cater to both 'seasonal' and 'Dunkelflaute' use cases. Due to significant variations in flow rates and resulting differences in feed pressure, these facilities necessitate substantial turndown ratios. Investigating the technical feasibility of such large turndown ratios is recommended for further study.
- The sizing of facilities to accommodate the Dunkelflaute use case increases CAPEX, and due to the assumed percentage factors, it also impacts OPEX. It is essential to investigate whether the Dunkelflaute use case generates additional income compared to a UHS system that serves only a seasonal use case.
- Further investigation is needed to incorporate the operational downtime of facilities into the cost estimates. Facility OPEX estimates do not consider intermittent operation.
- Although the volumetric flow rate of the tail gas product from the PSA increases only modestly (approximately 13%) between SOC and EOC in this study, the variability in composition leads to a substantial (82%) increase in mass flow rate. Future research should explore whether existing compression technologies can effectively handle this compositional variability.
- This study does not account for the potential re-use of existing well pad facilities or wells at NSH or NRB. Legacy wells could be repurposed for injection and/or production, or as MMV wells to monitor the possible migration of the H_2 plume. Moreover, legacy wells might serve as leakage pathways, and this aspect should be thoroughly assessed for risk mitigation.
- Given the challenges posed by Natura 2000 restrictions, this case study is tailored to existing pipeline corridors. Leveraging these existing routes could potentially lead to cost savings in pipeline CAPEX. It is important to note that the CAPEX estimates provided in this study are specifically for new 'greenfield' pipelines and further study is required to estimate the potential CAPEX reduction.
- For cases [B] and [D], where tail gas is reinjected into the NSH reservoir, separate compressors for tail gas reinjection are currently included in the scope. The injection compressors could possibly also be used for tail gas reinjection during a production cycle. The large turndown as well as variability in gas composition and mass flow rate possibly make this technically unfeasible.
- It is recommended to incorporate the electrical energy required for cushion gas injection into the cost estimates for future study.

- The LCOHS values assume constant OPEX over the years and, as a result, do not account for the benefits of store cleaning. To provide a more accurate assessment, it is essential to incorporate detailed multi-year reservoir simulations into the analysis.
- In the current simulations, only H_2, N_2, CO_2, CH_4 and C_2H_6 are included. However, for a comprehensive analysis, it is essential to conduct more detailed reservoir simulations in future studies. Additionally, accounting for the impact of microbial and geochemical reactions should be part of the investigation.
- It is advisable to conduct reservoir simulations specifically for the NSH reservoir for further techno-economic analysis.
- The Dunkelflaute production stream has the capacity to supply power plants to generate roughly 4GWe. This can be seen as an extreme case. In future study, several scenarios with different utilization fractions for Dunkelflaute can be compared.
- A H_2 price of 4.4 USD/kg assumed. Deviations can have a substantial impact on CAPEX associated with cushion gas filling. More recent projections of future H_2 prices should be incorporated.
- It is recommended to thoroughly investigate alternative cushion gases, such as CO_2. This exploration can significantly impact CAPEX and enhance carbon competitiveness.
- An electricity price of 100 USD/MWh is assumed. Deviations can have a substantial impact on OPEX associated with compression. More recent projections of future H_2 prices should be incorporated.
- Cryogenic separation can enhance H_2 recovery from 92% to nearly 100%. However, additional research is necessary to create an accurate model for this process and to identify the feed stream requirements that impact upstream scope design.
- If NSH becomes a potential target reservoir for a future commercial-scale UHS site, a screening study should be conducted to evaluate potential locations for a processing site, including the one proposed in this study.
- Further research is needed to address non-technical risks related to the NSH well pad location. The significant noise generated by compressors might lead to complaints from nearby residents, while compliance with Natura 2000 regulations could pose challenges for future pipeline operations.
- Reserving NRB as a future destination for tail gas would lead to additional OPEX at NRB once its commercial lifetime for natural gas production concludes. However, by repurposing the field for a secondary function, abandonment costs could be deferred. Further research should investigate the implications and requirements of establishing a tail gas destination at NRB.

10 Conclusion

This report presents the findings of a case study conducted on the existing gas field NSH, investigating its potential conversion into an UHS facility. NSH, with an available storage capacity of 1.54 BCM of H_2 and its proximity to the Port of Rotterdam, stands out as an attractive candidate. However, its high level of depletion necessitates substantial cushion gas volumes to reach operational pressure. Interestingly, this depletion may lead to high purities in the production streams, simplifying the scope and potentially reducing costs. The study aimed to identify challenges and opportunities related to commercial-scale UHS operation using NSH as the reservoir, with the goal to help define objectives for a potential pilot at NSH. Subsequently, this pilot could mitigate risks associated with future large-scale UHS investments. Through a comparison of technical scope and costs across various concepts, the following conclusions were drawn:

- The small well pad at NSH and its surroundings pose a challenge for commercial-scale UHS operation. While the size appears sufficient to accommodate most of the injection-side scope, issues such as compressor noise, multi-megawatt electricity supply, and safety distances make this site more challenging compared to industrial areas.
- The Natura 2000 zones that separate NSH from the Port of Rotterdam present challenges for future pipeline work and site selection for processing facilities. However, existing pipeline corridors connecting NSH, the Port of Rotterdam, and NRB offer opportunities for cost savings and avoiding Natura 2000 zones.
- The Dunkelflaute use case leads to large facility sizing and higher CAPEX due to the substantial flow rates required. However, for most of the year, flow rates would be much lower, rendering these large facilities excessive. UHS operation focused solely on seasonal use would necessitate significantly smaller facilities and lower CAPEX.
- The NRB reservoir is connected to NSH and the Port of Rotterdam via a natural gas pipeline. NRB presents a potential destination for tail gas. Instead of reinjecting the tail gas at NSH, reinjecting it at NRB would gradually “clean” the NSH reservoir over time. This approach would require less recompression and reduce the footprint at NSH.
- The low recovery rate of the PSA, as suggested by a vendor, results in a significant loss of H_2 if the tail gas is reinjected at NRB. Costly replenishment of the cushion gas would be necessary.
- Implementing secondary cryogenic separation on the tail gas stream would recover nearly all the H_2 present. This approach would allow for reinjection of only non-H_2 gases. However, cryogenic separation introduces complexity to both the upstream and downstream scope due to feed gas requirements and compression considerations.
- The large volume of cushion gas required constitutes up to Cannot be disclosed for confidentiality reasons of CAPEX, depending on the chosen concept. Exploring alternative cushion gas options could lead to significant cost reduction.

- Assuming a 20-year operational lifetime, a H_2 price of 4.4 USD/kg, and consistent production stream composition over that period:
  - CAPEX ranges
  - OPEX varies from
  - LCOHS spans from

  Cannot be disclosed for confidentiality reasons

- The concept comparison shows that investing in cryogenic separation for H_2 recovery is worthwhile in a scenario where tail gas is reinjected into a different field (NRB). The LCOHS decreases from. Cannot be disclosed for confidentiality reasons Conversely, if tail gas is reinjected into the UHS reservoir (NSH), cryogenic separation is not a cost-effective investment.
- Cryogenic separation can result in smaller processing facilities due to increased H_2 recovery. With higher H_2 recovery rates, smaller production rates are sufficient to achieve the same H_2 export rates into the backbone. However, this benefit does not apply in our case study because most facilities are designed to handle large Dunkelflaute flow rates.

Concept	NSH footprint	Store cleaning	Scope complexity	LCOHS [USD/kg]	Remarks
[A]	+	+	+/-		- Loss of H_2 - Costly cushion gas replenishment - Tail gas reinjected at 50 bara - H_2-rich tail gas
[B]	-	-	+		- No cushion gas replenishment - Tail gas reinjected up to 270 bar - H_2-rich tail gas
[C]	+	+	-		- Limited cushion gas replenishment - Tail gas reinjected at 50 bara - CH_4-rich tail gas - Smaller seasonal production rates
[D]	-	-	+/-		- No cushion gas replacement - Tail gas reinjected up to 270 bara - CH_4-rich tailgas - Smaller seasonal production rates
[E]	+	N/A	+		- Ideal scenario - No PSA or cryogenic separation - No tail gas

Cannot be disclosed for confidentiality reasons

Table 10.1: Conclusive summary of concept comparison: '+' indicates strengths, '-' indicates weaknesses.

II

H2-Brine Multiphase Flow and Ostwald Ripening in Sandstone Rock: An Experimental CT Imagery Approach

11

Theory

The principle of UHS in porous media is similar to storage of other gases (e.g, CO_2, CH_4). The in-situ pore fluids, which are typically brine and/or leftover hydrocarbons, will be displaced by the injected hydrogen, which will then spread out beneath a low-permeable caprock which is able to prevent the hydrogen from migrating into the overburden. In order to allow for reproduction, a trap structure will hold the hydrogen in place and stop it from escaping laterally [30]. Hydrogen molecules, characterized by lower viscosity, and a greater density contrast with water (brine) compared to CO_2 and CH_4, present an increased chance of uneven gas displacement. However, the higher interfacial tension of hydrogen with water, compared to CO_2 and CH_4 [17], not only mitigates the impacts of these characteristics but also lessens the likelihood of hydrogen escaping through the caprock [64]. Due to the different physical and chemical properties of hydrogen compared to CO_2 and CH_4, storage of hydrogen will result in additional complexity [10] [30] and the multiphase flow characteristics of this novel concept have not yet been thoroughly investigated.

11.1. Relative permeability

Relative permeability is defined as the ratio of the effective permeability of a fluid to the absolute permeability of the rock, which is dependent of the saturation level of the fluid [33]. Due to the heterogeneous pore structure within a rock, it is likely that there is a dissimilarity in saturation profile depending on the direction of saturation changes. This may result in a different relative permeability curve for drainage (reduction of wetting phase saturation) than for imbibition (increase of wetting phase saturation) [33]. This concept is known as hysteresis and must be accounted for depending on the mechanism by which a reservoir is depleted [59]. In a system in which hydrogen and water (or brine) are present in a sandstone rock, water is generally known to be the wetting phase and hydrogen the non-wetting phase [32] [10] [31] [43]. Therefore, in context of UHS, when hydrogen is injected into a water-bearing reservoir, hydrogen displaces the wetting phase. This mechanism can be modeled by a drainage experiment. Contrarily, an imbibition experiment mimics the reproduction of hydrogen, when the in-situ brine flows into previously hydrogen saturated pore space. Both leading to a characteristic relative permeability curve for drainage and imbibition. Although the hydrogen/water/rock system is generally water-wet, the degree of wettability can vary. This variation is due to factors such as the mineral composition of the rock [22], as well as the temperature and pressure conditions specific to the reservoir's depth [39]. These elements affect the contact angles, which serve as a measure of the system's wettability. Wettability refers to the preferential tendency of one of the fluids to spread over the surface of a porous material in the presence of the other fluid [18]. Thus, in a water-wet system, water occupies the smallest pores and throats, coating the surface. The non-wetting phase primarily fills the center of the larger pores [4]. The evidence from multiple studies indicating that water/hydrogen/rock systems tend to be water-wet is advantageous for UHS in porous media as this increases the relative permeability of hydrogen, improving essential aspects like injectivity and recoverability [10]. Recoverability is a parameter that may be limited by capillary trapping of injected hydrogen. This phenonemon is the result of capillary forces that prevents injected hydrogen gas from exiting pore space, leading to

hysteresis in relative permeability functions [10]. Trapping is often described by a snap-off mechanism which occurs during displacement of a non-wetting fluid by a wetting fluid in porous media (imbibition). This is recognized as the accumulation of the wetting phase within the corner layers of a pore throat as it penetrates water-wet porous rocks [71]. The non-wetting layers eventually lose contact with the solid surface, creating an unstable condition where water quickly fills the throat's center [47]. The non-wetting phase will withdraw into the pore body connected to the pore throats. After snap-off happens in all connecting throats to a pore body, the non-wetting phase within that pore body remains stable and resistant to further displacement [68]. Commercial scale UHS would benefit from a lower amount of trapping resulting in a smaller residual gas saturation and thus higher recoverability, as opposed to CCS, where immobile CO_2 is evidently favorable [47].

Relative permeability can be measured experimentally using several methods. There are two fundamental approaches: steady-state and unsteady-state method. For this experiment, the steady-state method is used, in which both wetting and non-wetting fluids are simultaneously injected into the core at different fractional flows. Water saturation and the pressure differential between the core inlet and outlet are measured for each fractional flow once steady-state is reached. Depending on the fluid properties and rock structure, it usually takes a considerable time to achieve a steady-state condition, however, this approach allows simple calculation of relative permeability using the extended Darcy's law. In the unsteady-state method, usually only one phase (typically the non-wetting phase) is injected at a consistent flow rate to displace the other phase (usually the wetting phase) already present in the core [81]. The steady-state method has a larger reliability as capillary equilibrium is maintained, saturation is directly measured, and calculations are based on Darcy's law. The unsteady-state method can be performed more rapidly but introduces numerous uncertainties in calculation methodologies [33].

11.2. Ostwald ripening

One method by which trapped hydrogen can escape from pores is through the phenomenon known as Ostwald Ripening. This process involves a two-phase system gravitating towards its lowest energy state to achieve thermodynamic equilibrium. Energy reduction occurs as the system decreases the interfacial area between the two phases [77]. This decrease in interfacial area occurs in regions in the pore space where there is high capillary pressure (P_c), which is the pressure difference across the interface of two immiscible fluids caused by interfacial tension [12]. This process is as follows: Elevated local capillary pressure induces a higher gas pressure, thereby enhancing the gas's solubility in the aqueous phase according to Henry's law [25]:

$$H = \frac{\partial C}{\partial P_g}, \tag{11.1}$$

where H is Henry's law constant [mol/m^3·Pa], C represents the concentration of gas dissolved in the aqueous phase [mol/m^3], and P_g is the gas pressure [Pa]. Consequently, concentration gradients form, resulting in diffusion of dissolved gas away from areas with high capillary pressure [84]. As a result, bubbles (ganglia) may either decrease in volume or vanish entirely in regions with high capillary pressure, while they expand in areas with low capillary pressure. Equilibrium is established when the capillary pressure becomes uniform throughout the system. In porous media, multiple equilibrium states are conceivable, characterized by a distribution of ganglia exhibiting equal capillary pressure [84] [8]. The timescale [s] for pore-scale equilibrium to develop in laboratory experiments can be estimated using Eq. 11.2 [8]:

$$t = \frac{l^2 r \phi S_{gr} \rho_g}{2DH\sigma m_g}, \tag{11.2}$$

where l is the length over which equilibrium is reached [m], r is the typical throat radius [m], ϕ is the porosity of the rock, S_{gr} is the residual gas saturation, ρ_g is the density of the gas [kg/m^3], D is the diffusion coefficient [m^2/s], σ represents the interfacial tension between the fluids [N/m], and m_g is the molecular mass of the gas [kg/mol].

It can be expected that following Ostwald ripening, ganglia will mostly expand in regions of low capillary pressure, thereby exhibiting larger radii of curvature in accordance with the Young-Laplace equation [8]:

$$P_c = \sigma(\frac{1}{R_1} + \frac{1}{R_2}). \quad (11.3)$$

Here, R_1 and R_2 are the principal radii of curvature of the liquid–gas interface [82]. Ostwald ripening potentially allows for the transition of hydrogen gas from trapped ganglia to large connected ganglia [25], thereby increasing recoverability and therefore feasibility of UHS. Thus, if simulation models are based on laboratory experiments that have not undergone Ostwald ripening, then they overestimate the amount of trapping on a UHS timescale [2]. The process of Ostwald ripening is visually described in Figure 11.1.

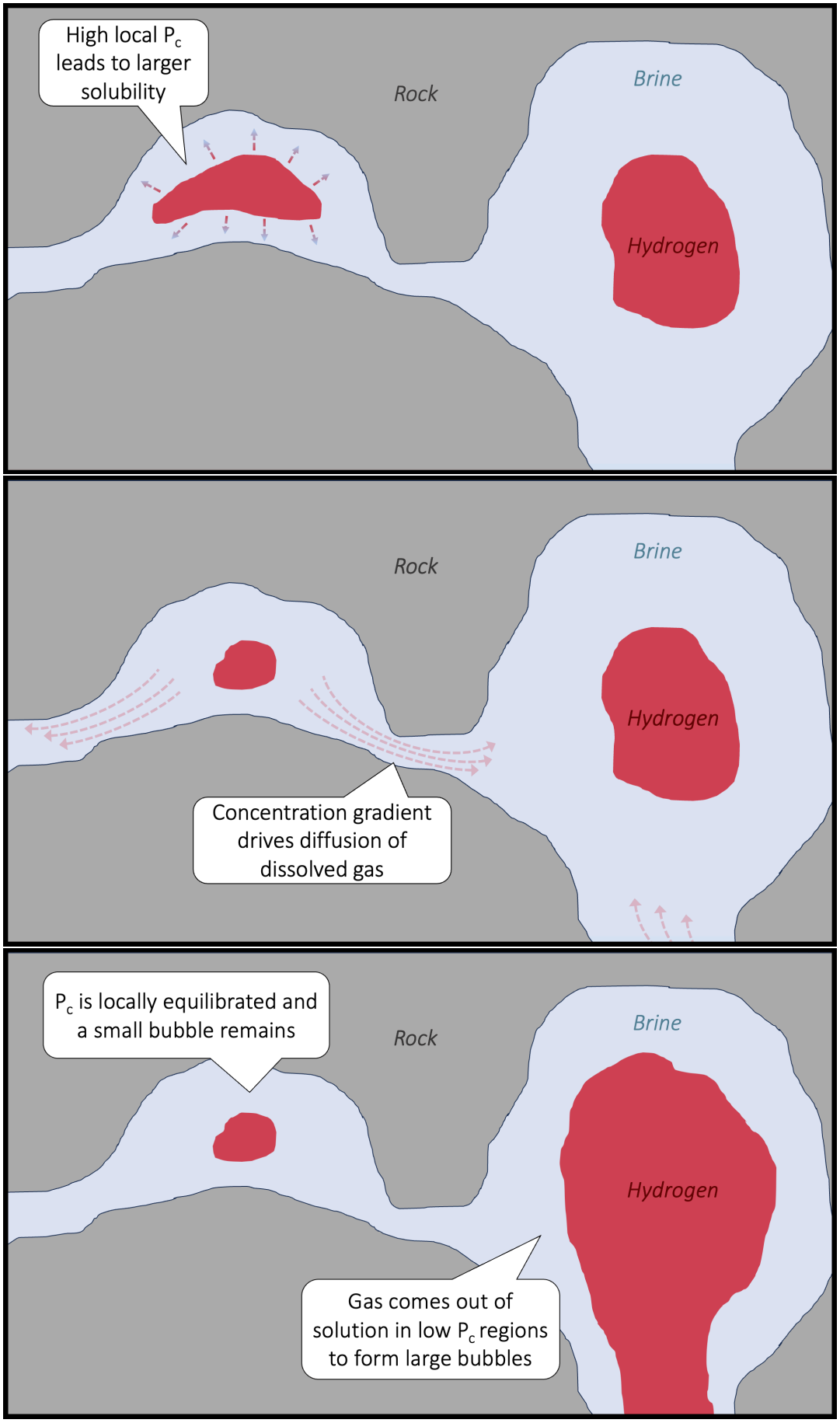

Figure 11.1: A schematic of Ostwald ripening in context of UHS in water-bearing porous rock.

12

Previous studies

The study by Yekta et al. [81] was the first to experimentally determine relative permeability in a hydrogen/water/rock system. Since then, the number of experimental studies has increased rapidly. In these studies, various reservoir conditions (e.g., temperature, pressure) have been used to represent different storage depths, with low temperature and low pressure referring to shallow reservoirs and high temperature and high pressure to deep reservoirs. Comparing these studies is not straightforward due to rock heterogeneity; differences in a rock's pore structure lead to varying capillary forces, which significantly impact fluid movement at low flow rates [81]. Accordingly, rock heterogeneity is demonstrated to influence relative permeability in CO_2-brine and N_2-water systems [63] which was also confirmed to be the case for hydrogen [64]. On the other hand, Yekta et al. [81] suggested that the relative permeability will *not* be largely influenced by changing temperature and pressure within 100 bar and 100^oC, due to a relatively constant viscosity of hydrogen within this range, which is in contrast to a CO_2-water system. This suggests that the depth of a UHS reservoir would not affect the flow capability of hydrogen. However, Higgs et al. [31] suggest that deeper reservoirs might result in a higher hydrogen relative permeability, due to a decreasing interfacial tension with higher temperature [17] and pressure. Contrarily, at high gas saturations, Rezaei et al. [64] have shown that relative permeability decreases with pressure, concluding this must be due to an increased viscosity, while at low gas saturations, they suggest that the large pressure results in a lower interfacial tension, which increases the relative permeability. This second reasoning is a similar to that stated by Higgs et al. [31]. The study by Rezaei et al. [64] shows that pressure can have different effects on relative permeability for different gas saturations, challenging the hypothesis proposed by Yekta et al. [81]. In literature, the relative permeability at the highest gas saturations, also known as end-point relative permeability, is often considered a key indicator, serving as a metric to evaluate the injectivity of hydrogen into the rock. However, from an economic perspective, recoverability is equally, if not more, important than injectivity. Thaysen et al. [71] suggest that shallow reservoirs are more suitable for commercial UHS because their experiment showed more residual trapping at higher pressures, resulting in less recoverability of injected hydrogen. Due to hysteresis, the path of fluid saturation can significantly impact the relative permeability characteristics of both hydrogen and brine. In context of UHS, relative permeability hysteresis has been experimentally studied by Boon and Hajibeygi [10], Lysyy et al. [52] and Higgs et al. [31].

The aforementioned studies demonstrate that hydrogen, in combination with water, exhibits complex flow properties in porous rock. To better understand the behavior of hydrogen in such systems, fluid saturation can be visualized through experiments conducted using CT imaging. Most previous coreflooding experiments were limited to either high-resolution micro-CT imaging on a small core plug [45] [43] [31], or low-resolution medical CT imaging on a large core [10]. This study involves both core-scale imaging of a 17 cm length core and pore-scale imaging in a middle section of the core. A rock sample of this size has never before been analyzed using micro-CT imaging while injecting hydrogen and water/brine. To derive valuable multiphase flow parameters, it is essential for hydrogen and brine to flow through the same pore space. In a horizontal placement of the core, the high-density contrast between the brine and hydrogen phases can potentially result in gravity segregation, as seen in the study by Boon and Hajibeygi [10]. To compare the effect of gravity segregation, this experiment is conducted with a vertically placed rock. An overview of published coreflooding experiments in a system of

hydrogen and water/brine in rock can be found below.

Study	Lithology	Core dimensions [cm] (D) / [cm] (L)	Temperature [°C]	Pressure [bar]	Porosity (%)	Permeability [mD]
Yekta et al., 2018 [81]	Vosges Sandstone	1.5 / 6.1	20-45	55-100	19	44
Jha et al., 2021 [45]	Gosford Sandstone	0.5 / 1.5	20	1	18	-
Al-Yaseri et al., 2022 [80]	Fontainebleau Sandstone	3.9 / 5.5	25	4	10	190
Rezaei et al., 2022 [64]	Sandstones & Carbonate	3.8 / 8.9-9.5	80	1-206.8	10.5-16.4	3-34
Boon and Hajibeygi, 2022 [10]	Berea Sandstone	3.8 / 17	18	100	20	203
Lysyy et al., 2022 [52]	Berea Sandstone	3.8 / 27.6	30	30	18	107
Thaysen et al., 2023 [71]	Clashach Sandstone	0.5 / 5.4-5.7	20	20-70	13-14	-
Jangda et al., 2023 [43]	Bentheimer Sandstone	0.6 / 2.7	50	100	23	2900
Goodarzi et al., 2024 [25]	Bentheimer Sandstone	1.3 / 6.0	25	10	22.6	1400
Higgs et al., 2024 [31]	Bentheimer Sandstone	0.6 / 1.3	25	21.3	23	653
This study	Berea Sandstone	1.0 / 17	25	50	18.3	104

Table 12.1: Rock type and experimental conditions for previous relative permeability and residual trapping studies. Empty fields indicate that the data was either not determined in the study or not provided by the authors. This table is based on data gathered by Higgs et al. [31] and has been modified and extended.

Study	Capillary number range [-]	Displacement methodology	Flow orientation	Imaging technique
Yekta et al., 2018 [81]	1.17-1.25 x $10^{-8\,d}$	Steady-state	Vertical	No
Jha et al., 2021 [45]	2.49 x 10^{-10} - 3.68 x $10^{-8\,i}$	Unsteady-state	Vertical	Micro-CT
Al-Yaseri et al., 2022 [80]	3.54 x $10^{-8\,d}$	Unsteady-state	Vertical	NMR
Rezaei et al., 2022 [64]	-	Unsteady-state	Vertical	No
Boon and Hajibeygi, 2022 [10]	9.1 x 10^{-9} - 1.1 x $10^{-6\,d}$	Steady-state	Horizontal	Medical CT
Lysyy et al., 2022 [52]	1.88 x 10^{-9} - 1.74 x $10^{-7\,d}$	Steady-state	Vertical	X-ray (unspecified)
Thaysen et al., 2023 [71]	1.2 x 10^{-8} - 9.5 x $10^{-6\,i}$	Unsteady-state	-	Micro-CT
Jangda et al., 2023 [43]	4.2 x 10^{-9} - 2.3 x $10^{-6\,d}$	Unsteady-state	Vertical	Micro-CT
Goodarzi et al., 2024 [25]	1.93 x 10^{-7} - 5.79 x $10^{-9\,d}$	Unsteady-state	Vertical	Micro-CT
Higgs et al., 2024 [31]	2.92 x 10^{-7} - 2.92 x $10^{-5\,d}$	Steady-state	Vertical	Micro-CT
This study	1.3 x 10^{-8} - 1.3 x $10^{-6\,d}$	Steady-state	Vertical	Micro-CT

[d] Determined with Darcy velocity
[i] Determined with Interstitial velocity

Table 12.2: Experimental methods of previous relative permeability and residual trapping studies. Empty fields indicate that the data was either not determined in the study or not provided by the authors. This table is based on data gathered by Higgs et al. [31] and has been modified and extended.

Study	Initial gas saturation [-]	Residual gas saturation [-]	Hydrogen end-point relative permeability [-]	Max. pressure drop [bar]
Yekta et al., 2018 [81]	0.59-0.6	-	0.035-0.044	0.9^{D}- 2.0^{D}
Jha et al., 2021 [45]	0.65^{x}	0.41^{x}	-	-
Al-Yaseri et al., 2022 [80]	0.04^{x}	0.02^{x}	-	-
Rezaei et al., 2022 [64]	0.22-0.28	-	0.260-0.360	-
Boon and Hajibeygi, 2022 [10]	0.36^{y}	$0.24\text{-}0.17^{y}$	0.019	0.6^{D}- 4.9^{I}
Lysyy et al., 2022 [52]	0.41^{y}	0.36^{y}	0.037-0.083	0.3^{D}- 4.2^{I}
Thaysen et al., 2023 [71]	0.50-0.53	0.1-0.21	-	-
Jangda et al., 2023 [43]	0.36^{x}- 0.36^{y}	0.20^{x}- 0.25^{y}	-	-
Goodarzi et al., 2024 [25]	0.30^{x}	0.10^{x}	-	-
Higgs et al., 2024 [31]	0.76^{x}	0.40^{x}	0.049	0.1^{D}- 0.9^{I}
This study	0.44^{y}	0.32^{y}	0.043	13.4^{D}- 15.9^{I}

[x] Determined with non-equilibrated brine
[y] Determined with hydrogen equilibrated brine
[D] Drainage
[I] Imbibition

Table 12.3: Results from previous relative permeability and residual trapping studies. Empty fields indicate that the data was either not determined in the study or not provided by the authors. This table is based on data gathered by Higgs et al. [31] and has been modified and extended.

In addition to the flow parameters that can be extracted from coreflooding, high-resolution CT imaging in this experiment allows to study the effects of Ostwald ripening. This phenomenon has not been extensively studied in a hydrogen/brine/rock system. Blunt [8] investigated the time scales to reach equilibrium and its effect on long-term gas storage and laboratory experiments. It has only been observed using high-resolution CT imaging by Zhang et al. [84] and Goodarzi et al. [25]. The primary finding of Zhang et al. [84] was the observation of a notable rearrangement of trapped hydrogen ganglia

following a 12-hour time without flow. The larger ganglia grew in size and the smaller ganglia tended to disappear. The same experiment was performed with nitrogen but no significant rearrangement of ganglia sized was observed. They suggest that Ostwald ripening had not yet had a substantial influence because of a difference in time-scales for each gas. Goodarzi et al. [25] concluded that following a 16-hour period without flow, the hydrogen gathered into larger ganglia, with one large connected ganglion comprising nearly all of the volume.

13

Methods

13.1. Sample

An untreated 17 cm length Berea core, with a diameter of 10.5 mm is used for this experiment. Its pore size distribution is shown in Figure 13.1. The untreated Berea sample is covered with a mixture of viscous adhesive (Rencast CW 2215) and hardener (REN HY 5160-1). After application, it is left to air-dry for a period of 21 hours. This mixture serves to block the penetration of the thinner resin, which is applied later to bond the core to the core holder. From CT imaging, it is observed that the viscous resin slightly penetrates the surface of the core. Therefore, for the (relative) permeability calculations, a radius of 5.0 mm is used instead of 5.25 mm. After the core is sawed to the desired length of 17 cm, it undergoes oven drying at 40°C for 5 hours to eliminate any water that may have seeped into the core during the sawing procedure. Subsequently, the epoxy endcaps connected to the PEEK in- and outlet tubing are glued onto the core. Once dried, the core is inserted into the carbon core holder (Figure 13.2) and a combination of epoxy resin (L20) and hardener (EPH 161) is injected into the voids to isolate the core.

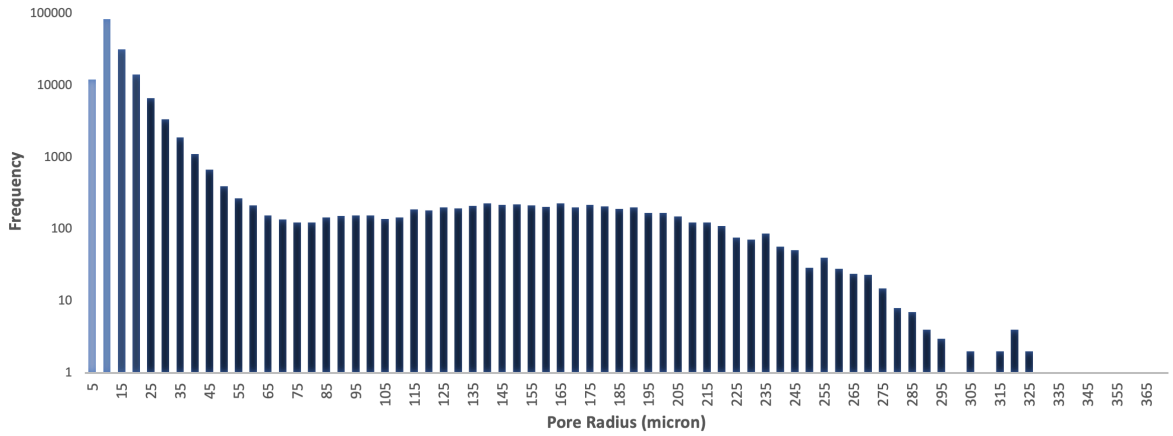

Figure 13.1: Pore size distribution in the Berea sample obtained using a high-resolution CT image of a 1 cm interval. The light blue shade indicates a larger possible error. These pore sizes are close to the voxel size (6.5 micron) and could therefore potentially be attributed to noise.

13.2. Materials and experimental conditions

The experiment is conducted at a pressure of 50 bar and 25°C. The hydrogen gas is produced by Linde-gas Company and has a purity of 99.99 mol%. Degassed 3w% KI brine is used to enhance contrast between the three phases in the CT images. The density of the brine is measured at 25^{o}C and atmospheric pressure resulting in 1019.7 kg/m^3 using a densimeter and 1017.4 kg/m^3 using the

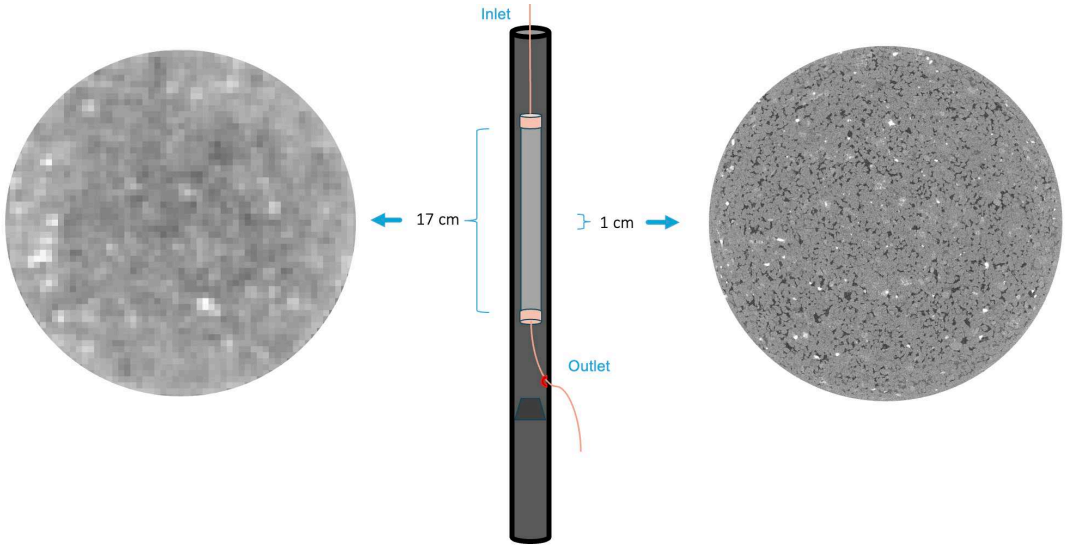

Figure 13.2: Schematic of the 17 cm Berea sample in its carbon core holder. The whole core is scanned at low resolution to extract the saturations. A 1 cm section in the middle of the core is scanned to study Ostwald ripening at the pore scale. The circle represent a raw 2D image of at the respective resolution.

scale density. The mean is used for calculations. The density of hydrogen at 25°C and 50 bar is 3.949 kg/m^3 [57]. The porosity of the core is measured at 18.3% using the slice average of Eq. 13.1:

$$\phi = \frac{CT_{brine} - CT_{dry}}{I_{brine} - I_{air}}. \tag{13.1}$$

Here, the voxel level CT numbers [HU] for the brine saturated and dry core are indicated by CT_{brine} and CT_{dry}, respectively. The CT values [HU] that would have been obtained if air and brine alone had been scanned are I_{brine} and I_{air} [48]. The absolute permeability of the core was determined to be 104 mD (1.03 x 10^{-13} m^2) using Darcy's law for single-phase flow of the KI brine:

$$q = \frac{Ak}{\mu}\left(\frac{\Delta P}{L} + \rho g\right), \tag{13.2}$$

where q is the injected flow rate [m^3/s], A is the cross-sectional area of the core [m^2], k is the absolute permeability [m^2], μ is the viscosity of the fluid [Pa·s] and ΔP is the pressure drop [Pa] over length L [m]. To take into account the vertical orientation of the core in this experiment, with the inlet at the top, the impact of gravity is included, where ρ is the fluid density [kg/m^3], and g is the gravitational acceleration [81]. At 50 bar and 25°C, the viscosity (μ) of hydrogen is 8.94 x 10^{-6} Pa·s [57]. For the KI brine, μ was measured to be 9.22 x 10^{-4} Pa·s at 25°C. The pore-scale capillary number (Ca) can help characterize flow as it describes the balance of viscous forces over capillary forces:

$$Ca_i = \frac{v_i \mu_i}{\sigma}, \tag{13.3}$$

where i refers to the displacing phase (hydrogen or brine), v_i is the Darcy velocity of the displacing phase and μ_i is the viscosity of the displacing phase [Pa·s]. σ represents the interfacial tension between the fluids [N/m], which in this experiment is presumed to be equivalent to σ observed between hydrogen and pure deionized water under the experimental conditions (72.6 mN/m [15]). Pore-scale simulations have shown that Ca can have a substantial effect on UHS efficiency. Findings in Bagheri et al. [6] and Thaysen et al. [71] indicate that the ideal flow velocity, and consequently the capillary number, vary between hydrogen injection and production processes. By optimizing the capillary number, it is possible to reduce both viscous fingering [10] and capillary trapping effects, thereby enhancing both storage capacity and recovery efficiency. For this experiment, the flow rate is kept at constant at 0.5 ml/min during drainage and imbibition, resulting in a Ca of 1.31 x 10^{-8} for drainage and a 1.35 x 10^{-6} for imbibition, which both represent capillary controlled conditions [25]. The flow rate is chosen such that the capillary numbers are similar to previous studies (Table 12.2), facilitating meaningful comparisons.

13.3. Experimental apparatus

The experimental setup is based on the apparatus used by Boon and Hajibeygi [10] with the primary differences being the type of CT scanner and the use of a closed-loop system for both fluids. While Boon and Hajibeygi [10] used a medical CT scanner, this experiment utilizes a CoreTOM Micro CT produced by TESCAN. It is capable of capturing details in mm-size micro-plugs as well as imaging full cores measuring up to 1 meter in length [69]. Therefore, in this experiment, it is used to determine saturation profiles over the entire core (macro-scale), and to analyse flow behaviour and fluid redistribution at the pore-scale. Image acquisition data is summarized in Table 13.1.

Setting	Macro-scale scans	Pore-scale scans
Exposure time [s]	34	175
No. of projections	1440	2880
Set voltage [kV]	70.00	70.00
Actual power (range) [kW]	50.01 - 50.11	15.01 - 15.04
Rotation angle [◦]	360	360
Filter	1.5 mm Al	1.5 mm Al
Voxel size [µm]	175.0	6.5
Scanned length [mm]	1925	13

Table 13.1: CT acquisition data

To ensure the integrity of the experiment, a closed-loop system is used to minimize the risk of introducing non-equilibrated brine or hydrogen. Two pulse-free high-precision piston pumps, manufactured by Vindum Engineering, Inc. are used to inject the equilibrated brine and hydrogen. These pumps exhibit an accuracy of 0.1% [75] and are connected to a brine container and a hydrogen cylinder for the initial filling of the pump cylinders. 3 m long PEEK tubing (0.75 mm ID) serves as the conduit connecting the apparatus outside the CT scanner to the inlet pressure transducer (UNIK 5000), which is inside the CT scanner. 1.25 m Radel tubing (0.75 mm ID) connects the pressure transducer to the inlet of the core. The core is placed vertically inside the CT scanner and the fluids are injected at the top of the core. 0.78 m Radel tubing (0.75 mm ID) is used to connect the outlet at the bottom of the core to the second pressure transducer. 3 m PEEK tubing (0.75 mm ID) connects outlet pressure transducer to an additional Vindum pump positioned outside the CT scanner. This supplementary pump plays a crucial role in upholding a consistent back-pressure within the system. Positioned between the core outlet and the separation vessel, it acts as a buffer to reduce pressure fluctuations caused by the pump-filling process. The separation vessel has a volume of 150 ml and serves to segregate the brine and hydrogen, which subsequently replenish the pumps, facilitating the formation of a closed loop system. The system is brought to an operational pressure of 50 bar using a nitrogen cylinder and a back-pressure regulator. Upon completion of the experiment, an effluent bottle connected to the back-pressure regulator collects the brine. Subsequently, the effluent bottle is replaced with a tube connection leading to a fume hood for the safe disposal of hydrogen.

Safety measures are paramount throughout the experiment. A hydrogen monitor is installed within the CT scanner, and the hydrogen cylinder remains closed except during the filling of the hydrogen pump. The maximum system volume of hydrogen is 180 ml when the system is completely saturated. Throughout the remainder of the experiment, the volume of hydrogen gas remains below 100 ml. The experiment is conducted in a well ventilated area.

13.4. Experimental procedure

The procedure for the coreflood experiment is outlined below:

1. In the laboratory, the system undergoes a pressure test by saturating it with hydrogen up to 70 bar. Over time, a slight pressure drop occurs. To locate the leak, all valves undergo careful leak checks, and the core holder, along with the inlet and outlet tubing, is submerged in water. The appearance of tiny air bubbles sticking to the Radel tubing indicates the permeation of hydrogen through the material. At 50 bar, the pressure stabilizes upon injecting hydrogen at a rate of 0.013 ml/min, indicating the magnitude of the leak in the system at full hydrogen saturation. Due to this small leak, which poses no safety threat during the experiment in a well ventilated room, the

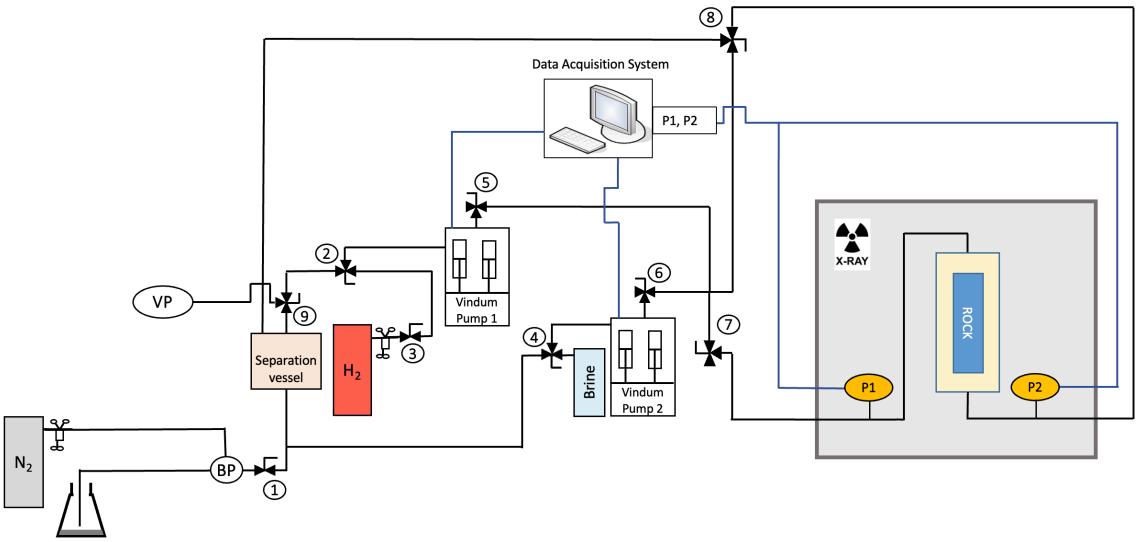

Figure 13.3: Schematic of the experimental setup.

hydrogen pump needs periodic replenishment to maintain a stable interface level between hydrogen and brine in the separation vessel throughout the experiment. This is monitored using the net volume which is injected by the back-pressure pump to maintain the 50 bar system pressure. Following the pressure test, the hydrogen is safely vented through the fume hood, and flushed with CO_2 while dried at 60°C for several hours to mitigate the risk of any liquid traces having migrated from the apparatus into the core.

2. In the CT room, the experimental apparatus outside the CT scanner is connected to the apparatus inside the CT scanner. Subsequently a scan is made of the dry core (air saturated) at macro-scale spec and pore-scale spec. The vacuum pump eliminates air from the system before introducing hydrogen.

3. Hydrogen is pumped through the system and valve 1 is cautiously opened until hydrogen bubbles are observed in the effluent water. The back-pressure is then increased to stop bubble formation. This process of observing bubble formation and increasing back-pressure is repeated until the back-pressure gradually reaches 50 bar. Once the flow is stopped, leak checks are conducted. Subsequently, the hydrogen-saturated core is scanned at both macro-scale and pore-scale spec. By gradually reducing the back-pressure to atmospheric, the hydrogen is vented to the fume hood, flushed with CO_2, and vacuumed while valve 1 remains closed.

4. The brine pump is filled from the brine container and pumped through the core while the outlet is still connected to the vacuum pump. Once the brine is visible at the outlet of the core, the core is bypassed to fill the separation vessel. When the brine is visible at the vacuum pump, the separation vessel is filled and 10 pore volume (PV) is pumped through the core again. Then, the vacuum pump is disconnected and the back-pressure is increased to 50 bar and the brine-saturated core is scanned at both macro-scale and pore-scale.

5. The absolute permeability of the core is determined by injecting brine for a range of flow rates between 0.5 and 2 ml/min. Using these flow rates together with the obtained pressure drops over the core, Darcy's law (Eq. 13.2) allows for the calculation of permeability.

6. While bypassing the core, 80 ml of hydrogen is injected to fill the upper half of the separation vessel, while 80 ml of brine is drained into the effluent bottle. Subsequently, the hydrogen cylinder and valve 1 are closed, and valves 2 and 4 are directed towards the separation vessel to enable re-circulation. Brine and hydrogen are co-injected through the pumps at a rate of 10 ml/min each for 20 minutes to pre-equilibrate the phases. The circulated volume (400 ml) exceeds twice the system volume of 180 ml. The pressure in the hydrogen pump experiences a slight drop due

to dissolution. Additional hydrogen is then injected into the pump from the hydrogen cylinder to restore the pressure to 50 bar.

7. The hydrogen pump is stopped and the hydrogen-saturated brine is recirculated over the core for 10 PV. Subsequently, a scan is made of the pre-equilibrated brine saturated core at macro-scale spec and pore-scale spec.

8. Once all background scans are completed, the brine-saturated core serves as the initial stage for the drainage relative permeability experiment. A consistent flow rate of 0.5 ml/min is maintained while incrementally increasing the fractional flow of hydrogen (f_{H2}). The inlet and outlet pressures are continuously monitored and recorded throughout the process. The attainment of steady-state is indicated by a constant pressure differential (ΔP). At each steady-state condition during the experiment, a macro-scale scan is conducted to determine the phase saturation. The last increment, when only hydrogen is injected into the core (f_{H2} = 1), marks the end of the drainage experiment, establishing the irreducible brine saturation (S_{wi}). This step also initiates the imbibition experiment, in which f_{H2} is incrementally reduced. The methodology mirrors that of the drainage experiment and the end-point (f_{H2} = 0), yield the residual gas saturation S_{gr}. The saturations and pressure differentials observed at each steady-state condition are utilized to derive the drainage and imbibition relative permeability curves.

9. To observe flow paths at the pore-scale and to analyse Ostwald ripening over time, a pore-scale spec image is captured during the drainage experiment, at f_{H2} = 0.1. The flow was paused for 39 hours, and another pore-scale spec image was acquired before resuming the drainage experiment. Additionally, a pore-scale spec image was obtained at the conclusion of the imbibition experiment and repeated after both 17 hours and 92 hours without flow.

13.5. Relative permeability

For this experiment, the steady-state method is employed, where both wetting and non-wetting fluids are injected simultaneously into the core at varying fractional flows. Once steady-state is achieved, water saturation and the pressure differential between the core inlet and outlet are measured for each fractional flow. Darcy's law, extended for a multiphase system, is then used to calculate the steady-state relative permeability of brine and hydrogen:

$$q_i = \frac{Akk_{r,i}(S_i)}{\mu_i}\left(\frac{\Delta P}{L} + \rho_i g\right), \tag{13.4}$$

where i refers to the phase (hydrogen or brine), $k_{r,i}(S_i)$ is the relative permeability of phase i as a function of saturation [-]. Note that there is a pressure drop over the inlet and outlet tubing between the pressure transducers and the core (Figure 13.3). However, during the drainage and imbibition experiment, the influence of the tubing on ΔP is less than 0.02 bar following the Hagen-Pousseuille equation. This is negligible to the measured ΔP during the experiment. Therefore, it is not included in the relative permeability calculations.

The saturation of the hydrogen inside the core (S_{H_2}) is determined according to the following equation [10]:

$$S_{H_2} = \frac{CT_{exp} - CT_w}{CT_{H_2} - CT_w}. \tag{13.5}$$

CT_{exp} represents the voxel level CT number [HU] obtained from the core at a specific step in the experiment. Similarly, CT_{H_2} and CT_w are the voxel level CT numbers for the hydrogen saturated core and the brine saturated core (background scans), respectively. Relative permeability curves are usually plotted as a function of the wetting phase saturation, S_w. The average S_w values over the whole core are used. S_w can be determined using:

$$S_w = \frac{CT_{exp} - CT_{H_2}}{CT_w - CT_{H_2}}, \tag{13.6}$$

or similarly:

$$S_w = 1 - S_{H_2}. \tag{13.7}$$

The drainage relative permeability curves can be fitted to empirical functions for both the brine (Eq. 13.8) and hydrogen (Eq. 13.9). Upscaled transport functions can be benchmarked using these functions [28]. In this study, the results are fitted using the modified Brooks-Corey equations [31]:

$$k_{r,w} = k_{r,w,max}\left[\frac{S_w - S_{wi}}{1 - S_{gr} - S_{wi}}\right]^m, \tag{13.8}$$

$$k_{r,g} = k_{r,g,max}\left[\frac{(1 - S_w) - S_{gr}}{1 - S_{gr} - S_{wi}}\right]^n, \tag{13.9}$$

where $k_{r,g,max}$ is the end-point relative permeability for each phase, S_{wi} is the irreducible brine saturation, S_{gr} is the residual gas saturation, m is the water/brine relative permeability exponent and n is the gas relative permeability exponent. The exponents are associated with pore structure and wettability [28]. At the end of imbibition, when 100% brine is injected, the residual gas saturation (S_{gr}) can be obtained. This represents the amount of trapped hydrogen. The amount of trapped hydrogen is given using the linear trapping coefficient A [56]:

$$A = \frac{S_{gr}}{S_{gi}}, \tag{13.10}$$

where S_{gi} is the initial gas saturation, obtained at the end of drainage.

13.6. Ostwald ripening

High-resolution CT imaging is used to analyze Ostwald ripening at the pore scale. To limit scanning duration, a 1 cm section in the middle of the core is scanned. The relative permeability experiment is conducted simultaneously, with the flow stopped at certain points to perform high-resolution scans. Scans are taken at the start and at the end of intervals without flow, mimicking periods during which the hydrogen is ”stored” in the rock. Before the start of the experiment, the dry core is scanned at high resolution to allow creating a mask of the pore space, which is used for processing the multiphase scans. To quantify the effect of Ostwald ripening, hydrogen ganglia size distributions are extracted using the image processing software Avizo 3D 2023 (Thermo Fisher). The processing steps can be summarized as follows: First, noise is removed using a median filter. The scans are then registered and resampled to ensure precise alignment between the image stacks. Using the dry pore space as a mask, the fluids are separated from the grains. The fluids are subsequently segmented to distinguish between brine and hydrogen. Finally, the individual hydrogen ganglia are labeled and analyzed. To estimate the progression of Ostwald ripening, the timescale for pore-scale equilibrium in laboratory experiments are estimated using Eq. 11.2 [8]. A detailed guideline for the pore-scale image processing steps can be found in Appendix A.

14

Results and Discussions

14.1. Flow characteristics and relative permeability

12 data points were acquired for the relative permeability curves: 7 data points for drainage and 5 for imbibition. Table 14.1 lists the flow conditions for these data points, including the constant total flow rate (q), the varying fractional flows (f_i), and the resulting flow rates for each phase (q_i). Note that the final step in the drainage experiment marks the start of the imbibition experiment.

Drainage step	q **[ml/min]**	f_{H2}	f_w	q_{H2} **[ml/min]**	q_w **[ml/min]**
1	0.5	0.1	0.9	0.05	0.45
2	0.5	0.3	0.7	0.15	0.35
3	0.5	0.5	0.5	0.25	0.25
4	0.5	0.7	0.3	0.35	0.15
5	0.5	0.9	0.1	0.45	0.05
6	0.5	0.97	0.03	0.485	0.015
7	0.5	1	0	0.5	0
Imbibition step					
8	0.5	0.9	0.1	0.45	0.05
9	0.5	0.5	0.5	0.25	0.25
10	0.5	0.1	0.9	0.05	0.45
11	0.5	0.03	0.97	0.015	0.485
12	0.5	0	1	0	0.5

Table 14.1: Flow conditions for the drainage and imbibition experiments.

After processing the macro-scale scans at steady-state, it is observed that, especially for the steps with lower f_{H2}, the first 2 cm from the inlet exhibits a higher S_w compared to the bulk of the core. This is likely due to dissolution of hydrogen. Despite extensive recirculation outside the core to pre-equilibrate the phases before the start of drainage, dissolution still appears to occur. This may be due to a pressure difference between the pre-equilibration at 50 bar and the inlet pressure during drainage. The pressure drop across the core results in a higher pressure at the inlet that gradually decreases along the length of the core. According to Henry's law, the higher partial pressure of hydrogen at the inlet leads to increased dissolution. As the dissolved hydrogen moves further down the core, the partial gas pressure decreases, causing hydrogen to come out of solution and form possibly disconnected ganglia. This process results in lower S_w values down the core. Additionally, these disconnected ganglia might obstruct flow, leading to relatively large pressure drops, as can be seen in Table 12.3. The gradual increase in pressure drop might explain the unexpectedly slow progression to steady-state. In the first step of the drainage experiment, steady-state was achieved after injecting 13 PV. The high S_w values at the inlet furthermore indicate that buoyancy does not overcome viscous forces, which would lead to

a build-up of hydrogen at the top of the core. This is in contrast with the clear gravity segregation seen during drainage in the experiment by Boon and Hajibeygi [10], where there was horizontal flow. The 3D saturation maps in Figure 14.2 clearly show higher brine saturations near the inlet. In the bulk of the core, away from the inlet, no flow segregation is detected, indicating that both phases are flowing through the same pore space and suggesting that the extracted flow parameters are representative of a multiphase system. However, in the final stages of imbibition, preferential flow paths for the brine become apparent at the inlet away from the core's center. This may result from hydrogen buildup in the center of the endcap (Appendix B). Therefore, optimizing the internal shape of the endcap may prevent this issue. At the outlet of the core, capillary end effects due to the increase in capillary pressure discontinuity could be expected especially for high gas fractional flows [81] [31]. This would result in larger S_w values. However, because the saturation profile remains constant near the end of the core, it can be confirmed that there are no capillary end effects.

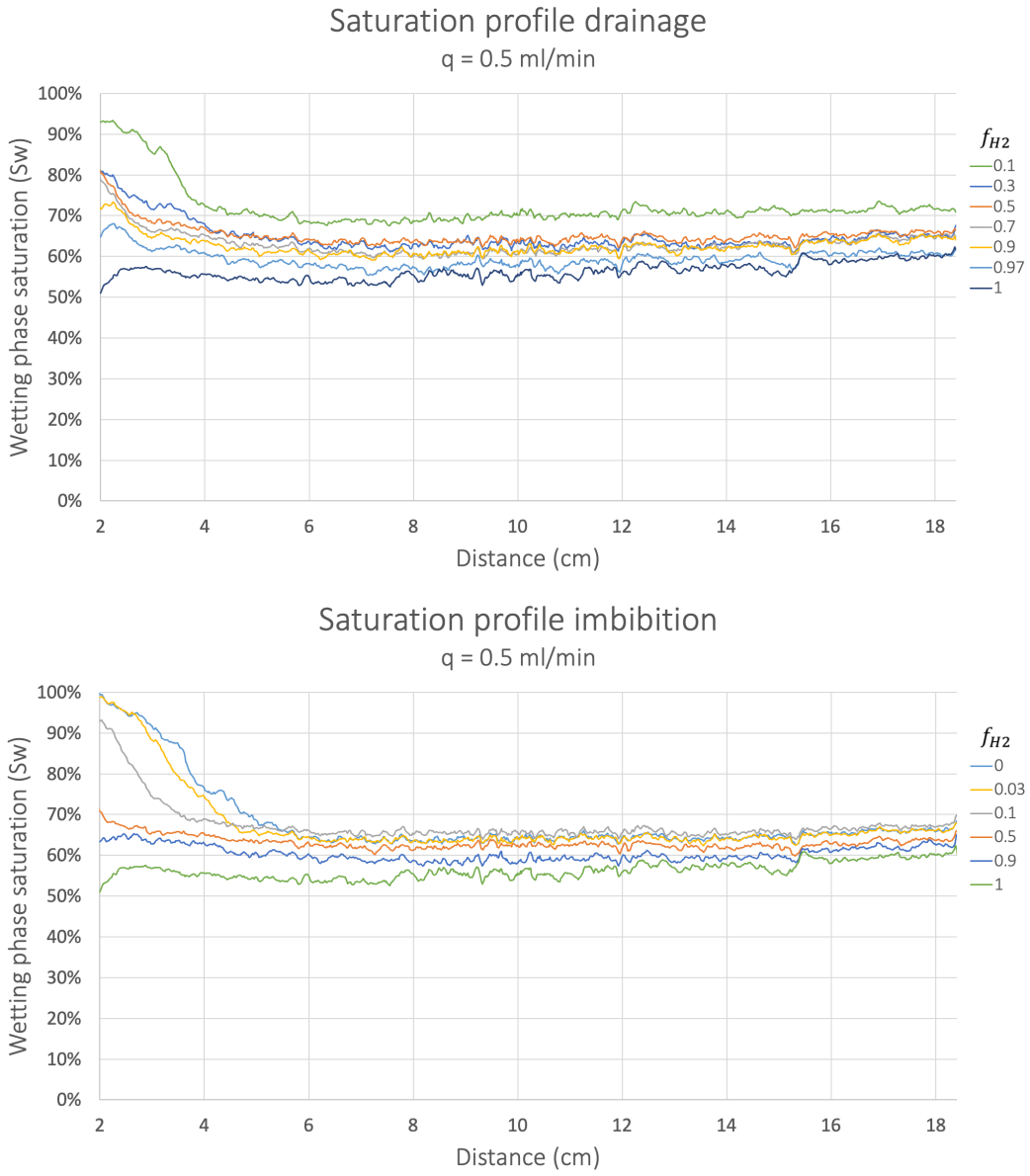

Figure 14.1: Steady-state drainage/imbibition saturation profiles. The x-axis limits are set to include only the length of the core, excluding the endcaps. Please note that at the end of imbibition (f_{H_2} = 0), the valve of the hydrogen pump was not closed. Consequently, due to gas expansion, some hydrogen may have still entered the core, although the pump was inactive at that time.

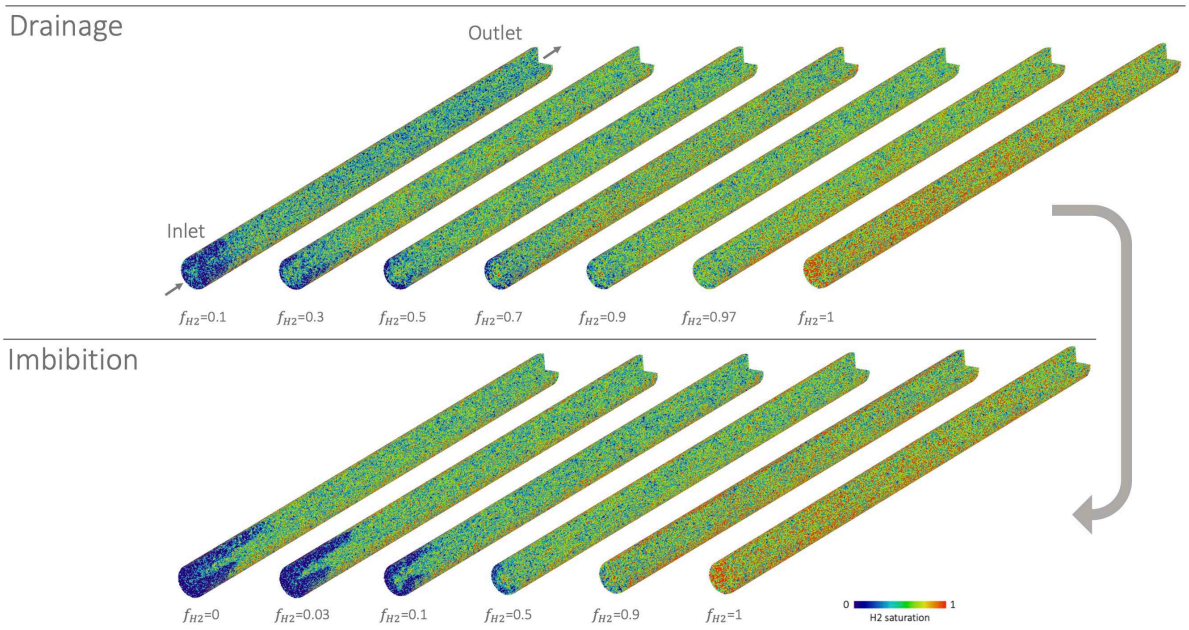

Figure 14.2: Steady-state 3D saturation maps for drainage and imbibition. Note that the core was vertically placed during the experiment with the inlet at the top.

The average saturation at the end of drainage represents the minimum brine saturation in this experiment at S_w = 0.56, which also corresponds to the initial gas saturation (S_{gi} = 0.44). It is important to note that this saturation does not represent the actual irreducible brine saturation S_{wi} as flow rates were not adjusted to maximize brine removal from the core. At the end of imbibition, the residual gas saturation (S_{gr} = 0.32) represents trapped hydrogen. From this, the linear trapping coefficient is determined to be 0.725, indicating that 72.5% of the hydrogen gets trapped. This substantial fraction of 'lost' hydrogen could be reduced by adjusting flow rates. Specifically, a lower capillary number during drainage may result in a higher S_{gi}, while a higher capillary number during imbibition may lead to a smaller S_{gr}, as demonstrated experimentally by Thaysen et al. [71]. However, the impact of Ca on S_{gi} and S_{gr} depends on the magnitude of Ca which determines whether the flow is dominated by capillary or viscous forces [71]. Contrarily to the observation by Thaysen et al. [71], Boon and Hajibeygi [10] increased S_{gi} by increasing the flow rate (or Ca_{H_2}) by a factor 6 at the end of drainage, thereby increasing S_{gi} from 0.36 to 0.47. Evidently, optimizing capillary numbers during drainage and imbibition could significantly decrease the linear trapping coefficient.

In context of commercial scale UHS, the large amount of trapping suggests that at the first cycle, when hydrogen is injected into a brine-bearing depleted reservoir or aquifer, a significant portion of the injected hydrogen will not be recovered during production. Instead, the immobile hydrogen will act as a cushion gas setting the lower end of the working pressure range. On an experimental scale, the difference between S_{gi} of 0.44 and S_{gr} of 0.32 indicates that only 12% of the effective pore volume can be considered "working volume". During subsequent injection and withdrawal cycles, this working volume is expected to remain largely unchanged. The mobile hydrogen recovered during the first cycle will be roughly equal to the working volume that can be injected and produced in subsequent cycles. This hypothesis is supported by experimental results of Thaysen et al. [71], who found similar S_{gi} and S_{gr} values between the first drainage/imbibition cycle (0.479 and 0.070) and the second cycle (0.476 and 0.073) under the same conditions.

Figure 14.3 presents the relative permeability curves for drainage and imbibition following the data points in Table 14.2. The height of the crossover point between the brine and hydrogen curves indicates the degree of interference between these two phases, leading to smaller relative permeabilities. Consistent with the findings of Yekta et al. [81], Boon and Hajibeygi [10], Lysyy et al. [52], and Higgs et al. [31], this crossover point lies at a value between 0.01 and 0.1. However, in contrast to Higgs et al. [31], the crossover point in our data is shifted further to the right, suggesting a stronger water-wet system. This observation aligns more closely with Boon and Hajibeygi [10], likely due to the use of the same rock type (Berea). Additionally, our study reveals similar slopes for the wetting phase (brine)

relative permeability during both drainage and imbibition, indicating minimal hysteresis. Nevertheless, some hysteresis is observed in the hydrogen relative permeability. The hydrogen endpoint relative permeability found in this experiment, which is a crucial factor in evaluating injectivity in reservoir rock, is 0.043. This value is consistent with the values found in the aforementioned studies. Only Rezaei et al. [64] found a much larger end-point relative permeability. However, this experiment was conducted without imaging. As a result, the presence of preferential flow paths that do not represent true multiphase flow cannot be ruled out.

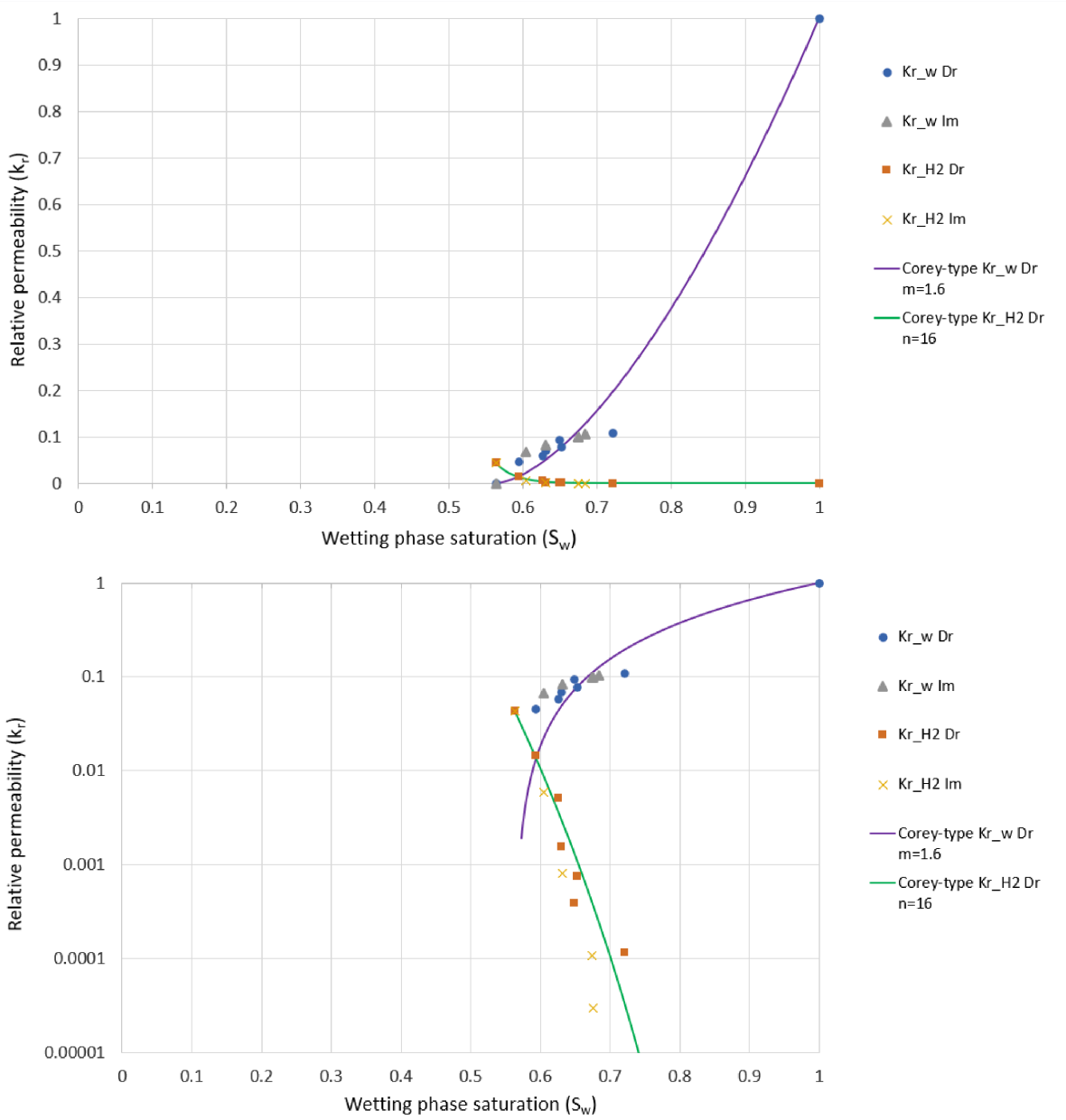

Figure 14.3: Steady-state drainage/imbibition relative permeability curves plotted in normal and semilogarithmic scale, compared with the modified Brooks-Corey model for drainage. Please note that the curves are fitted using the minimum S_w as S_{wi}. The actual S_{wi} was not determined in this experiment.

Drainage step	f_{H2}	dP [bar]	dP [Pa]	S_w	$k_{r,H2}$	$k_{r,w}$	PV injected
1	0.1	13.36	1.34E+06	0.72	1.17E-04	1.08E-01	13
2	0.3	12.07	1.21E+06	0.65	3.87E-04	9.30E-02	11
3	0.5	10.35	1.04E+06	0.65	7.52E-04	7.74E-02	5
4	0.7	7.04	7.04E+05	0.63	1.55E-03	6.83E-02	4
5	0.9	2.76	2.76E+05	0.63	5.08E-03	5.78E-02	4
6	0.97	1.04	1.04E+05	0.59	1.45E-02	4.56E-02	4
7	1	0.36	3.60E+04	0.56	4.32E-02	0	4
Imbibition step							
8	0.9	2.39	2.39E+05	0.60	5.86E-03	6.77E-02	9
9	0.5	9.73	9.73E+05	0.63	8.00E-04	8.26E-02	6
10	0.1	14.54	1.45E+06	0.67	1.07E-04	9.95E-02	4
11	0.03	15.88	1.59E+06	0.68	2.94E-05	9.82E-02	4
12	0	15.35	1.54E+06	0.68	0	1.05E-01	3

Table 14.2: Hydrogen fractional flow, pressure drops, brine saturation, relative permeability values, and the number of pore volumes injected until steady state for each step in the experiment.

14.2. Dissolution

After completing the imbibition experiment, the core containing trapped hydrogen (S_{gr}) was left undisturbed over the weekend. After 92 hours, the saturation profile was measured again. While there was some rearrangement of the hydrogen and possibly some diffusion towards the outlet, the average saturation remained similar. Subsequently, the core was flooded with 30 PV of brine that was not pre-equilibrated with hydrogen. This led to a gradual decrease in the pressure drop and an increase in S_w to 0.93 at steady state, indicating the dissolution of the majority of the trapped hydrogen. The changing saturation profiles can be found in Figure 14.4.

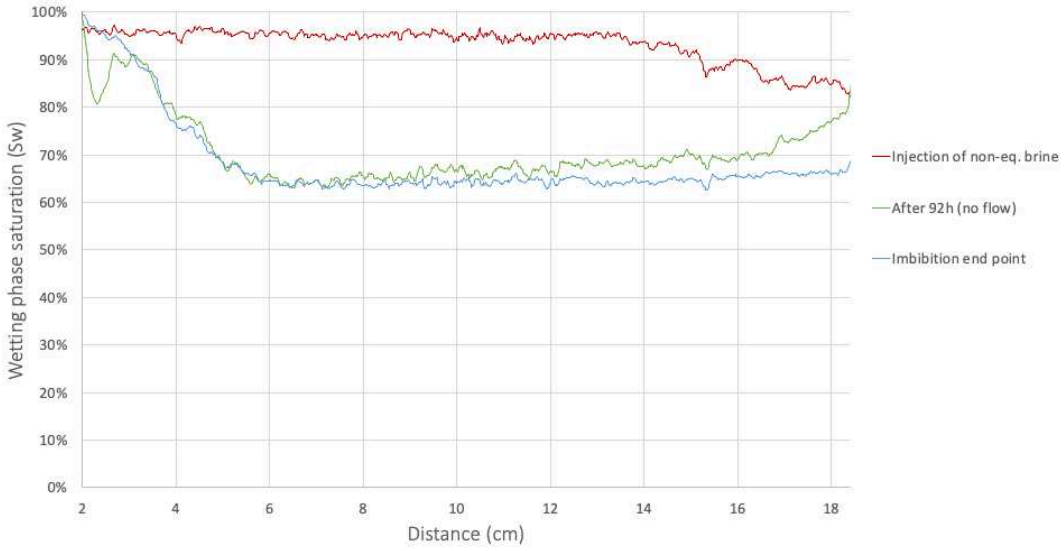

Figure 14.4: Saturation profile showing almost complete dissolution of hydrogen after injection of non-equilibrated brine.

Chabab et al. [14] measured the solubility of hydrogen in water and NaCl brine at various concentrations and used the obtained values to optimize models. These models were then used to calculate solubilities across a range of pressures and temperatures. For hydrogen in pure water at the experimental conditions (50 bar and 25°C), they calculated a solubility of 6.85 x 10^{-4} (salt-free mole fraction). This corresponds to just 0.077 g/kg$_w$. Still, given hydrogen's low density, injecting 30 PV of non-equilibrated pure water could potentially dissolve up to 0.59 PV of hydrogen. After injecting 30 PV brine in this experiment, S_{H2} decreased from 0.29 to 0.07, indicating that 0.22 PV of hydrogen was dissolved. It is

important to note that hydrogen has lower solubility in KI brine than in pure water due to the salting-out effect [35] [14]. One of the findings by Hulikal et al. [35] is that increasing molality of NaCl in water by 1 mol/kg$_w$, will result in a decrease of around 15% in hydrogen solubility, regardless of the pressure and temperature. Although different salts exhibit varying salting-out effects, the KI brine molality of just 0.18 mol/kg$_w$ in this experiment is not likely to have a significant impact on the observed dissolution rate. The difference between the potential 0.59 PV, and the actual 0.22 PV of dissolved hydrogen is more likely due to the brine being partially saturated with hydrogen from the start of the injection. Ostwald ripening during the 92-hour period might have reconnected some trapped hydrogen that now became mobile, but the effect is not expected to be significant.

14.3. Ostwald ripening

Figure 14.5 visualises the intermediate processing steps for the scan immediately after pausing the flow during drainage at f_{H2} = 0.1. The same steps are applied for every pore-scale scan. The procedure is as follows: first, the raw image is cropped to separate the core from the core holder. Then it is filtered using a median filter. To ensure proper analysis, all scans must be precisely aligned. This is achieved by registering and resampling the image stacks based on corresponding greyscale values of the grains and minerals, using the dry background scan as a reference. Next, the pore space is extracted using a mask of the dry scan, and the greyscale values within the pore space are thresholded to segment the hydrogen and the brine. Finally, the disconnected hydrogen ganglia are labeled, and parameters are extracted. This allows for the determination of the volumes of discrete ganglia. The volume distributions of these ganglia serve as a measure of Ostwald ripening. In order to maintain reliability in the measurements, all ganglia with a size less than 10 voxels [25] are excluded from the ganglia volume distributions as they may be attributed to noise.

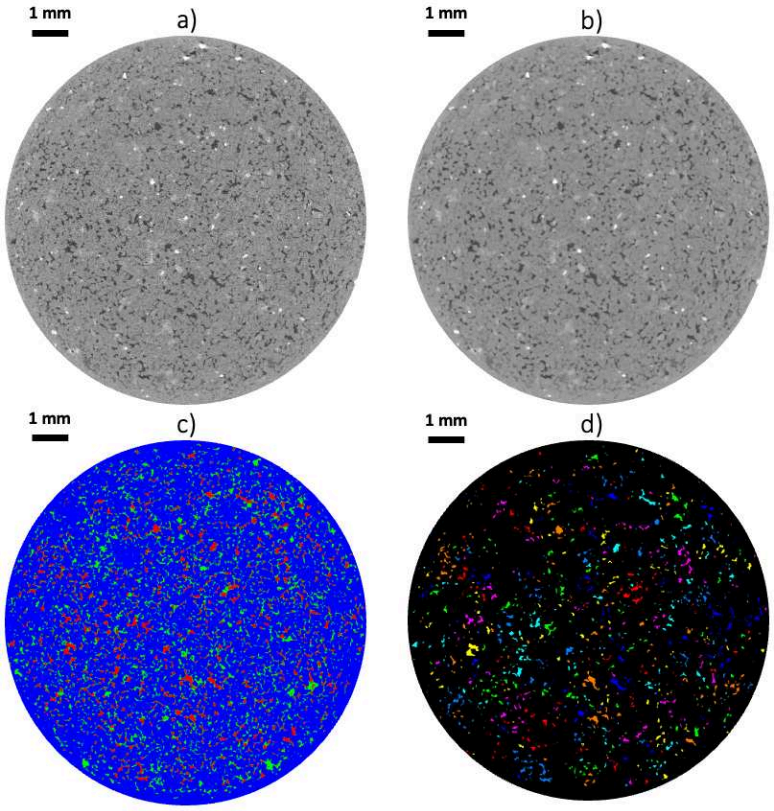

Figure 14.5: A 2D representation of the image processing procedure. a) shows the cropped raw image with hydrogen (dark grey), brine (medium grey), grains (light grey) and high density minerals (white). b) shows the filtered and resampled image. c) shows the masked and segmented image with hydrogen (red), brine (green) and grains and minerals (blue). d) shows the labeled distinct hydrogen ganglia where a difference in color represents non-connected ganglia.

Additionally, pore-scale visualization of shrinkage and growth of ganglia after storage offers further evidence. It must be noted that the connectivity of ganglia may not be detected if the connections are smaller than the scanning resolution. This could explain the apparent numerous discrete ganglia visible in Figure 14.6. This is contrarily to the results by Goodarzi et al. [25] where a single large ganglion dominates the total hydrogen volume, also before storage. Their study uses a slightly higher scanning resolution. Table 14.3 lists storage times and saturations for the pore-scale scans. Note that saturations may change slightly due to influx or outflux of hydrogen from adjacent sections in the core.

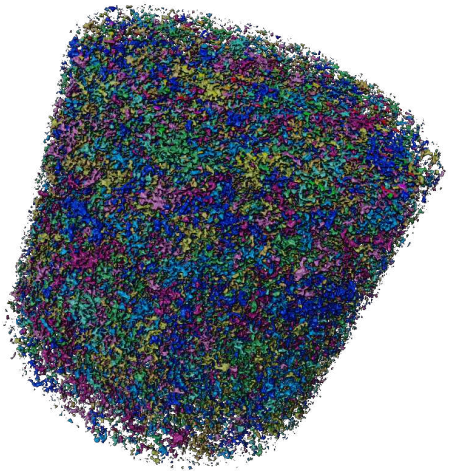

Figure 14.6: 3D image showing hydrogen ganglia after pausing the flow during drainage at f_{H_2} = 0.1. A difference in color represents non-connected ganglia. Note that the colormap consists of only 8 colors, so distant ganglia with the same color often do not represent connected ganglia.

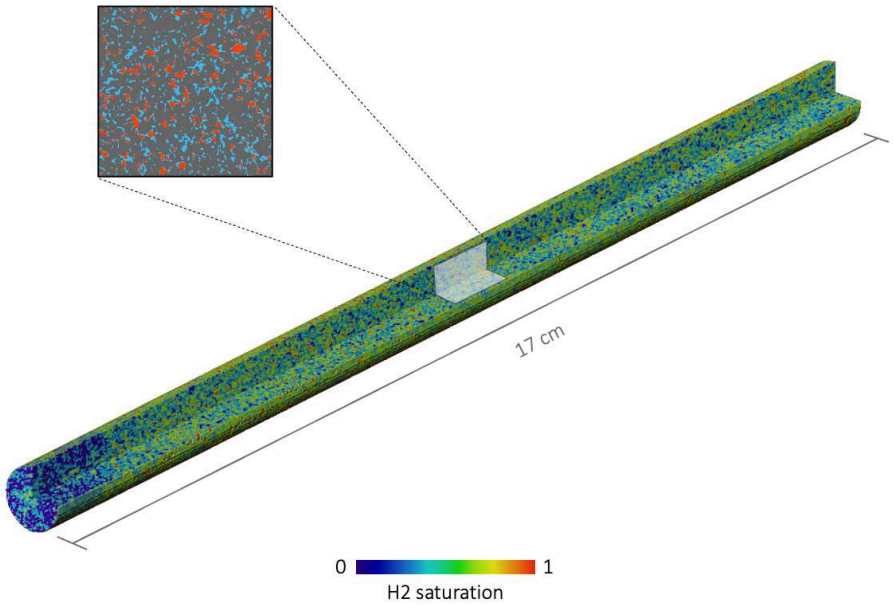

Figure 14.7: Steady-state saturation map for drainage at f_{H_2} = 0.1. The highlighted area indicates the location of the 1 cm section that was imaged at pore-scale to investigate Ostwald ripening.

Scan	Storage time	S_w
1	-	0.69
2	39h	0.66
3	-	0.61
4	17h	0.64
5	92h	0.65

Table 14.3: Storage time and saturations for the scans taken after pausing the flow during drainage at f_{H2}= 0.1 (scan 1-2), and after the end of imbibition at f_{H2}= 0 (scan 3-5).

From Figure 14.8, it can be observed that the quantities of both the smallest and the largest ganglia increase at the expense of the mid-sized ganglia. Two new large ganglia form, as shown in the subplot, which significantly contribute to the total volume, as indicated in the relative distribution. Additionally, the relative distribution reveals a rightward shift in the mode, indicative of Ostwald ripening [84]. The increase in the number of small ganglia and the formation of new large ganglia are likely due to mid-sized ganglia breaking apart into several smaller ganglia. This fragmentation occurs due to volume loss from dissolution and diffusion toward low P_c regions, leading to the formation of larger ganglia. Small ganglia do not always completely disappear as P_c may drop when the small ganglia migrate into larger pore spaces [8], which may be allowed by this fragmentation. Furthermore, it is possible that the process of Ostwald ripening has not yet fully developed after the 39 hours. It is likely that only the highest capillary pressure regions underwent Ostwald ripening. This hypothesis can be substantiated by estimating the time scale to reach local equilibrium using Eq. 11.2, which is 265 hours, or 11 days. The calculation assumes a length (l) of 1 mm [8], a throat radius (r) of 10 x 10^{-6} m [76], a gas saturation (S_{gr}) of 0.28, which is the hydrogen saturation when the flow is stopped, a diffusion coefficient (D) of 9.35 x 10^{-10} m^2/s (which is the value for hydrogen in water at 25°C [21] corrected by the porosity) and Henry's constant (H) is 7.8 x 10^{-6} mol/m^3·Pa [66]. However, this time scale can be considered an overestimate because the equation estimates an equilibrium state in which all trapped gas is displaced, whereas in reality only a fraction needs to relocate to achieve equilibrium [8]. Additionally, S_{gr} represents trapped, disconnected hydrogen, whereas during drainage, less hydrogen will be trapped. However, as described in Section 14.1, a significant portion of the hydrogen in the middle of the core might be disconnected (trapped) due to dissolution at the inlet and the formation of ganglia further down the core.

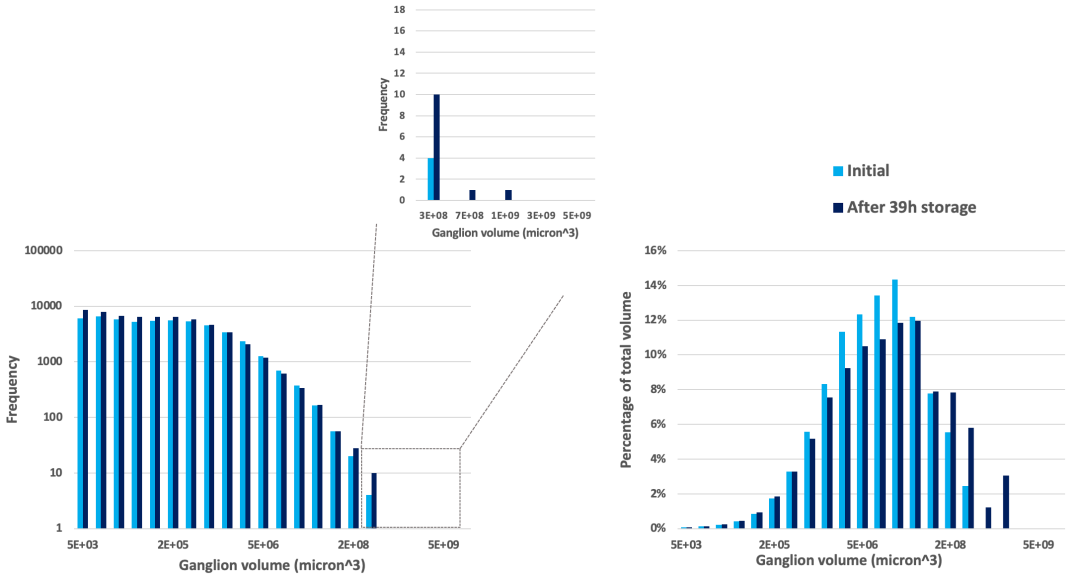

Figure 14.8: Hydrogen ganglion volume distribution immediately after pausing the flow during drainage at f_{H2} = 0.1, and after 39h of storage. The left plot shows the frequency distribution of ganglia sizes. The right plot displays the total volume of the ganglia in each bin relative to the total volume of all hydrogen ganglia.

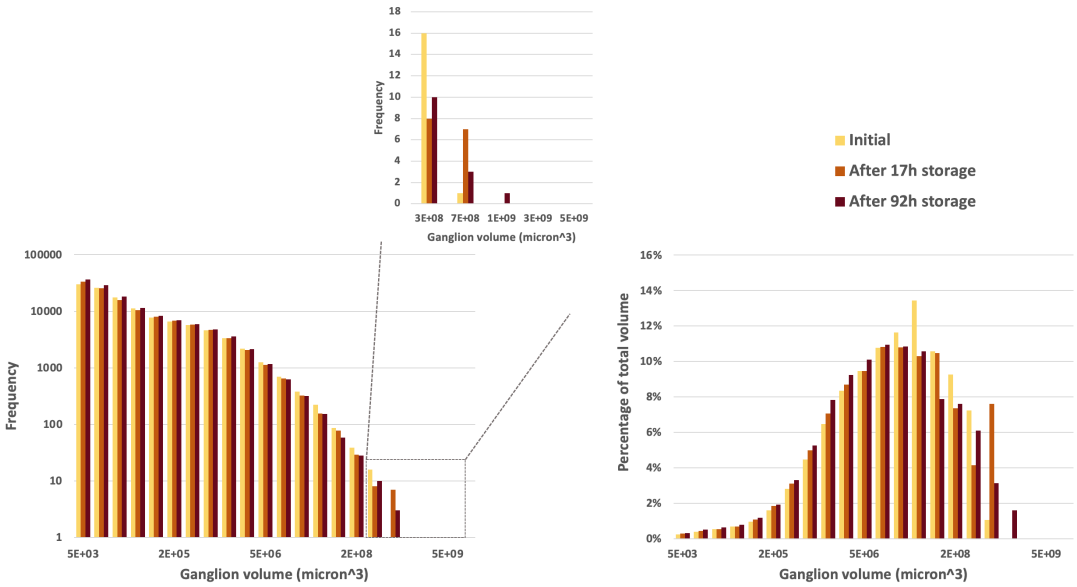

Figure 14.9: Hydrogen ganglion volume distribution immediately after the end of imbibition at f_{H2} = 0, after 17h of storage and after 92h of storage. The left plot shows the frequency distribution of ganglia sizes. The right plot displays the total volume of the ganglia in each bin relative to the total volume of all hydrogen ganglia.

Figure 14.9 shows the changing ganglion volume distribution functions after storage following the end of imbibition. The subplot highlights the formation of new, larger ganglia over time. Additionally, there is a noticeable decrease in the quantity of the larger half of the mid-sized ganglia, accompanied by an increase in the number of small ganglia, possibly due to fragmentation similar to the process during drainage. However, it is important to note that the results of the post-imbibition pore-scale experiment are more prone to error. The pore-scale scans taken while the drainage experiment was paused are of high quality, providing consistent CT values. This consistency allows for reliable thresholding to segment the fluids accurately, enabling precise comparisons between different scans. Conversely, the post-imbibition pore-scale scans after 17 hours and 92 hours of storage appear to be of relatively poor quality for unknown reasons. Although image processing remains possible, the inconsistent CT values prevent the use of equal threshold values for the different scans. Threshold values were initially determined through visual inspection. To minimize potential errors due to the lower scan quality, the threshold values were then adjusted using trial and error such that the resulting saturation closely matched the saturation obtained from the most recent macro-scale measurements. However, since the pore-scale scan covers only a 1 cm section of the core (Figure 14.7), potential influx or outflux over time from adjacent core sections makes this validation method less reliable.

14.3.1. Pore scale visualisation

To visualise the concept of growth of large ganglia at the expense of fragmented mid-size ganglia, the ganglia are sieved into small, mid-size, and large ganglia and are given a different color. The ranges are based on the volume frequency distributions, where the small and large ganglia increase in frequency and the mid-size ganglia decrease in frequency. This division is as follows:

Ganglia size	Range (μm^3)	Color
Small	$< 6.6 \times 10^5$	Blue
Mid	6.6×10^5 - 2.1×10^7	Yellow
Large	$> 2.1 \times 10^7$	Red

Table 14.4: Sieved ganglia sizes for visualisation.

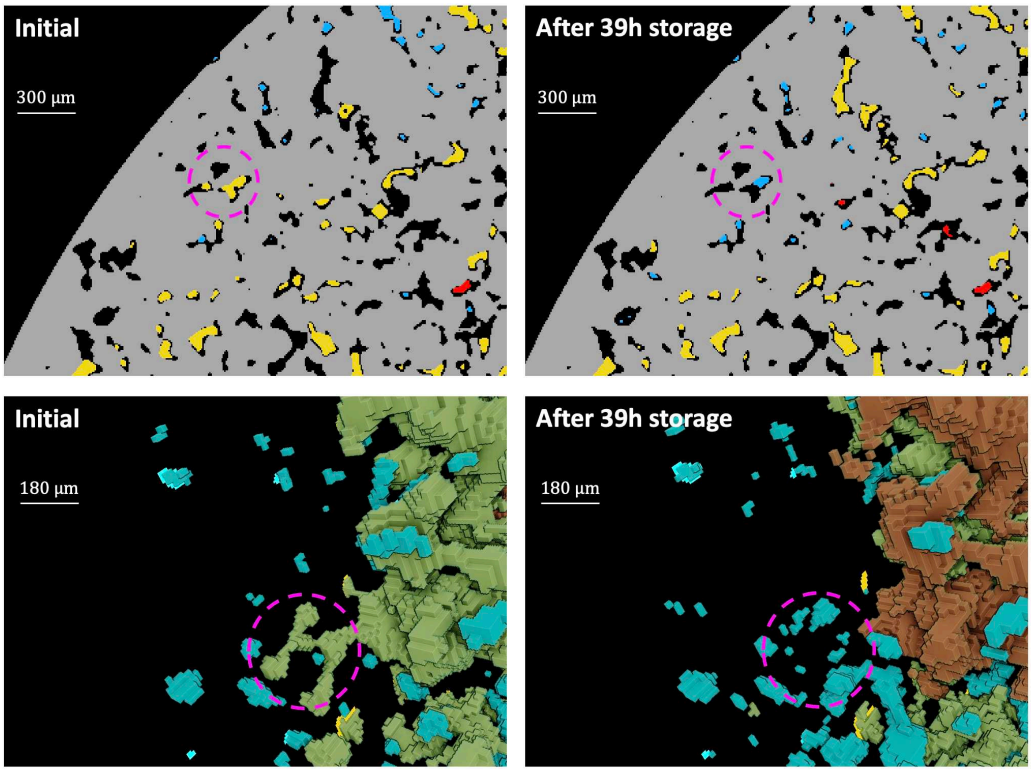

Figure 14.10: 2D slice and 3D volume of hydrogen ganglia before and after storage. The 2D images illustrate the rock (grey) with a mid-sized ganglion (yellow) highlighted within the pink circle, which transforms into a smaller ganglion (blue) after storage. In the 3D figures, it is evident that the same mid-sized ganglion fragments into multiple smaller ganglia. Additionally, a large ganglion (red) forms after storage, visible on the right side of the 3D image.

15

Conclusions and Recommendations

This study presents experimental measurements of steady-state relative permeability using co-injection of brine and hydrogen in a vertical Berea sandstone core during both drainage and imbibition processes. A 17 cm core with a diameter of 10.5 mm was used, and the experiments were conducted at 25°C and 50 bar. Saturation distributions were determined using CT imaging. An end-point relative permeability of 0.043 was found, which is consistent with values reported in previous studies [81] [10] [52] [31]. Flow experiments with capillary numbers of 1.3×10^{-8} (drainage) and 1.3×10^{-6} (imbibition) resulted in a linear trapping coefficient of 0.725, suggesting that only 12% of the effective pore volume can be considered working volume. Additionally, the results of this experiment highlight the complex and undesirable effects of dissolution. Despite extensive pre-equilibration before the start of the experiment, significant dissolution still occurred at the elevated inlet pressure when hydrogen was injected at the beginning of drainage. Furthermore, at a later stage of the experiment, it was demonstrated that the injection of brine poorly equilibrated with hydrogen dissolved almost all the trapped hydrogen.

Apart from the dissolution at the inlet during the start of drainage, the saturation distributions indicate a uniform flow of both phases throughout the bulk of the core. However, towards the conclusion of imbibition, there is evidence of radial flow segregation at the inlet, likely attributable to the geometry of the inlet endcap.

During the experiment, a 1 cm section in the middle of the core was imaged at high resolution to observe the rearrangement of gas in the pore space without flow, due to local dissolution and diffusion, known as Ostwald ripening. The results show that Ostwald ripening leads to the fragmentation of mid-size hydrogen ganglia and the growth of a few larger ganglia. On a 1 mm length scale, total equilibrium is expected to be reached within 11 days. Therefore, the ganglion volume distributions and the 3D visualisations in this study may indicate a state of partial equilibrium, where only the hydrogen in the highest capillary pressure regions has dissolved due Ostwald ripening.

The experimentally obtained relative permeability values help validate findings from previous experiments. This may lead to a reduction in the considerable uncertainty currently associated with UHS as large scale reservoir simulators can use these relative permeability values as input parameters. Moreover, the observed dissolution effect underscores the importance of considering it when predicting hydrogen recovery rates, emphasizing the need for a thorough analysis of the dissolution capability of in-situ fluids. To further improve modeling capabilities, the effect of Ostwald ripening needs to be considered, as it can influence trapped hydrogen saturations, capillary pressure, and relative permeability [2]. Conventional models based on hydrocarbon production usually ignore Ostwald ripening [84]. Consequently, when applied to hydrogen storage, these models tend to overestimate the amount of trapping and relative permeability hysteresis, thereby underestimating the feasibility of UHS.

To experimentally study the effect of Ostwald ripening on relative permeability hysteresis, future research should compare relative permeability core flooding experiments with and without storage time between primary and secondary drainage/imbibition cycles. Conducting multiple cycles will also enhance our understanding of potential cyclic effects associated with UHS. Moreover, multiple pressure measurement points could be installed to determine whether flow segregation at the inlet affects the pressure profile across the core, thereby impacting the relative permeability curves. Future experiments could use more permeable rock to minimize pressure differentials across the core and assess whether

this reduces the dissolution rate at the inlet. For pore-scale analysis, mapping capillary pressure regions in 3D could reveal their correlation with Ostwald ripening, potentially achieved through interfacial curvature analysis of CT scans. Similar to the approach by Goodarzi et al. [25], calculating the Euler characteristic could be employed to assess connectivity before and after Ostwald ripening. If feasible, achieving higher imaging resolutions would better capture the connectivity of hydrogen ganglia after image processing. Finally, investigating longer storage times with intermediate image analyses could provide insights into the progression towards different states of equilibrium.

III

Interrelated Implications

16

Interrelated Implications

Although both parts of this thesis address different aspects of UHS in porous media, with the techno-economic study focusing on surface facilities and costs, and the experimental work concentrating on fluid behavior in rock at a micro-scale, heir results are mutually informative. Firstly, it was demonstrated that hydrogen exhibits complex flow behavior in the presence of brine. Relative permeability, capillary trapping, dissolution, and Ostwald ripening are all factors relevant in a multiphase system. Therefore, evaluating the fluid composition of a target depleted gas reservoir is crucial for predicting the impact of these phenomena on the techno-economic feasibility. For instance, the experimental work demonstrated a trapping coefficient of 0.725 under the experimental conditions. In the techno-economic case study, the selected depleted gas reservoir was designed to hold 2.30 BCM of hydrogen cushion gas and 1.54 BCM of working volume. If 72.5% of this total hydrogen volume were immobilized due to capillary trapping, achieving a working volume of 1.54 BCM would not be feasible, potentially altering the business case. However, this scenario is oversimplified because capillary trapping is highly site-specific, dependent on factors such as rock type and reservoir conditions. Therefore, it underscores how assumptions in techno-economic studies can be refined by conducting experimental work that mimics the conditions of the target reservoir. Moreover, the direction of phase displacement can significantly impact well placement strategies. In this experiment, drainage and imbibition occur in the same direction, mimicking distinct injection and production using separate wells. However, if wells are used for both injection and production, drainage and imbibition would proceed in opposite directions, potentially leading to different hysteretic effects. Utilizing wells for both purposes could yield substantial cost savings. Therefore, future experimental setups could be designed to allow drainage and imbibition to occur in opposite directions. In a more comprehensive experiment, geochemical and microbial reactions could be evaluated using rock samples containing specific minerals and microbes found in target reservoirs. For instance, a rock containing pyrite could be used to monitor the formation of H_2S over time. Introducing microbes into the rock sample would demonstrate how microbial metabolisms, which consume hydrogen, produce hydrogen sulfide (H_2S) and methane (CH_4), among other compounds. This not only results in a loss of pure hydrogen but also influences the required technologies in processing facilities, potentially affecting the economic viability of UHS in a target reservoir, as highlighted in the techno-economic case study's concept comparison.

While both parts of this thesis delve into different aspects of the same topic, it is evident that their results can have interrelated implications. Therefore, future experimental work should be tailored to enhance site-specific relevance, thereby reducing reliance on assumptions in techno-economic analyses.

Bibliography

[1] M. Aasadnia, M. Mehrpooya, and B. Ghorbani. “A novel integrated structure for hydrogen purification using the cryogenic method”. In: *Journal of Cleaner Production* 278 (2021).

[2] Ademola Isaac Adebimpe et al. “Percolation without trapping: how Ostwald ripening during two-phase displacement in porous media alters capillary pressure and relative permeability”. In: 2024. URL: https://api.semanticscholar.org/CorpusID:268857135.

[3] Irfan Ahmad and Mark T. Looijer. *[Shell internal document]*. Tech. rep. Shell, Apr. 2023.

[4] Masoud Aslannezhad et al. “A review of hydrogen/rock/brine interaction: Implications for Hydrogen Geo-storage”. In: *Progress in Energy and Combustion Science* 95 (2023), p. 101066.

[5] Atlas Leefomgeving. *Kaarten*. Accessed: 2024-04-02. 2024. URL: https://www.atlasleefomgeving.nl/kaarten.

[6] Matin Bagheri et al. “Direct pore-scale simulation of the effect of capillary number and gas compressibility on cyclic underground hydrogen storage & production in heterogeneous aquifers”. In: *Advances in Water Resources* 181 (2023), p. 104547.

[7] Herib Blanco and André Faaij. “A review at the role of storage in energy systems with a focus on Power to Gas and long-term storage”. In: *Renewable and Sustainable Energy Reviews* 81 (2018), pp. 1049–1086.

[8] Martin J Blunt. “Ostwald ripening and gravitational equilibrium: Implications for long-term subsurface gas storage”. In: *Physical Review E* 106.4 (2022), p. 045103.

[9] Zhenkai Bo et al. “Effects of geological heterogeneity on gas mixing during underground hydrogen storage (UHS) in braided-fluvial reservoirs”. In: *Fuel* 357 (2024), p. 129949.

[10] Maartje Boon and Hadi Hajibeygi. “Experimental characterization of H 2/water multiphase flow in heterogeneous sandstone rock at the core scale relevant for underground hydrogen storage (UHS)”. In: *Scientific reports* 12.1 (2022), p. 14604.

[11] J. Bouma. *Underground hydrogen storage H2S removal technologies*. Tech. rep. Shell, 2023.

[12] Harry W Brown. “Capillary pressure investigations”. In: *Journal of Petroleum Technology* 3.03 (1951), pp. 67–74.

[13] Andrew Cavanagh et al. *Hydrogen storage potential of existing European gas storage sites in depleted gas fields and aquifers*. Tech. rep. D1.3. Europe: HyUSPRe, June 2022. URL: https://www.hyuspre.eu/wp-content/uploads/2022/06/HyUSPRe_D1.3_Hydrogen-storage-potential-of-existing-European-gas-storage-sites_2022.06.29.pdf.

[14] Salaheddine Chabab et al. “Solubility of H2 in water and NaCl brine under subsurface storage conditions: Measurements and thermodynamic modeling”. In: *International Journal of Hydrogen Energy* 50 (2024), pp. 648–658.

[15] YT Florence Chow, Geoffrey C Maitland, and JP Martin Trusler. “Interfacial tensions of (H2O+ H2) and (H2O+ CO2+ H2) systems at temperatures of (298–448) K and pressures up to 45 MPa”. In: *Fluid Phase Equilibria* 475 (2018), pp. 37–44.

[16] Costain. *Destination for tail gas from hydrogen purification*. Tech. rep. Shell, 2022.

[17] Quoc Truc Doan et al. “Molecular dynamics simulation of interfacial tension of the CO2-CH4-water and H2-CH4-water systems at the temperature of 300 K and 323 K and pressure up to 70 MPa”. In: *Journal of Energy Storage* 66 (2023), p. 107470.

[18] Erle C Donaldson and Waqi Alam. *Wettability*. Elsevier, 2013.

[19] EBN and TNO. *Haalbaarheidsstudie Offshore Ondergrondse Waterstofopslag*. R11212, version 07.07.2022. EBN and TNO, 2022. URL: https://www.example.com.

[20] Eneco. *Enecogen*. https://www.eneco.nl/en/about-us/what-we-do/sustainable-sources/other-projects/enecogen/. 2024.

[21] Engineering ToolBox. *Diffusion Coefficients of Gases in Water*. https://www.engineeringtoolbox.com/diffusion-coefficients-d_1404.html. Accessed: 2024-06-01. 2024.

[22] Hamid Esfandyari et al. “Experimental evaluation of rock mineralogy on hydrogen-wettability: Implications for hydrogen geo-storage”. In: *Journal of Energy Storage* 52 (2022), p. 104866.

[23] Yves Gensterblum et al. “Gas transport and storage capacity in shale gas reservoirs–A review. Part A: Transport processes”. In: *Journal of Unconventional Oil and Gas Resources* 12 (2015), pp. 87–122.

[24] Eleni Gianni et al. “Underground hydrogen storage: The techno-economic perspective”. In: *Open Research Europe* 4 (2024).

[25] Sepideh Goodarzi et al. “Trapping, hysteresis and Ostwald ripening in hydrogen storage: A pore-scale imaging study”. In: *International Journal of Hydrogen Energy* 56 (2024), pp. 1139–1151.

[26] Google Earth. *Google Earth*. https://earth.google.com/web/@51.94878992,4.15411243,6.09417506a,1468.39066311d,35y,0h,0t,0r. Apr. 2024.

[27] F. Haghighatjoo, S. Z. Lak, and M. R. Rahimpour. “Hydrogen Purification and Technologies”. In: *Elsevier* (2024).

[28] Leila Hashemi, Martin Blunt, and Hadi Hajibeygi. “Pore-scale modelling and sensitivity analyses of hydrogen-brine multiphase flow in geological porous media”. In: *Scientific reports* 11.1 (2021), p. 8348.

[29] Niklas Heinemann et al. “Enabling large-scale hydrogen storage in porous media – the scientific challenges”. In: *Energy Environ. Sci.* 14 (2 2021), pp. 853–864. DOI: 10.1039/D0EE03536J. URL: http://dx.doi.org/10.1039/D0EE03536J.

[30] Niklas Heinemann et al. “Enabling large-scale hydrogen storage in porous media–the scientific challenges”. In: *Energy & Environmental Science* 14.2 (2021), pp. 853–864.

[31] Scott Higgs et al. “Direct measurement of hydrogen relative permeability hysteresis for underground hydrogen storage”. In: *International Journal of Hydrogen Energy* 50 (2024), pp. 524–541.

[32] Scott Higgs et al. “In-situ hydrogen wettability characterisation for underground hydrogen storage”. In: *International Journal of Hydrogen Energy* 47.26 (2022), pp. 13062–13075.

[33] M. Honarpour and S.M. Mahmood. “Relative-Permeability Measurements: An Overview”. In: *Journal of Petroleum Technology* 40.08 (Aug. 1988), pp. 963–966. ISSN: 0149-2136. DOI: 10.2118/18565-PA. eprint: https://onepetro.org/JPT/article-pdf/40/08/963/2221692/spe-18565-pa.pdf. URL: https://doi.org/10.2118/18565-PA.

[34] S. Huisman, A. Correnti, and M. Verlaan. *Impact of Reservoir Uncertainties and Design Choices on Back Produced Gas Composition in Underground Hydrogen Storage*. Tech. rep. Shell, 2023.

[35] Thejas Hulikal Chakrapani et al. “Mutual Diffusivities of Mixtures of Carbon Dioxide and Hydrogen and Their Solubilities in Brine: Insight from Molecular Simulations”. In: *Industrial & Engineering Chemistry Research* (2024).

[36] *Hydrogen Underground storage in Porous Reservoirs (HyUsPRe)*. Accessed on 30 January 2024. HyUsPRe Consortium. 2024. URL: https://www.hyuspre.eu/ (visited on 01/30/2024).

[37] Hynetwork. *Quality specification for hydrogen*. https://www.hynetwork.nl/en/news/quality-specification-for-hydrogen. Accessed: June 24, 2024. Oct. 2021.

[38] Hystock. *Hystock: Green Hydrogen through Underground Storage*. Accessed: 2024-01-17. 2022. URL: https://www.hystock.nl.

[39] Stefan Iglauer, Muhammad Ali, and Alireza Keshavarz. “Hydrogen wettability of sandstone reservoirs: implications for hydrogen geo-storage”. In: *Geophysical Research Letters* 48.3 (2021), e2020GL090814.

[40] International Energy Agency. *Hydrogen*. License: CC BY 4.0. Paris, 2023. URL: https://www.iea.org/reports/hydrogen-2156.

[41] IRENA. *Global Trends*. https://www.irena.org/Data/View-data-by-topic/Costs/Global-Trends. 2023.

[42] Diego Viesi Jacopo de Maigret. *Equipment requirements and capital as well as operating costs for the hydrogen scenarios*. HyUSPRe WP7. HyUSPRe, Apr. 2023. URL: https://www.hyuspre.eu/wp-content/uploads/2023/04/HyUSPRe_WP7_Operating-costs-for-hydrogen-scenarios_2023.04.14.pdf.

[43] Zaid Jangda et al. “Pore-scale visualization of hydrogen storage in a sandstone at subsurface pressure and temperature conditions: Trapping, dissolution and wettability”. In: *Journal of Colloid and Interface Science* 629 (2023), pp. 316–325.

[44] Hubert Jannel and Matthias Torquet. *Conceptual Design of Salt Cavern and Porous Media Underground Storage Site*. Hystories Deliverable D7.1-1. Public Document. Geostock France, Apr. 2022.

[45] Nilesh Kumar Jha et al. “Pore scale investigation of hydrogen injection in sandstone via X-ray micro-tomography”. In: *International Journal of Hydrogen Energy* 46.70 (2021), pp. 34822–34829.

[46] G.P. Kidambi, A. Sullerey, and J.J. Williams. *Gas Treating Guideline*. Tech. rep. Shell, 2020.

[47] Samuel Krevor et al. “Capillary trapping for geologic carbon dioxide storage–From pore scale physics to field scale implications”. In: *International Journal of Greenhouse Gas Control* 40 (2015), pp. 221–237.

[48] Samuel CM Krevor et al. “Relative permeability and trapping of CO2 and water in sandstone rocks at reservoir conditions”. In: *Water resources research* 48.2 (2012).

[49] B. Li et al. “A Brief Climatology of Dunkelflaute Events over and Surrounding the North and Baltic Sea Areas”. In: *Energies* 14.20 (2021), p. 6508.

[50] *Hydrogen Storage in Depleted Gas Fields: A North Sea Case Study*. Vol. Day 3 Thu, September 07, 2023. SPE Offshore Europe Conference and Exhibition. Sept. 2023, D031S013R001.

[51] Anna S Lord, Peter H Kobos, and David J Borns. “Geologic storage of hydrogen: Scaling up to meet city transportation demands”. In: *International journal of hydrogen energy* 39.28 (2014), pp. 15570–15582.

[52] Maksim Lysyy et al. “Hydrogen relative permeability hysteresis in underground storage”. In: *Geophysical Research Letters* 49.17 (2022), e2022GL100364.

[53] J. Miocic et al. “Underground hydrogen storage: a review”. In: *Geological Society, London, Special Publications* 528 (2023), pp. 73–86.

[54] T. Mohammad-Reza. “Recent advances in hydrogen compressors for use in large-scale renewable energy integration”. In: *International Journal of Hydrogen Energy* (2022), pp. 35275–35292.

[55] Natura 2000. *Natura 2000 gebieden*. https://www.natura2000.nl/gebieden. 2024.

[56] Hailun Ni et al. “Predicting CO2 residual trapping ability based on experimental petrophysical properties for different sandstone types”. In: *International Journal of Greenhouse Gas Control* 86 (2019), pp. 158–176.

[57] *NIST Chemistry WebBook*. URL: https://webbook.nist.gov/chemistry/fluid/ (visited on 03/27/2024).

[58] *NLOG - Kaart Boringen*. https://www.nlog.nl/kaart-boringen. Accessed: June 24, 2024.

[59] JS Osoba et al. “Laboratory measurements of relative permeability”. In: *Journal of Petroleum Technology* 3.02 (1951), pp. 47–56.

[60] PetroSkills. *Volume 1: The Basic Principles. In J. M. Campbell, Gas Conditioning and Processing*. Tulsa, Oklahoma: PetroSkills, LLC, 2020.

[61] PetroSkills. *Volume2: The Equipment Modules. In Gas Conditioning and Processing*. Tulsa: PetroSkills, 2017.

[62] *Project Description - Underground Sun Storage*. Accessed on 30 January 2024. Underground Sun Storage. 2024. URL: https://www.underground-sun-storage.at/en/project/project-description.html (visited on 01/30/2024).

[63] CA Reynolds and S Krevor. "Characterizing flow behavior for gas injection: Relative permeability of CO2-brine and N2-water in heterogeneous rocks". In: *Water Resources Research* 51.12 (2015), pp. 9464–9489.

[64] Amin Rezaei et al. "Relative Permeability of Hydrogen and Aqueous Brines in Sandstones and Carbonates at Reservoir Conditions". In: *Geophysical Research Letters* 49.12 (2022). e2022GL099433 2022GL099433, e2022GL099433. DOI: https://doi.org/10.1029/2022GL099433. eprint: https://agupubs.onlinelibrary.wiley.com/doi/pdf/10.1029/2022GL099433. URL: https://agupubs.onlinelibrary.wiley.com/doi/abs/10.1029/2022GL099433.

[65] Leopoldo M. Ruiz Maraggi and Lorena G. Moscardelli. "Modeling hydrogen storage capacities, injection and withdrawal cycles in salt caverns: Introducing the GeoH2 salt storage and cycling app". In: *International Journal of Hydrogen Energy* 48.69 (2023), pp. 26921–26936. ISSN: 0360-3199. DOI: https://doi.org/10.1016/j.ijhydene.2023.03.293. URL: https://www.sciencedirect.com/science/article/pii/S0360319923014167.

[66] Rolf Sander. "Compilation of Henry's law constants (version 4.0) for water as solvent". In: *Atmospheric Chemistry and Physics* 15.8 (2015), pp. 4399–4981.

[67] M.-R. Tahan. "Recent advances in hydrogen compressors for use in large-scale renewable energy integration". In: *International Journal of Hydrogen Energy* (2022), pp. 35275–35292.

[68] Yukie Tanino and Martin J Blunt. "Capillary trapping in sandstones and carbonates: Dependence on pore structure". In: *Water Resources Research* 48.8 (2012).

[69] TESCAN. *CoreTOM Product Flyer*. URL: https://info.tescan.com/coretom-product-flyer (visited on 04/21/2024).

[70] Eike M Thaysen et al. "Estimating microbial growth and hydrogen consumption in hydrogen storage in porous media". In: *Renewable and Sustainable Energy Reviews* 151 (2021), p. 111481.

[71] Eike M Thaysen et al. "Pore-scale imaging of hydrogen displacement and trapping in porous media". In: *International Journal of Hydrogen Energy* 48.8 (2023), pp. 3091–3106.

[72] Thunder Said Energy. *Cryogenic air separation: costs and energy economics?* https://thundersaidenerg com/downloads/cryogenic-air-separation-the-economics/. 2024.

[73] Esteban R Ugarte and Saeed Salehi. "A review on well integrity issues for underground hydrogen storage". In: *Journal of Energy Resources Technology* 144.4 (2022), p. 042001.

[74] *Underground Hydrogen Storage - HyChico*. Accessed on 30 January 2024. HyChico. 2024. URL: https://hychico.com.ar/eng/underground-hydrogen-storage.php (visited on 01/30/2024).

[75] Vindum. *Vindum Metering Pumps*. URL: https://vindum.com/products/vindum-metering-pumps (visited on 04/21/2024).

[76] Jan Vinogradov, Rhiannon Hill, and Damien Jougnot. "Influence of Pore Size Distribution on the Electrokinetic Coupling Coefficient in Two-Phase Flow Conditions". In: *Water* 13 (Aug. 2021), p. 2316. DOI: 10.3390/w13172316.

[77] Peter Willis Voorhees. "Ostwald ripening of two-phase mixtures". In: *Annual Review of Materials Science* 22.1 (1992), pp. 197–215.

[78] Weather Atlas. *Climate and monthly weather forecast The Hague, Netherlands*. https://www.weather-atlas.com/en/netherlands/the-hague-climate. 2024.

[79] Wikipedia. *Lijst van elektriciteitscentrales in Nederland*. https://en.wikipedia.org/wiki/List_of_power_stations_in_the_Netherlands. 2024.

[80] Ahmed Al-Yaseri et al. "Initial and residual trapping of hydrogen and nitrogen in Fontainebleau sandstone using nuclear magnetic resonance core flooding". In: *International Journal of Hydrogen Energy* 47.53 (2022), pp. 22482–22494.

[81] AE Yekta et al. “Determination of hydrogen–water relative permeability and capillary pressure in sandstone: application to underground hydrogen injection in sedimentary formations”. In: *Transport in Porous Media* 122.2 (2018), pp. 333–356.

[82] Tuna Yildirim et al. “Electrostatic forces and higher order curvature terms of Young–Laplace equation on nanobubble stability in water”. In: *NPJ Clean Water* 5.1 (2022), p. 18.

[83] Seyed Hamidreza Yousefi et al. “Techno-economic analysis of developing an underground hydrogen storage facility in depleted gas field: A Dutch case study”. In: *International Journal of Hydrogen Energy* 48.74 (2023), pp. 28824–28842.

[84] Yihuai Zhang et al. “Pore-Scale Observations of Hydrogen Trapping and Migration in Porous Rock: Demonstrating the Effect of Ostwald Ripening”. In: *Geophysical Research Letters* 50.7 (2023), e2022GL102383.

A

Detailed image processing procedure

This appendix provides a guide to the processing steps involved in the pore-scale data analysis and visualization for this experiment. Step-by-step instructions in Avizo 3D 2023 (Thermo Fisher) are accompanied by screenshots. This guide aims to maximize reproducibility for future research. It is recommended to first watch a tutorial on basic navigation in Avizo.

1. **Open data**

   When opening large data sets in Avizo, you can choose from several methods. Select ”Read complete volume into memory”. Depending on the size of the data, this may take some time. Afterward, define the resolution of the acquired images by entering the voxel size, then click OK.

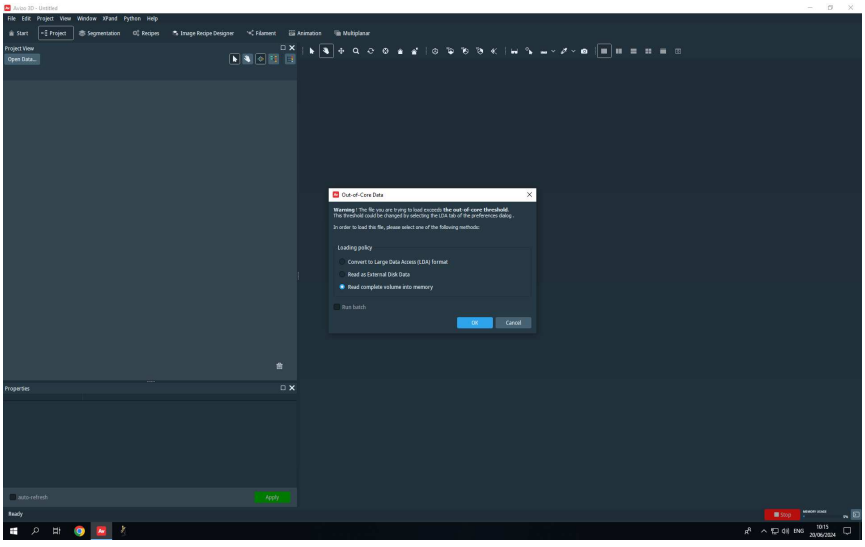

Figure A.1: Select ”Read complete volume into memory” after opening the data.

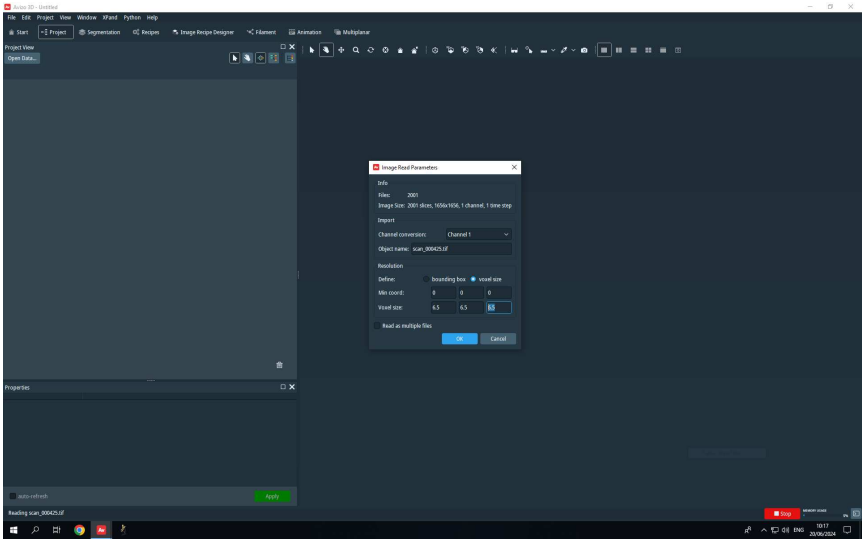

Figure A.2: Enter the voxel size for all axes.

2. **Data visualisation**

   When the data is uploaded, Avizo will automatically add an Ortho Slice to visualize the raw data. You may need to adjust the colormap to properly see the images. This can be done by dragging the lower and/or upper end of the colormap range in the Ortho Slice properties window. Additionally, you can visualize the other slices here as well.

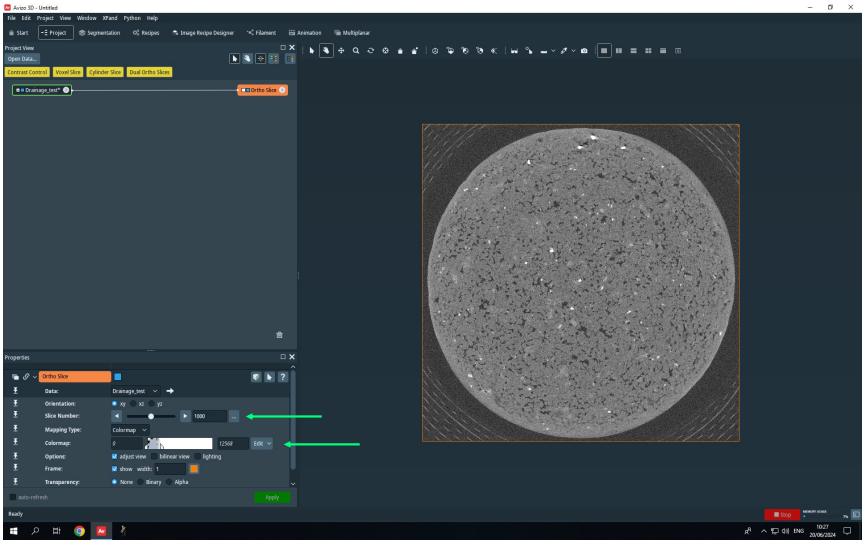

Figure A.3: Visualisation can be adjusted in the properties window of the Ortho Slice.

3. **Volume edit**

   The data can now be cropped to include only the volume of interest. To do this, right-click the data file and select the 'Volume Edit' tool. In the properties window, choose 'TabBox', 'Cylinder', 'Lines', and 'Z axis'. Next, change the view to 'Orthographic' and select the cursor. Drag the green squares to encompass only the area of interest. Then, change the view and orientation in the Ortho Slice to XZ and repeat the process. Do the same for the YZ view/orientation. Once the volume of interest is selected, return to Volume Edit and click 'Cut: Outside'. Finally, click 'Apply'.

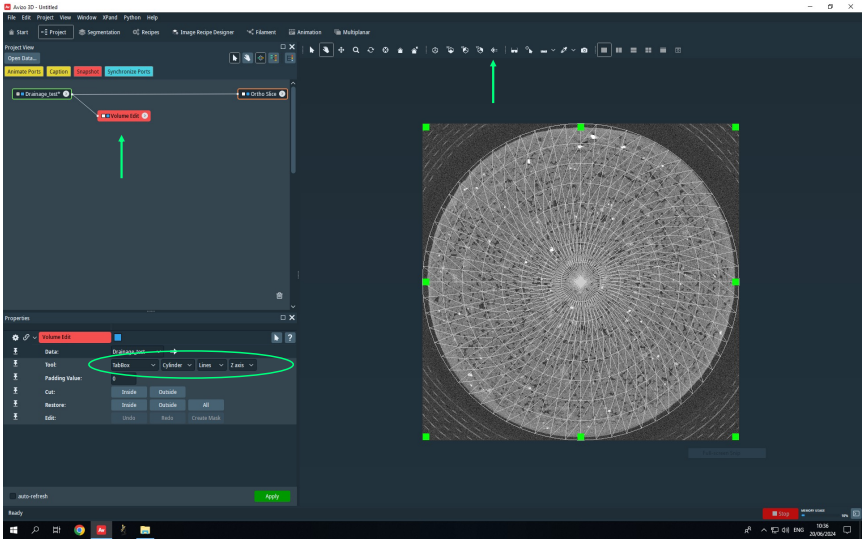

Figure A.4: Select the area of interest using the 'Volume Edit' tool.

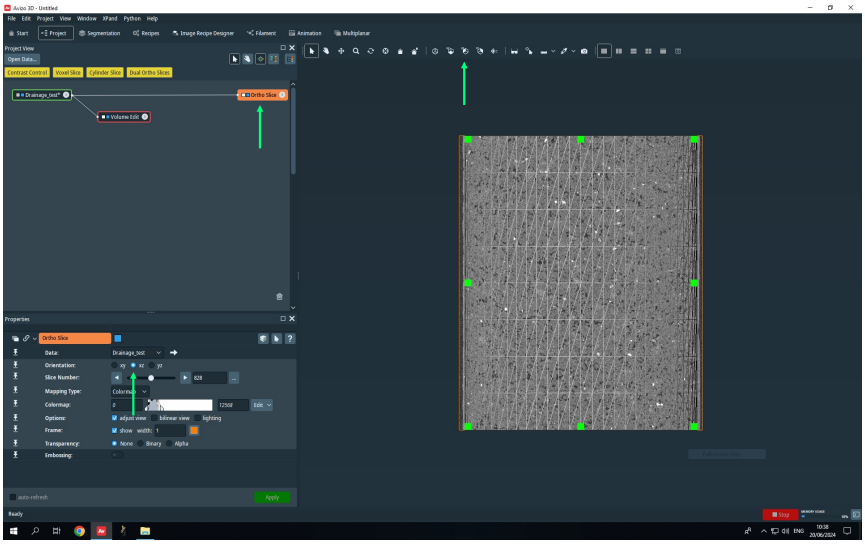

Figure A.5: Change the view and orientation in the Ortho Slice to XZ and repeat the process. Do the same for the YZ axis.

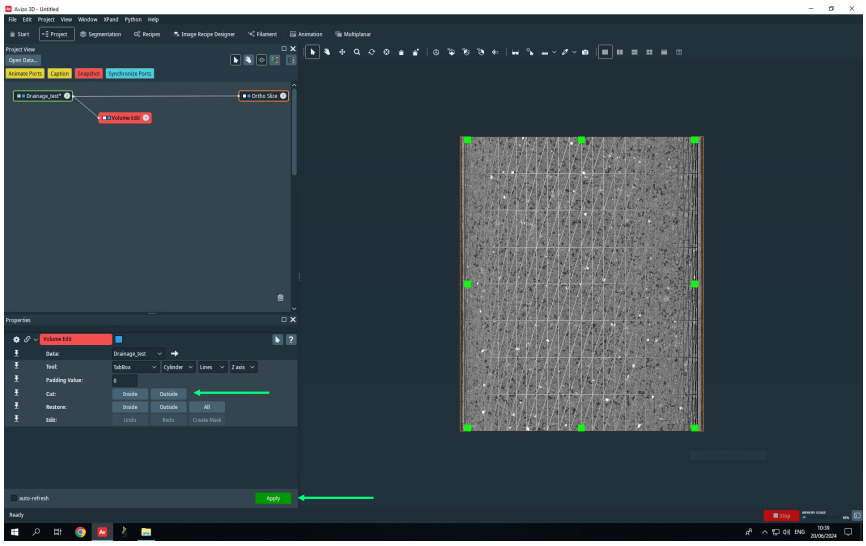

Figure A.6: In the Volume Edit properties window, click 'Cut: Outside'.

4. **Filtering**

   A new cropped file will appear. Select this file and apply a 'Filter Sandbox'. Within this tool, various filters can be tested on a preview area. For this experiment, the Median filter yielded good results with 3D interpretation and 2 iterations. Click 'Apply'.

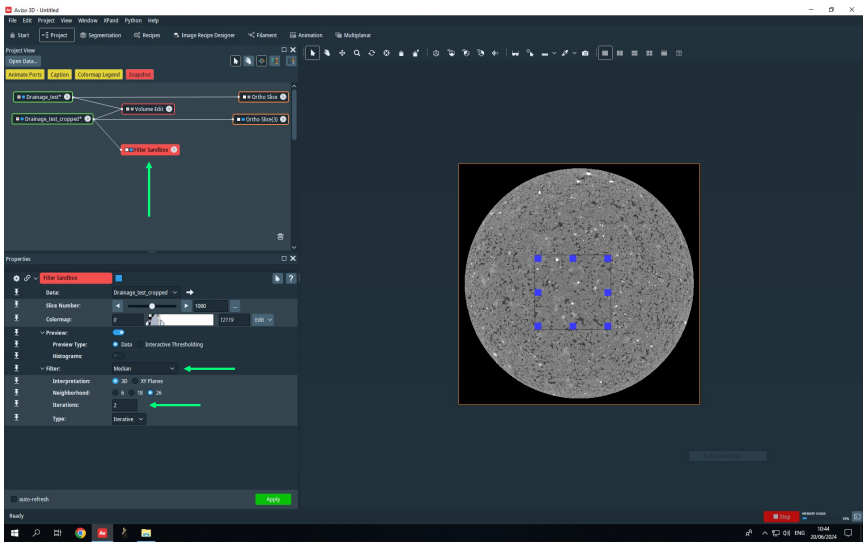

Figure A.7: Different filters can be tested in the 'Filter Sandbox' tool.

5. **Image registration**

   To allow meaningful comparisons between different scans, all images need to be precisely aligned. For every scan, upload the same reference scan for alignment. In this experiment, the cropped and filtered 'Dry scan' is used. Select the scan of the experiment and open the 'Image Registration Wizard'. Choose the correct reference scan and press 'Apply'.

   In steps 2 and 3, select the volume that will be used as input, which the algorithm will use to provide a transformation matrix. For a pore-scale scan, the entire volume can be selected, and no intervention is needed. Press 'Apply' twice to proceed to step 4.

   Here, select the grey-scale values based on which the algorithm will create the transformation matrix. Choose the range of values that are supposed to remain consistent throughout the experiment. A good approach is to include only the grains and mineral intensities, excluding the

fluids. In 'Window', a grey-scale value histogram can be created. Several peaks may appear, representing different phases. Other methods can also be applied to determine a good range of intensities. In this experiment, the minimum 'Histogram Range Reference' and 'Histogram Range Model' values were changed to 4500 to exclude the fluids. Press 'Apply'. The italic text indicates that the data is registered.

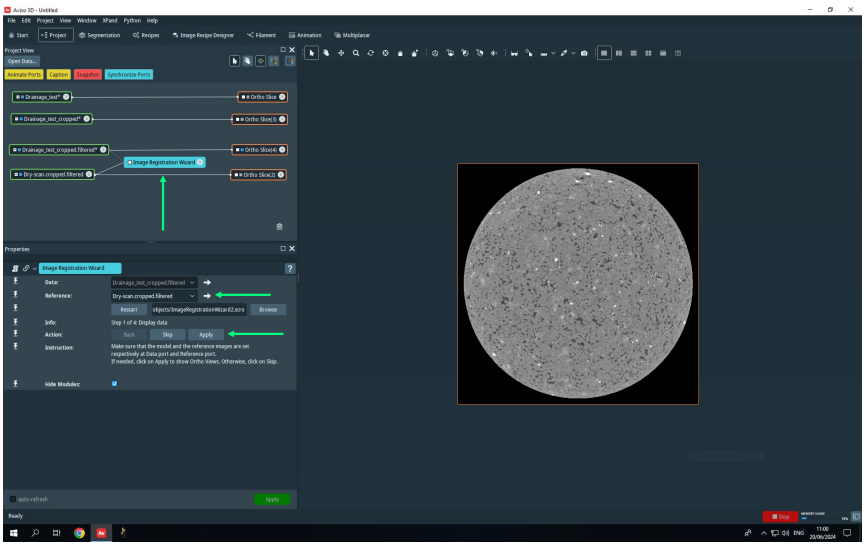

Figure A.8: In the Image Registration Wizard, the reference data must be selected.

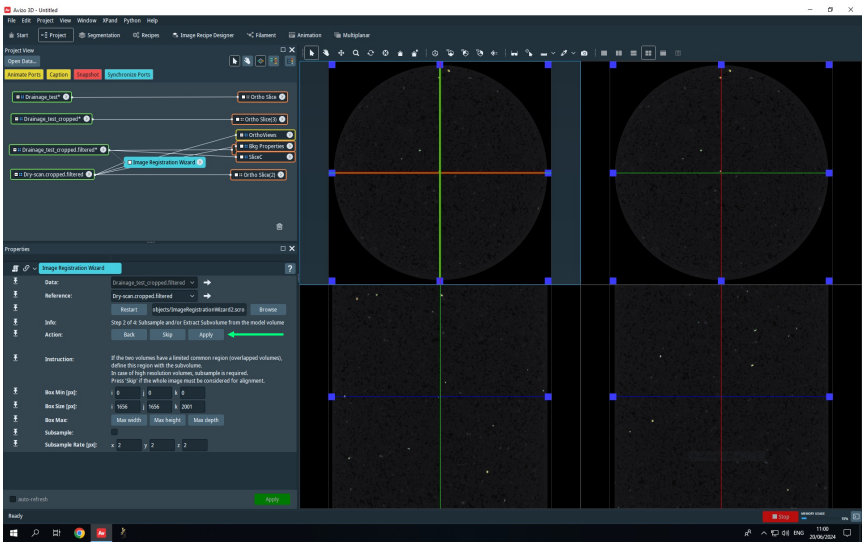

Figure A.9: In step 2 of the Image Registration Wizard, the input data for the transformation matrix algorithm can be selected.

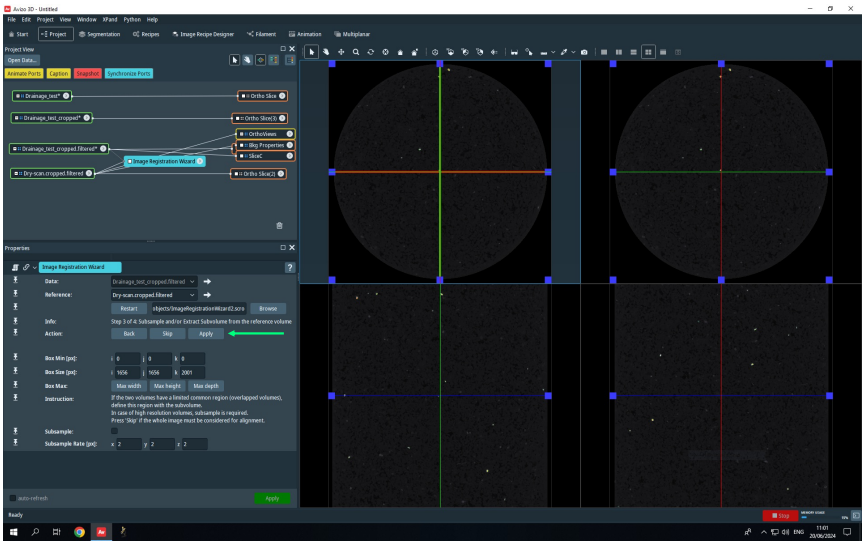

Figure A.10: Similar to step 2, the input data for the transformation matrix algorithm can be selected in step 3.

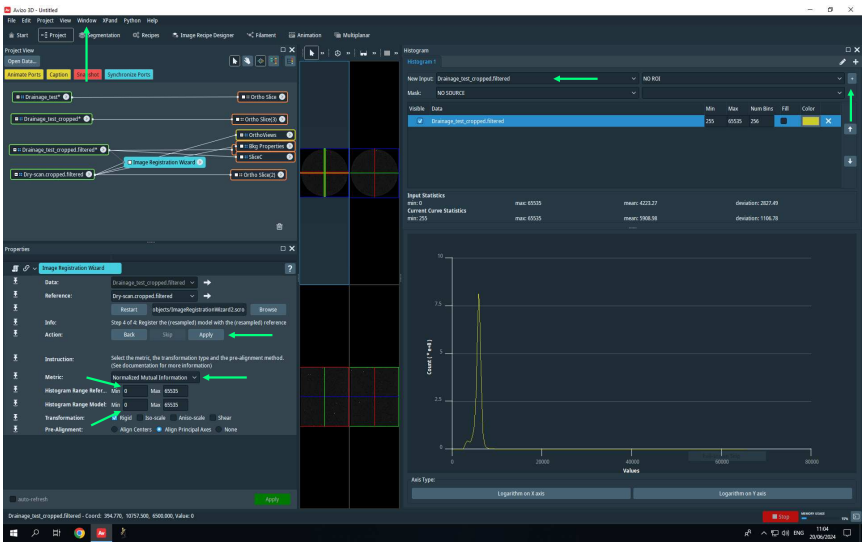

Figure A.11: In step 4, select the grey-scale values based on which the algorithm will create the transformation matrix.

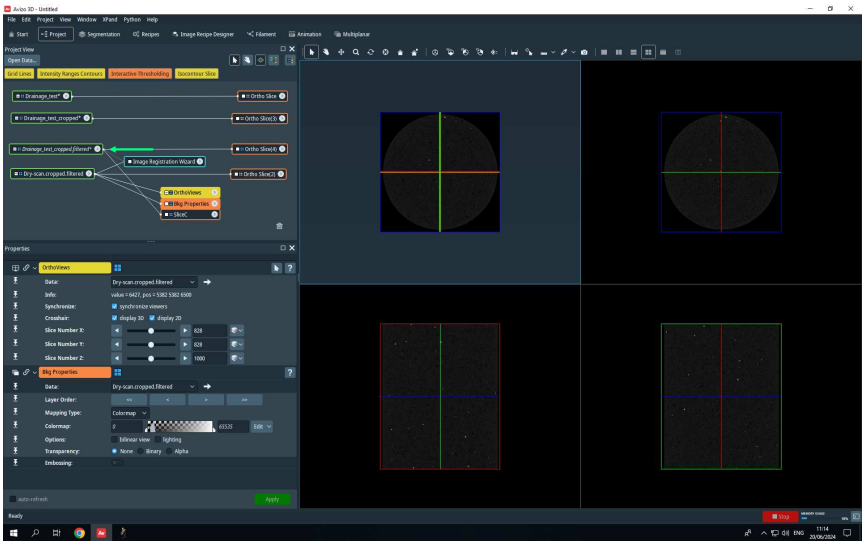

Figure A.12: The italic text indicates that the data is registered.

6. **Resampling**

   Now, the transformation matrix from the registration algorithm can be applied to give new coordinates to the data, ensuring precise alignment. To do this, select the registered data and apply 'Resample Transformed Image'. Ensure that the Dry scan is included as the reference. Select Lanczos interpolation and press 'Apply'. Resampling may require some time, depending on the data size.

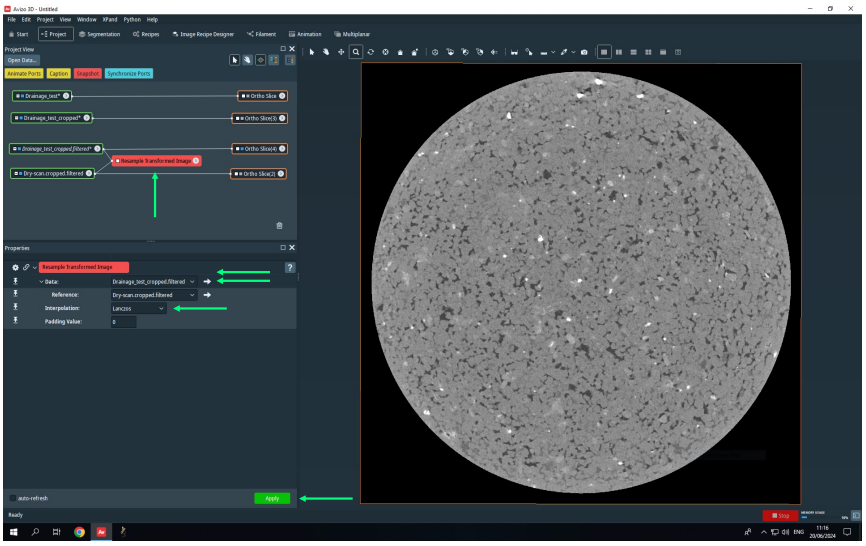

Figure A.13: 'Resample Transformed Image'. Ensure that the Dry scan is included as the reference and apply Lanczos interpolation.

7. **Masking Dry scan**

   To separate the fluids from the grains, a 'mask' should be created for the pore space. Select the Dry scan and apply 'Interactive Thresholding'. In this experiment, a value of 4500 was chosen as the lower end of the grey-scale values for the grains. Therefore, this value was used as the upper end of the intensity range when extracting the pore space in the Dry scan. Dragging the ends of the intensity range will display the thresholded data in the image. Hiding and unhiding the Ortho Slice of the Dry scan will help validate the appropriate intensity range to extract the pore space. Press 'Apply' when the correct range is selected. The pore volume can be determined by applying 'Global Analysis' on the thresholded file.

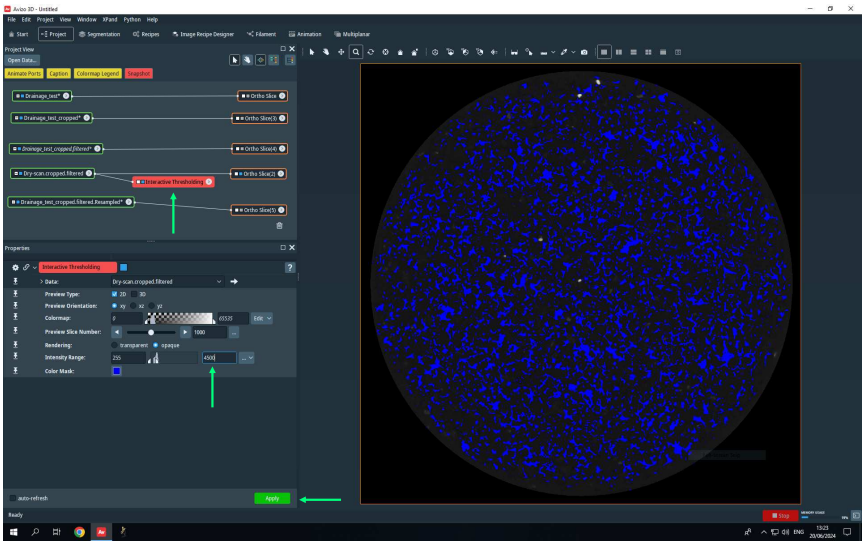

Figure A.14: In the 'Interactive Thresholding' properties window, select the correct intensity range.

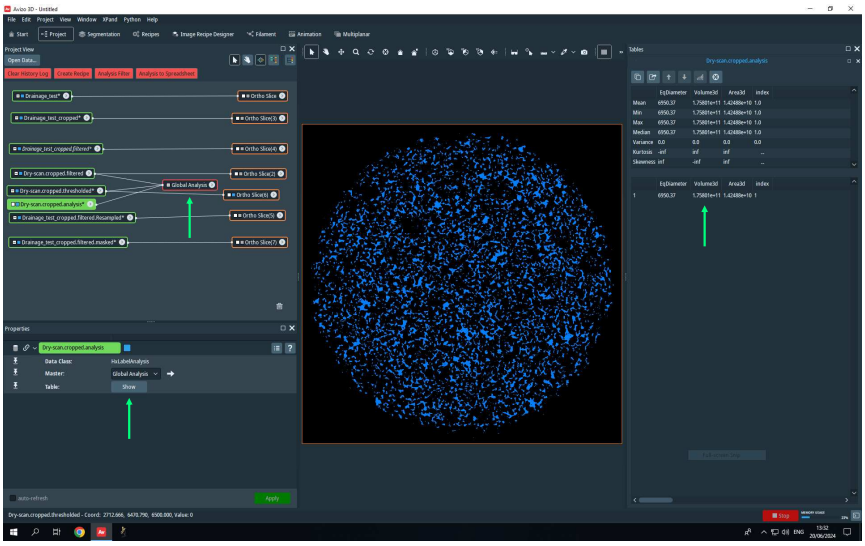

Figure A.15: Global Analysis can be applied to extract the pore volume.

8. **Apply mask**

The mask created using the Dry scan can now be used to separate the fluids from the rock. To do this, select the resampled scan of the experiment and apply 'Mask'. Select the thresholded Dry scan as the 'Input Binary Image', then press 'Apply'.

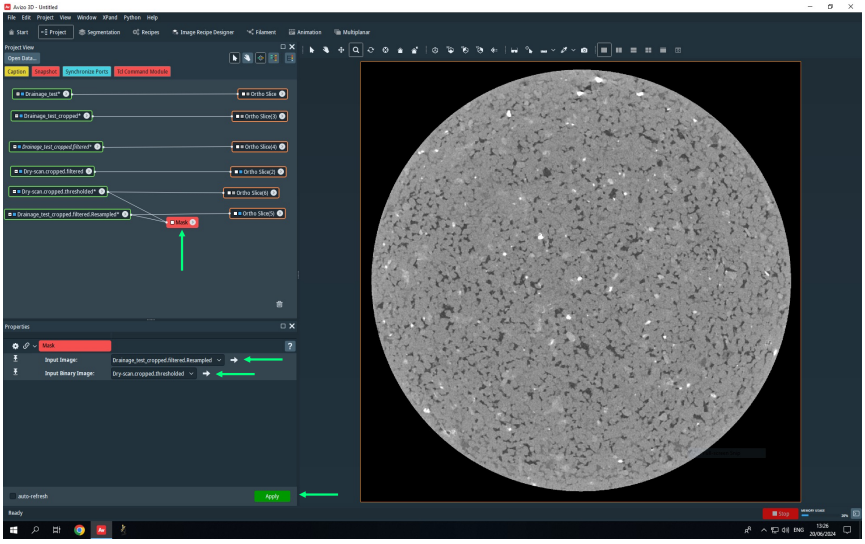

Figure A.16: Use the mask of the pore volume to separate the fluids from the grains in the data of interest.

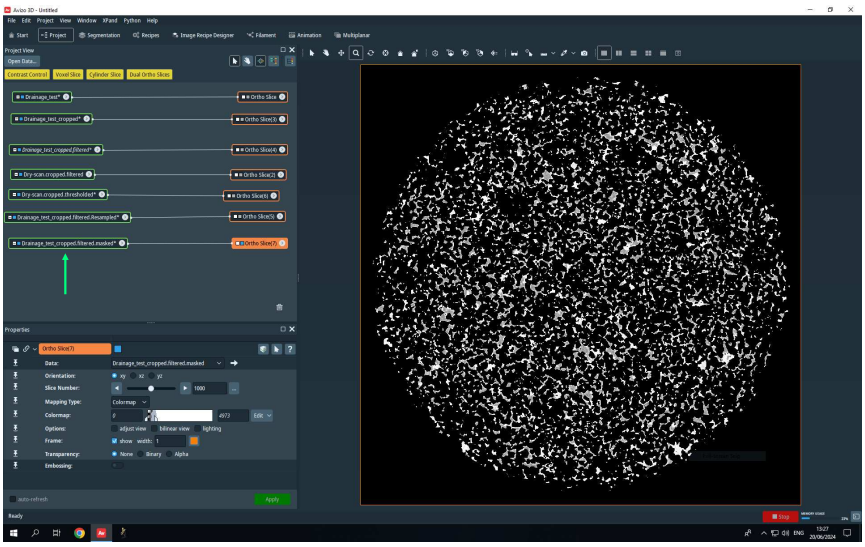

Figure A.17: The masked data extracts information within the pore space while assigning a value of 0 to the remaining data.

9. **Segmenting phases**

To segment the liquid and the gas, apply 'Interactive Thresholding' on the masked data. Adjust the intensity range, and hide and unhide the masked or resampled file to find the appropriate threshold. In this experiment, 4300 was determined to be the correct upper range limit to extract the gas only.

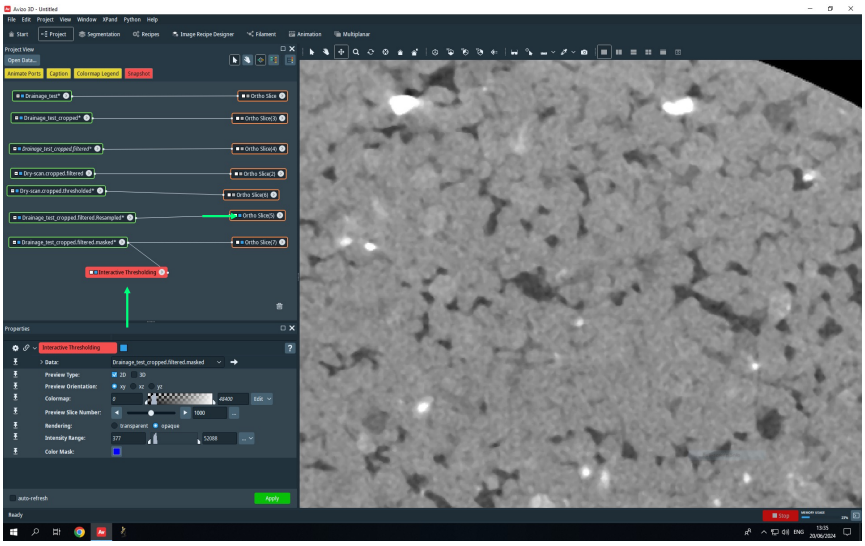

Figure A.18: Apply Interactive Thresholding to the masked data to segment the fluids.

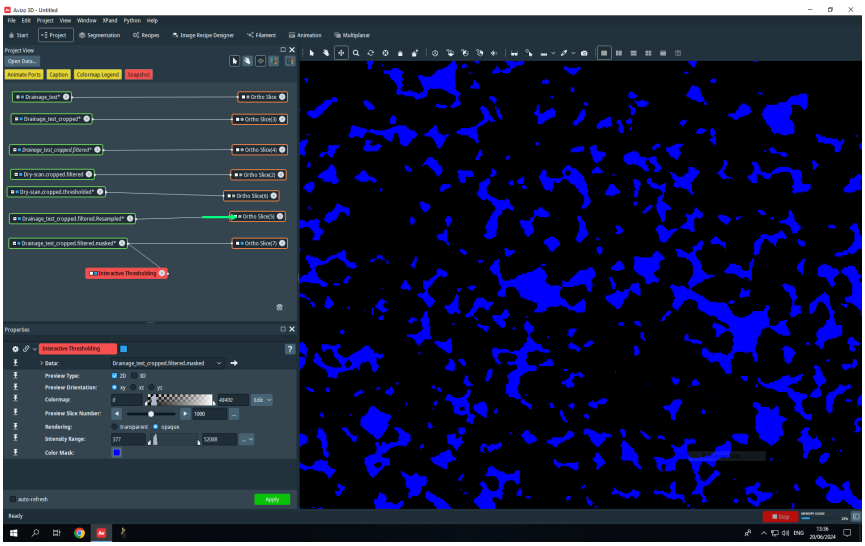

Figure A.19: Hiding and unhiding Ortho Slices can help with the segmentation.

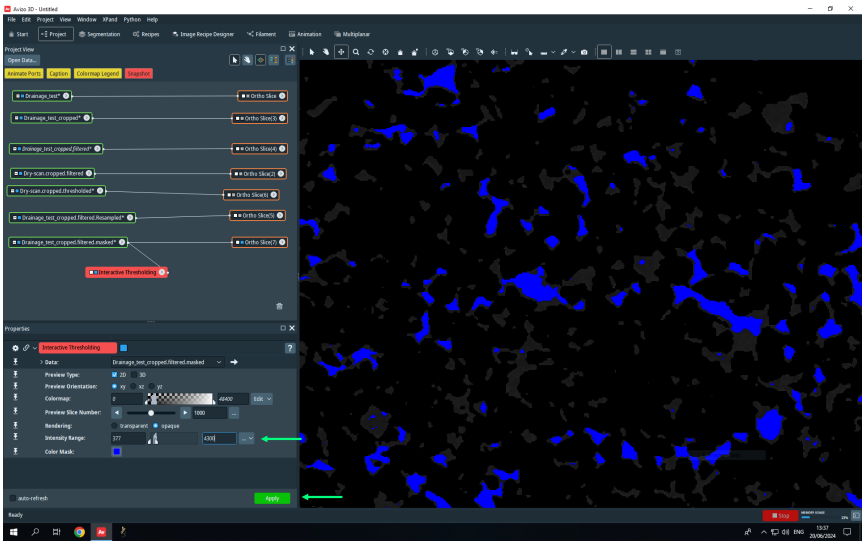

Figure A.20: The thresholded data only includes the phase of interest and assigning a value of 0 to the remaining data.

10. **Labeling**

To analyze distinct gas ganglia, the gas phase needs to be labeled. Apply 'Labeling' to the thresholded file and press 'Apply'. Each labeled gas ganglion is assigned a value corresponding to its label number, independent of the grayscale values.

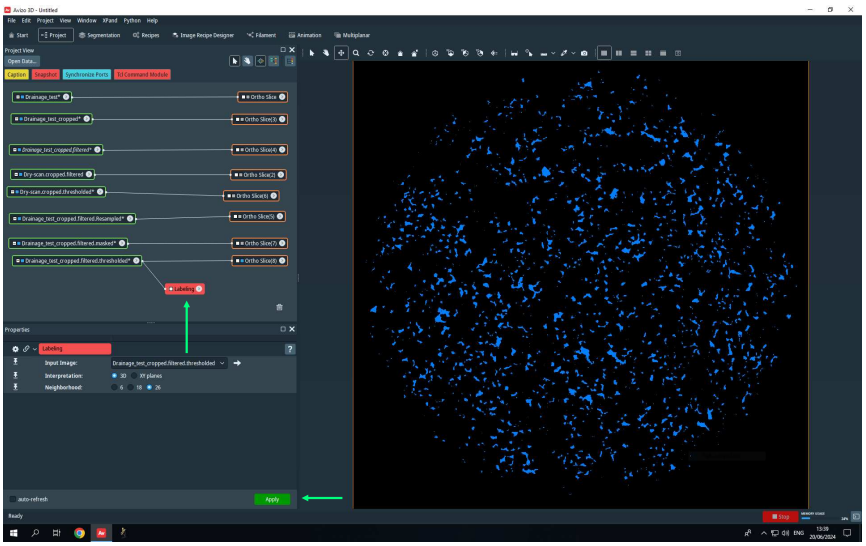

Figure A.21: The Labeling properties window.

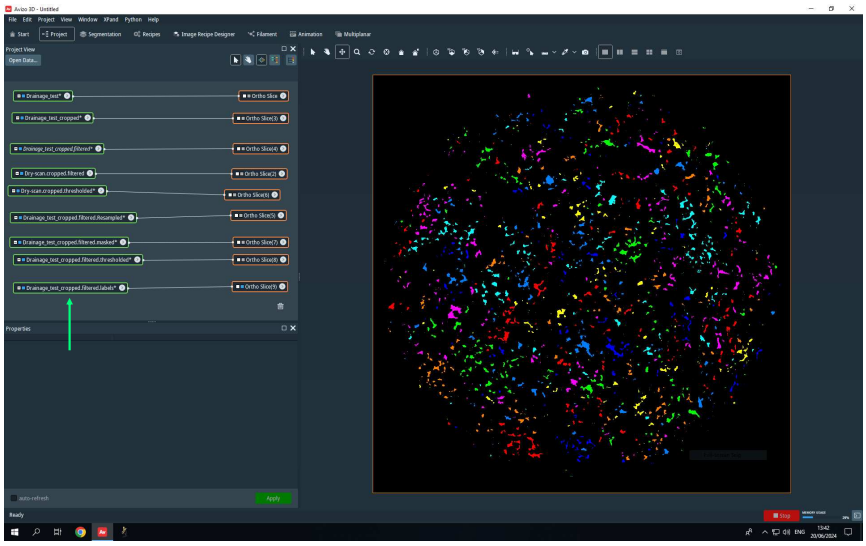

Figure A.22: The labeled gas ganglia.

11. **Volume rendering**

To visualize the individual gas ganglia in 3D, apply 'Volume Rendering'. You can navigate through the volume using the hand cursor. Note that distinct colors indicate distinct, unconnected ganglia. Depending on the number of colors available in the active colormap, not all unconnected ganglia may receive a unique color.

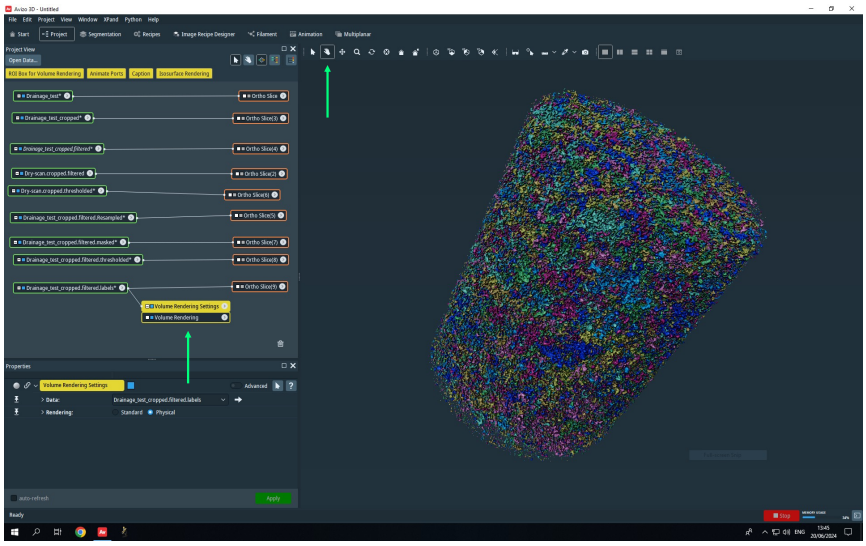

Figure A.23: A 3D volume rendering of the dinstinct gas ganglia.

12. **Label analysis**

Parameters can be extracted from the labels using 'Label Analysis'. Click on the three dots next to 'Measures' to select different parameters for output in the analysis. In this example, equivalent diameter, volume, and surface area of the ganglia are extracted. Export the results as a CSV file for further data analysis. Remember to save intermediate files for potential later processing.

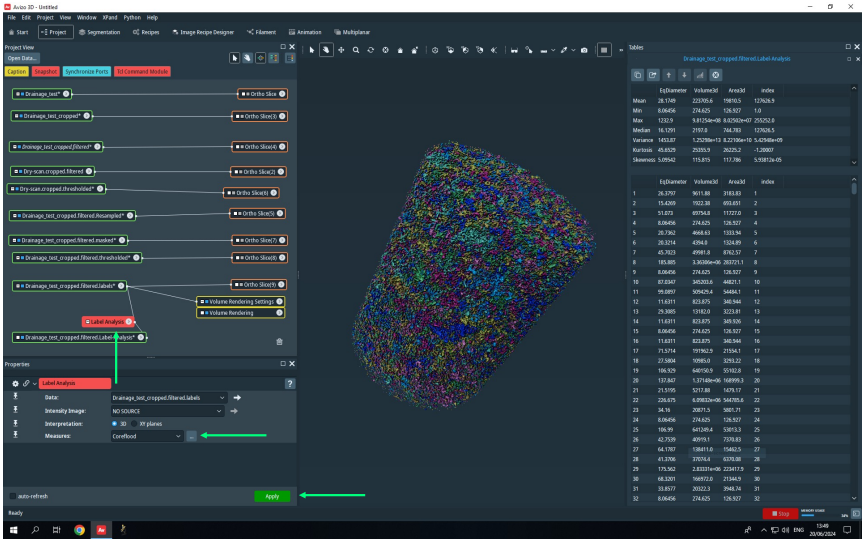

Figure A.24: The Label Analysis result yields data for further analysis.

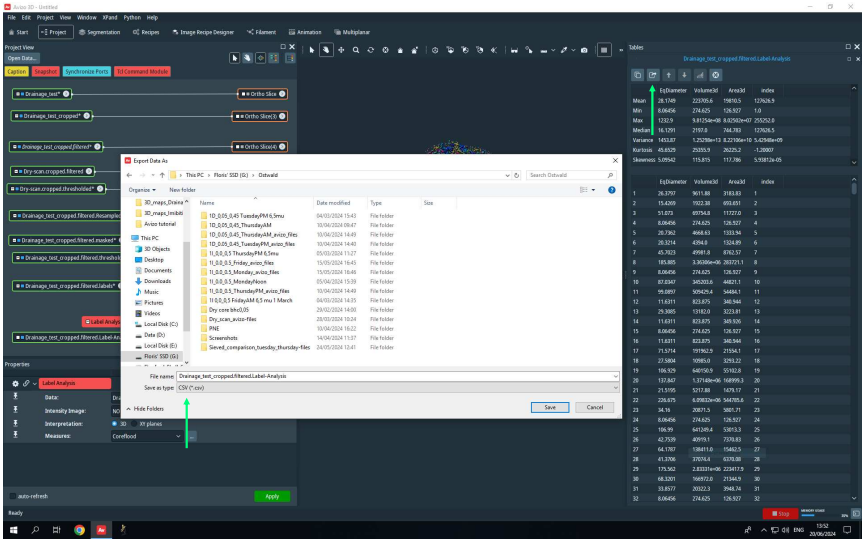

Figure A.25: The data can now be exported to into several formats.

B

Supplementary figures

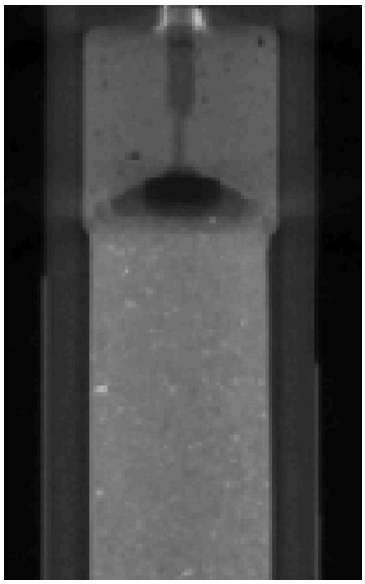

Figure B.1: Raw CT image of the inlet at f_{H2}=0.1. The black bubble shows a buildup of hydrogen in the endcap.

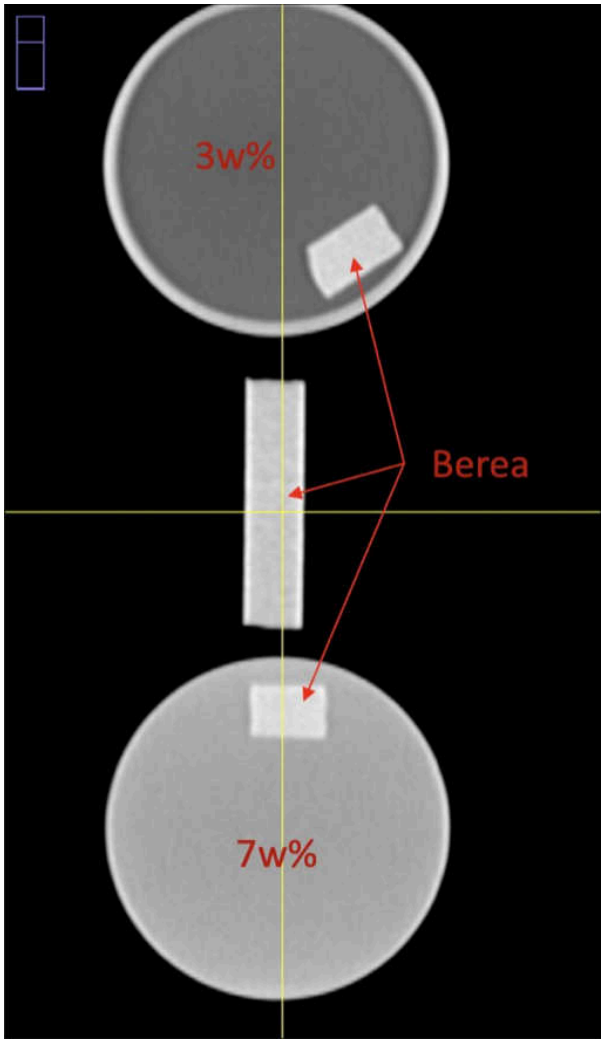

Figure B.2: Comparison of the phase contrast using different KI weight percentages in the brine.

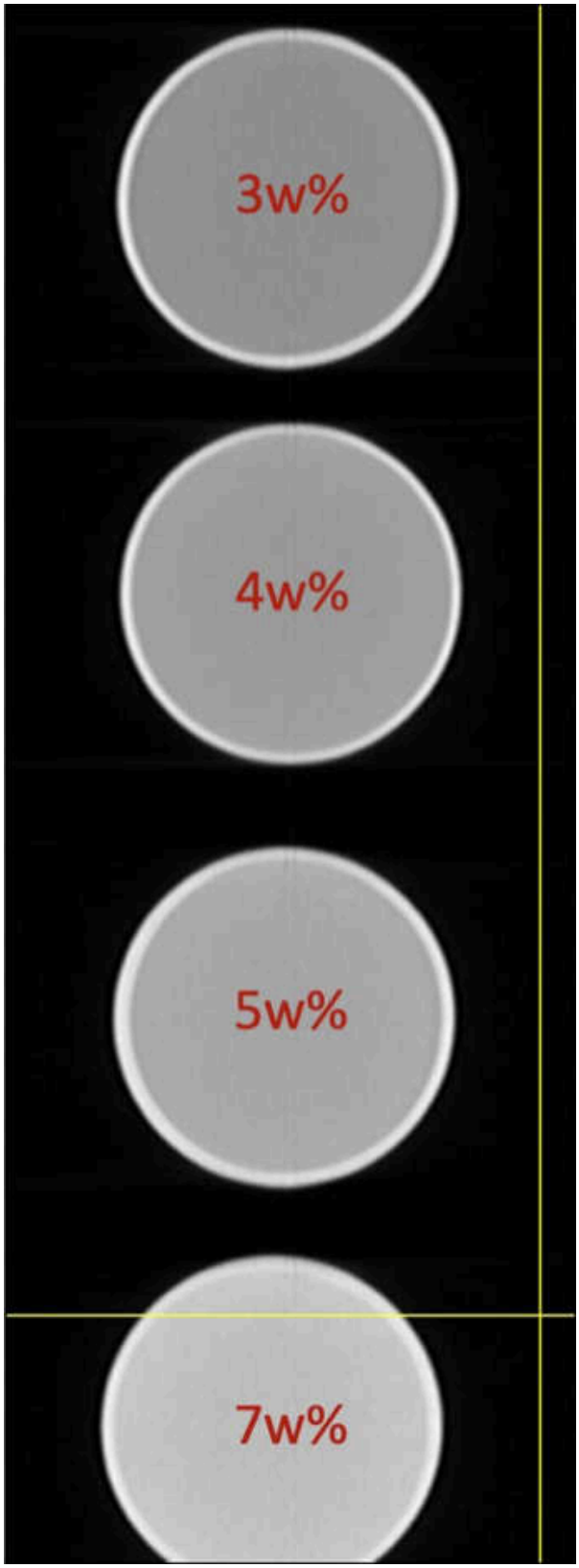

Figure B.3: Comparison of the phase contrast using different KI weight percentages in the brine.

Figure B.4: Coreholder inside CoreTOM CT.

Figure B.5: Experimental set-up outside CoreTOM CT, with the injection pumps visible under the table.